Uncertainties of a near 90 GHz sea ice concentration retrieval algorithm

Dissertation zur Erlangung des Doktorgrades
an der Fakultät für Mathematik, Informatik und Naturwissenschaften
im Fachbereich Geowissenschaften der Universität Hamburg

vorgelegt von

Alexander Beitsch

Hamburg

2014

Tag der Disputation: 01.07.2014

Folgende Gutachter empfehlen die Annahme der Dissertation:
Prof. Dr. Lars Kaleschke
und
Dr. Stefan Kern

Day of oral defense: 01/07/2014

The following evaluators recommend the admission of the dissertation:
Prof. Dr. Lars Kaleschke
and
Dr. Stefan Kern

Prof. Dr. Christian Betzler
Leiter des Departments für Geowissenschaften

Abstract

Passive microwave remote sensing of sea ice concentrations has proven to be the backbone to understand the polar sea ice covers, which are key elements in the global climate system. In over 30 years of remote sensing of sea ice, several retrieval algorithms have been developed using brightness temperature measurements for the investigation of the sea ice covered area by means of the sea ice concentration. Knowledge about the uncertainty of the retrieved ice concentrations is essential to quantify observed trends in sea ice area against the background of natural variability and for the assimilation of sea ice concentrations into numerical weather prediction models. Changes in surface emissivity and variations in atmospheric parameters, like water vapour and cloud cover, are known to have an influence on the accuracy of the retrieved ice concentration. Additionally, the quality of retrieved sea ice concentrations depends on an appropriate choice of the tie-points, which are defined as typical brightness temperatures measured over the surfaces involved.

We investigate uncertainties of a near 90 GHz retrieval algorithm, called the ARTIST Sea Ice algorithm (ASI), by intercomparison with other sea ice concentration data sets. First, we compare ASI and sea ice concentrations retrieved from other retrieval algorithms with visual ship-based observation of the sea ice concentration around Antarctica. After adapting ASI to the new Advanced Microwave Scanning Radiometer 2 (AMSR2) that recently started to provide brightness temperature measurements, we compare the new ASI sea ice concentrations with the Comiso Bootstrap (BST) retrieval, which performed best in the first comparison, and with satellite optical imagery and ice surface temperatures in the Arctic. ASI shows a higher agreement with the other data than BST. Both comparisons show that ASI performs well for different satellite sensors and in different hemispheres. In addition, we present the influence of changing surface emissivities and variations due to changing atmospheric parameters on the ASI retrieval. For a consolidated ice cover during winter, when uncertainties were thought to be limited to variations in surface emissivity, the changes in the snow surface and atmospheric parameters have a considerable influence on ASI and its error estimation. While fresh snow on sea ice that very often reduces the snow surface density tends to decrease retrieved sea ice concentrations, increased atmospheric water vapour increases retrieved sea ice concentrations. We suggest to derive a new set of tie-points separately for both hemispheres and reconsider the current interpolation approach for values between consolidated ice and open water.

Zusammenfassung

Passive Mikrowellenradiometrie bildet die Grundlage die Meereiskonzentrationen in den Polargebieten zu ermitteln. Das Meereis ist eine der wichtigsten Kenngrößen im globalen Klimasystem. In über 30 Jahren Eisforschung mit Fernerkundungsdaten wurden eine Vielzahl von Verfahren zur Bestimmung der Meereiskonzentrationen entwickelt. Diese Verfahren nutzen die vom Satelliten gemessenen Helligkeitstemperaturen zur Berechnung der Eiskonzentrationen. Grundlegend dabei ist auch eine Kenntnis über die Unsicherheit der abgeleiteten Eiskonzentrationen, um die Signifikanz beobachteter Ab- oder Zunahmen der Eisfläche vor dem Hintergrund natürlicher Schwankungen abzuschätzen. Die Unsicherheit wird aber auch benötigt für die Assimilierung von Eiskonzentration in numerische Wettermodelle. Dabei wird die Unsicherheit in der Eiskonzentration vor allem verursacht durch Schwankungen der Emissivität an der Oberfläche und den Einfluß atmosphärischer Größen wie Wasserdampf und Wolkenbedeckung. Darüber hinaus hängen die verschiedenen Verfahren zur Bestimmung der Eiskonzentration von der Wahl der Referenzpunkte ab. Diese stellen typische Helligkeitstemperaturen der involvierten Oberflächentypen dar.

In dieser Arbeit werden die Unsicherheiten des ARTIST Sea Ice (ASI) Verfahrens im Vergleich mit anderen Datensätzen der Eiskonzentration untersucht. ASI nutzt Helligkeittemperaturen, die bei 90 GHz gemessen werden. In einer ersten Studie werden ASI-Eiskonzentrationen und die Eiskonzentrationen aus anderen Verfahren mit in-situ Beobachtungen der Einskonzentrationen von Schiffsfahrten um die Antarktis verglichen. Nach einer Erweiterung von ASI um die Nutzung der Helligkeitstemperaturen des neuen Advanced Microwave Scanning Radiometer 2 (AMSR2) vergleichen wir ASI in einer zweiten Studie für die Arktis mit Eiskonzentrationen abgeleitet mit dem Comiso Bootstrap Verfahren (BST). Das BST Verfahren hat im ersten Vergleich mit den Schiffsbeobachtungen die besten Ergebnisse erzielt. In dem Vergleich für die Arktis ziehen wir zudem Daten aus optischen Verfahren und abgeleitete Eishelligkeitstemperaturen hinzu. Hier erweist sich ASI als das genauere Verfahren. Beide Vergleiche zeigen, dass ASI in der Lage ist mit Helligkeitstemperaturen verschiedener Radiometer und in beiden Hemisphären gute Ergebnisse zu erzielen. In einer dritten Untersuchung stellen wir den Einfluß variabler Emissivitäten an der Oberfläche und den Einfluß atmosphärischer Größen wie der Wasserdampf und die Wolkenbedeckung auf das ASI Verfahren dar. Bisherige Untersuchungen geschlossener Eisbedeckungen im Winter zeigen, dass die Schwankungen der abgeleiteten Eiskonzentrationen durch Schwankungen der Emissivität an der Oberfläche verursacht werden. Es wird gezeigt, dass für das ASI Verfahren darüber hinaus atmosphärischer Wasserdampf und die Wolkenbedeckung einen beträchtlichen Einfluß auf das Verfahren haben. Während eine Neuschneedecke auf dem Meereis die berechntete Eiskonzentration reduziert, erhöhen zusätzlicher Wasserdampf und Wolken die berechnete Eiskonzentration. Aufgrund der Ergebnisse für die soeben genannten Sensitivitäten wird eine Neuberechunung der oben genannten Referenzpunkte unabhängig für beide Hemisphären vorgeschlagen. Außerdem sollte

untersucht werden, ob die derzeitige Interpolierung zwischen diesen Referenzpunkten verbessert werden kann.

Contents

Chapter 1

Introduction

The polar ice covers have shown considerable changes since the start of satellite observations in the 1970s (Cavalieri and Parkinson, 2012; Parkinson and Cavalieri, 2012). Climate model simulations of the sea ice extent and its trends contradict these observations, especially in the Arctic, where sea ice declines much faster than expected (Kattsov et al., 2010; Stroeve et al., 2012). To improve climate model simulations, a comprehensive knowledge of the sea ice cover is essential, including knowledge about the uncertainties of the data. Recently, state-of-the-art earth system models have shown a considerable mismatch between model simulations and the true SIC as observed from satellites (Turner et al., 2013).

Passive microwave (PM) radiometers onboard polar-orbiting satellites are the backbone of today's sea ice concentration (SIC) retrievals. The radiometers measure raw antenna counts from which one derives the antenna temperature and then calculates the brightness temperatures (TB) of the Earth radiated to space. Based on these measurements of TB, once can obtain daily SIC on a hemispheric scale (e.g., Hallikainen and Winebrenner, 1992; Tucker et al., 1992; Winebrenner et al., 1992; Eppler et al., 1992; Steffen et al., 1992). In more than 30 years of research on PM radiometry, multiple SIC retrieval algorithms have been developed , e.g., NASA Team (Cavalieri et al., 1984), enhanced NASA Team (Markus and Cavalieri, 2000), Bootstrap (Comiso, 1986), NORSEX (Svendsen et al., 1983), SVENDSEN (Svendsen et al., 1987), and ASI (Kaleschke et al., 2001). These retrievals use TB measured at frequencies at 18/19 GHz, 36/37 GHz and near 90 GHz. Due to physical processes in the sea ice and snow cover (e.g., Barber et al., 1998; Wiesmann and Mätzler, 1999; Mätzler and Wiesmann, 1999; Markus and Cavalieri, 2000), varying atmospheric liquid water and water vapor content (e.g., Oelke, 1997; Fuhrhop et al., 1998; Kern, 2004; Andersen et al., 2006), and the influence of wind-induced surface roughness (e.g., Kern, 2004; Andersen et al., 2006), microwave emissivities from both the surface and the atmosphere show substantial variability, reduce the accuracy of SIC estimates. This leads to uncertainties specific for each retrieval algorithm due to the different frequencies involved.

The different retrieval algorithms use different sets of TB measuring at different

frequencies. Each frequency has a specific instantaneous field-of-view (IFOV), which is the area on the ground observed with one measurement. This leads to considerable differences in sensitivities to atmospheric opacity and to the variability in surface emissivities for measurements between 18/19 GHz or near 90 GHz. The different IFOV lead to different capabilities in retrieving inhomogeneities that actually define the surface properties. Such inhomogeneities can be leads, which occur on different spatial and temporal scales, ranging from a few tens of meters to kilometers and from hours to days. Other inhomogeneities can be different types and forms of ice, like newly-formed plane nilas, grease ice, pancake ice, snow-covered first-year ice, and old sea ice that eventually has deformed to rafted ice or pressure ridges due to shear forces. Additionally, the sensitivities to atmospheric opacity and surface variations are different at different frequencies (e.g., Oelke, 1997; Fuhrhop et al., 1998; Andersen et al., 2006). While lower frequency channels, for example 18/19 GHz, tend to be less sensitive to atmospheric contamination, higher frequency channels, for example near 90 GHz, are more sensitive (e.g., Lubin et al., 1997; Kern, 2004; Andersen et al., 2006). While the higher frequencies penetrate less into the ice or snow cover, the lower frequencies have a higher penetration depth and, thus, can be more sensitive to layering in the snow cover and intrusions in the sea ice from air bubbles, for example (Wiesmann and Mätzler, 1999; Mätzler and Wiesmann, 1999).

During the last 30 years, there have been a number of studies comparing different retrieval algorithms and multiple improvements for single algorithms. We present some that show sources of uncertainties. The widely used NASA Team and Bootstrap algorithm were found to exhibit considerable differences, the first due to layering effects in the snow, the second due to an influence of the physical temperature at the surface (Comiso et al., 1997). Andersen et al. (2006) investigated the performance of several retrieval algorithms regarding their sensitivity to the atmospheric influence by clouds and water vapour. They found the highest sensitivity for algorithms that use the horizontally-polarized channels at near 90 GHz. In another study, Andersen et al. (2007) explained variances in SIC close to 100 % to result from the variations of surface properties and not from changes in the real ice concentration. Ivanova et al. (2014) showed for 11 SIC retrieval algorithms that the negative trend in SIC is similar, but that individual retrieval algorithms can have considerable biases from the mean.

Although the higher frequency channels show higher sensitivities to atmospheric water vapour and clouds, near 90 GHz-based SIC algorithms have the advantage of considerably higher spatial resolution due to smaller IFOV. Svendsen et al. (1983) and (Svendsen et al., 1987, hereafter called SVENDSEN) were the first to use the higher frequencies that provide a higher spatial resolution. Improvements to SVENDSEN were presented in Lomax et al. (1995) and Lubin et al. (1997). Kern (2004) introduced a near 90 GHz retrieval algorithm that uses a radiative transfer model to reduce the error due to atmospheric contamination. The ARTIST Sea Ice (ASI) algorithm (Kaleschke et al., 2001) augments the SVENDSEN algorithm with a weather correction based on lower-frequency channels. It has been developed for TB measurements from the

Special Sensor Microwave/Imager (SSM/I) by Kaleschke et al. (2001) and adapted for measurements from Advanced Microwave Scanning Radiometer onboard EOS (AMSR-E) by Spreen et al. (2008).

In this thesis, we seek to

- enhance the ARTIST sea ice algorithm by using the new Advanced Microwave Scanning Radiometer 2 (AMSR2) TB measurements. With these data we are able to provide SICs at 3.125 km grid resolution which has only been possible before by considerable oversampling of available PM measurements;
- compare the most used SIC retrieval algorithms with a long surface-based observational record of ship-based observation of SIC to establish knowledge on the performance of the different algorithms;
- quantify the effect of varying surface emissivities and atmospheric contamination on the near 90 GHz ARTIST sea ice algorithm and assess the algorithm's uncertainties.

Based on these objectives, we address the following research questions:

1. What is the gain of information from a higher-resolution sea ice concentration retrieval?
2. Apart from the known advantages and disadvantages of lower- and higher-frequency-based sea ice retrievals, what is the actual performance when compared with a long data set of in-situ measurements?
3. Which parameters exhibit the highest influence on the variation of retrieved SIC under winter conditions? Can we estimate their influence?

Thesis outline

This thesis is organized as follows:

In Chapter 2, we provide the basic information to comprehend the investigations of this study by presenting the areas of interest, principles of remote sensing of sea ice concentration, and an overview of the data and methods used to answer the above presented research questions.

In Chapter 3, we compare different PM-derived sea ice concentrations with ship-based observations of the sea ice cover acquired around Antarctica. With this investigation, we quantify the differences among frequently-used sea ice concentration retrievals.

In Chapter 4, we introduce a new sea ice concentration data set, which is based on TB measured at 89 GHz from AMSR2, which has been placed in orbit in 2012. We investigate whether the new data reproduce surface details like leads that are visible on Moderate Resolution Imaging Spectroradiometer images under clear sky conditions and that are not captured by another frequently-used sea ice concentration data set.

In Chapter 5, we investigate the uncertainties of a near 90 GHz retrieval stemming from varying surface emissivities and atmospheric contamination by using simulations of a combined thermodynamic and emissivity model. We show how the differences and uncertainties that have been derived can be combined into a an uncertainty estimate for ASI and specify conditions under which ASI doe snot provide robust results .

In Chapter 6, we summarize the investigations presented before.

Publications

In the course of the research that has lead to this thesis, the following articles were published or accepted for publication:

Beitsch, A., Kaleschke, L., and Kern, S., 2014: Investigating High-Resolution AMSR2 Sea Ice Concentrations during the February 2013 Fracture Event in the Beaufort Sea. *Remote Sens.*, **6(5)**, 3841–3856, doi:10.3390/rs6053841.

Beitsch, A., Kern, S., and Kaleschke, L., 2015: Comparison of SSM/I and AMSR-E Sea Ice Concentrations with ASPeCt Ship Observations around Antarctica. *IEEE Transactions On Geoscience And Remote Sensing*, **53(4)**, 1985–1996, doi:10.1109/TGRS.2014.2351497.

Chapter 2

Fundamentals

The sections of this chapter give an overview on and present the necessary principles to understand the focus and the outcome of this work. The first section (Section 2.1) introduces the regions of the interest, the polar regions. The second section (Section 2.2) introduces principles of remote sensing to measure the sea ice concentration from space. The third section (Section 2.3) gives an overview of the data basis that we use in this work—the remote sensing data and the in-situ data. In the last section (Section 2.4), we introduce the microwave emission model MEMLSI that is used in this thesis.

2.1 The Regions of Interest

The Arctic and the Antarctic regions depict the polar regions of the Earth and constitute essential parts of the global climate system. Differential heating of the Earth's surface and resulting meridional heat transports of the excess heat in the tropics leaves the polar regions as the heat sinks to counterbalance the unequal distribution of energy on the globe. Their geographic position exposes the polar regions to extended periods of dark (polar night) and light (polar day) which has consequences for the general synopsis in the mid-latitudes. The widespread coverage of ice—be it glaciers on land, land-fast shelve ice or sea ice—imposes a high albedo onto the polar regions.

The dry, cold climate of the polar regions leads to another important characteristics for its role in the global climate system: the production of intermediate and deep water masses (e.g., Marshall and Schott, 1999). These water masses are in turn essential for the global heat distribution and the occur where a very cold atmosphere supports strong heat loss of the the upper ocean, which increases the upper layer density and leads to convection. The Nordic Seas (Greenland Sea, Iceland Sea, and Norwegian Sea) and the Labrador Sea in the Northern Hemisphere (see Figure 2.1), the Wedell and the Ross Seas in the Southern Hemisphere (see Figure 2.2) constitute regions for the production of deep-water masses. Considering environmental issues, the polar regions

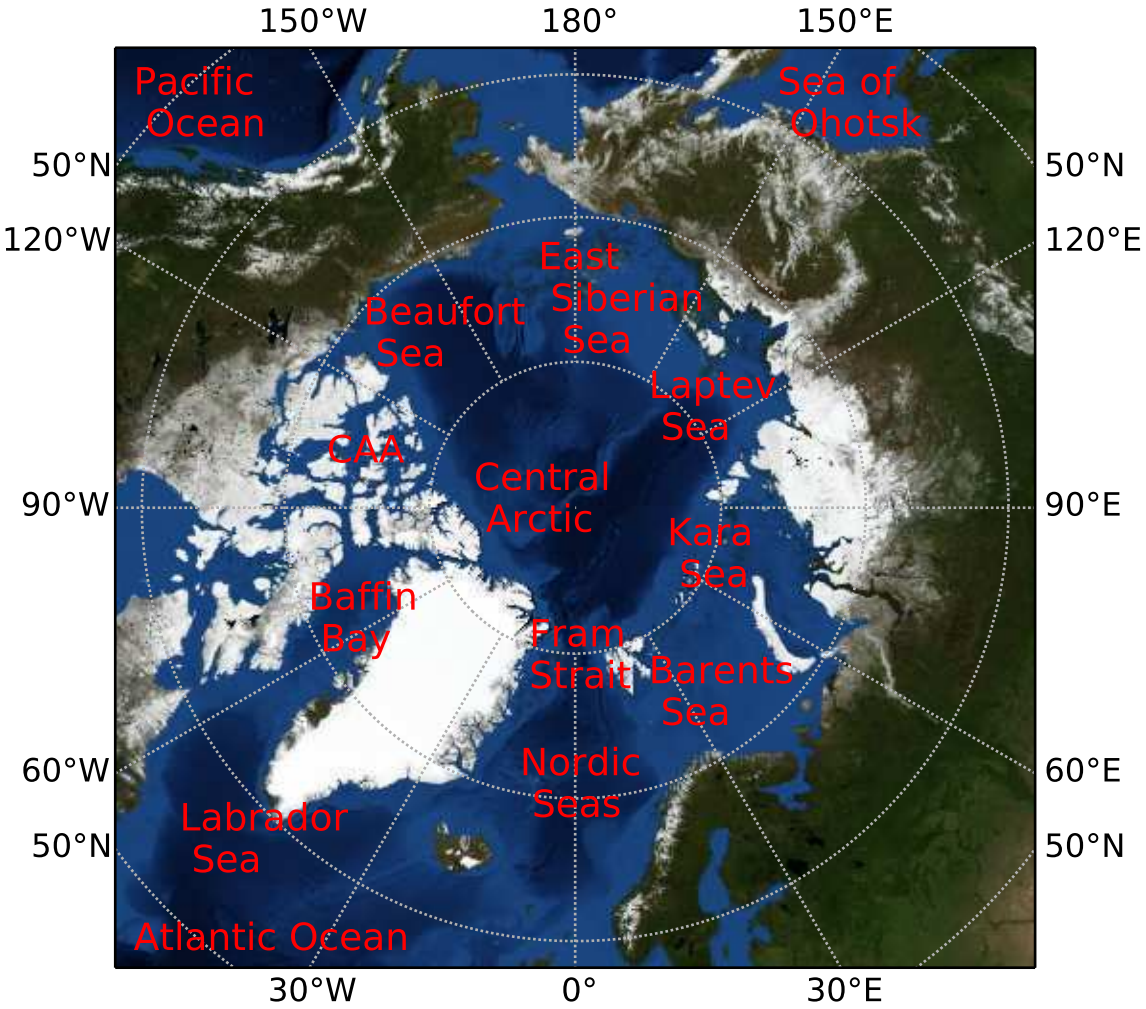

Figure 2.1: Map of the Arctic region.

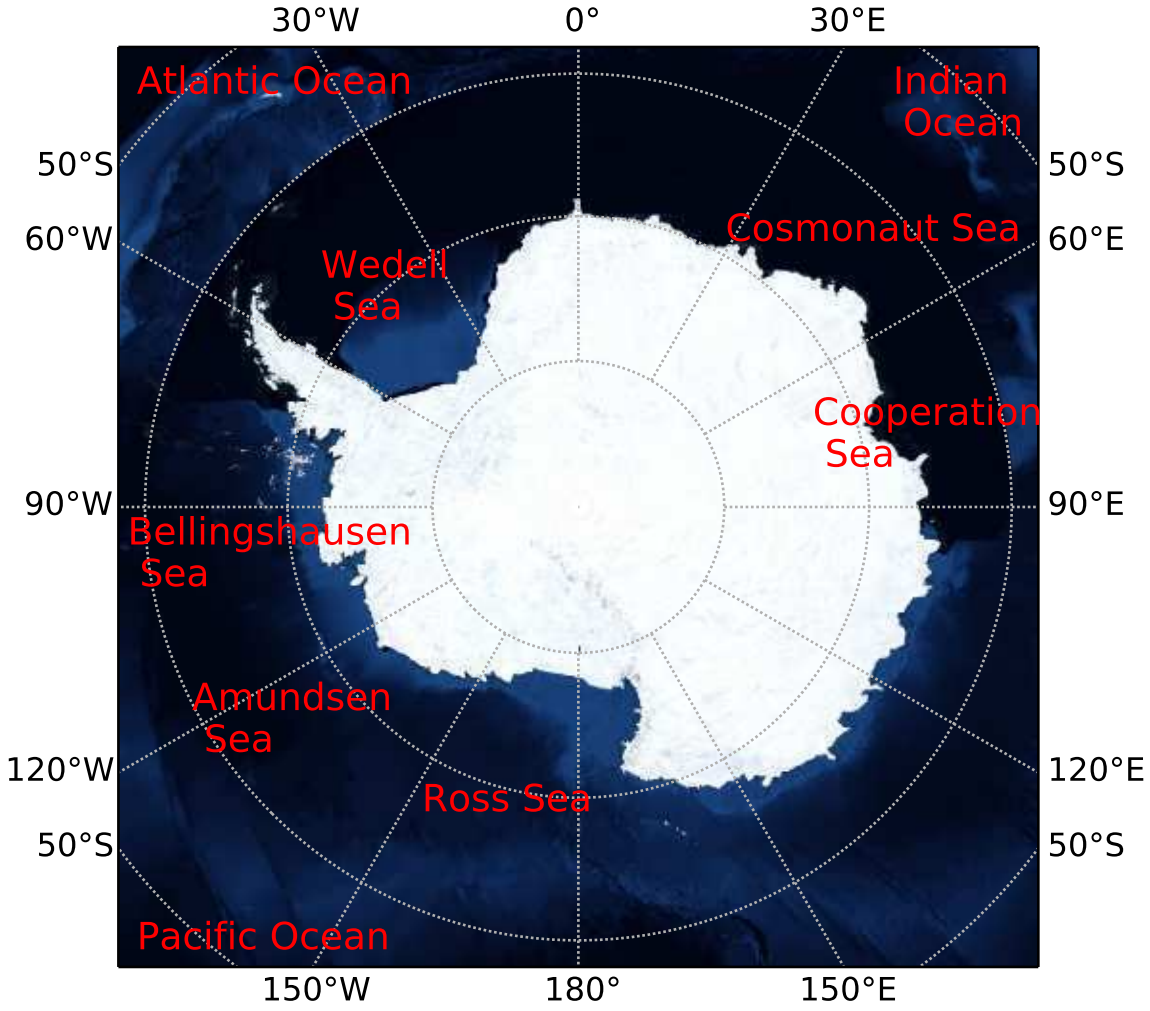

Figure 2.2: Map of the Antarctic region.

gain more and more attentions due to the accumulation of waste, chemicals and other disposals.

The polar regions also play a crucial role in current climate change: they indicate climate changes far earlier than other regions of the globe mainly due to the so-called Arctic Amplification (e.g., see Serreze and Francis, 2006; Serreze and Barry, 2011). Central to the polar regions is the the cryosphere which constitutes a complex system of water in its solid form ice including the above mentioned glaciers, shelve ice, and sea ice.

Apart from these similarities, the Arctic and the Antarctic region have very different characteristics. While the Arctic region can be characterized as an ocean surrounded by continents, Antarctica is a continent surrounded by oceans (Figures 2.1-2.2). The Arctic Ocean is a deep basin encompassed by the shallow marginal seas Beaufort Sea, Chukchi Sea, East Siberian Sea, Laptev Sea, Kara Sea, and Barents Sea. Deep-water masses enter the Arctic Ocean through Fram Strait. A shallower passage for water

masses are the Bering Strait, and the Canadian Arctic Archipelago (CAA). In contrast, the Antarctic is mostly surrounded by the deep basins from the Cosmonaut Sea, the Cooperation Sea, the Amundsen Sea, and the Bellingshausen Sea. Only parts of the Ross Sea and the Wedell Sea are shallow continental shelves. The different geographies of the two polar regions lead to very different characteristics : the Arctic is affected by warm ocean currents importing heat from the Atlantic ocean, while the Antarctic region is surrounded by a circumpolar current system, which inhibits heat import from lower latitudes and leads to extremely low temperatures on the continent. While cyclones can occur all year and penetrate the Antarctic sea ice cover with ocean swells breaking up the ice, the sea ice cover in the central Arctic Ocean is protected from ocean swell by the surrounding continents when the sea ice has developed. This has important implications for the sea ice formation, which is quite different for both hemispheres.

2.2 Sea Ice

While regional sea ice coverage have been shown to change significantly on interannual time-scales (Walsh and Chapman, 2001), the overall trend of Arctic sea ice extent and area are negative for the 30 years of observation (Cavalieri and Parkinson, 2012) and positive for Antarctica (Parkinson and Cavalieri, 2012). The knowledge of the hemispheric evolution of the sea ice during the last 30 years is to most parts based on passive microwave remote sensing of sea ice concentrations, which we introduce in the following section.

2.2.1 Principles of Remote Sensing of Sea Ice Concentrations

The sea ice concentration retrieval algorithms that we consider in this thesis are based on the radiative transfer equation, simplified for the microwave regime:

$$\mathrm{TB} = (1-\epsilon)\,\mathrm{T_{spc}} + \epsilon\,\mathrm{T_{sfc}}\,(1-\tau_{\mathrm{atm}}) + \tau_{\mathrm{atm}}\,\delta\mathrm{T_{atm}} + (1-\epsilon)\,\delta\mathrm{T_{atm}}\,\tau_{\mathrm{atm}}\,(1-\tau_{\mathrm{atm}}) \quad (2.1)$$

which is demonstrated following Svendsen et al. (1983). The brightness temperature TB measured in space is composed of four terms. The first term depicts the radiation from space $\mathrm{T_{spc}}$ that is, based on the emissivity ϵ, reflected from the surface and passes the atmosphere two times. The second term depicts the brightness temperature $\mathrm{T_{sfc}}$ emitted from the surface and attenuated through the atmosphere by the total atmospheric opacity τ_{atm}. The third term depicts the upwelling radiation from the atmosphere, where $\delta\,\mathrm{T_{atm}}$ is the weighted average atmospheric temperature in the lower troposphere. The fourth term depicts the downwelling atmospheric radiation reflected at the surface and transmitted back through the atmosphere. The emissivity ϵ can be

considered an effective emissivity, which is the emissivity that a PM radiometer detects in one measurement. The effective emissivity averages individual emissivities from different layers within the radiation's path. The contribution from space is very small and generally neglected. Since τ_{atm} is small for polar atmospheres, it is approximated by $\mathrm{e}^{-\tau_{\mathrm{a}}} = 1 - \tau_{\mathrm{a}}$.

The brightness temperature $\mathrm{TB}_{\mathrm{surf}}$, which is measured by a radiometer just above the surface or in the ideal case of a fully transparent atmosphere, can be expressed as the product of an effective temperature $\mathrm{T}_{\mathrm{eff}}$ and the emissivity of the surface ϵ_{surf}:

$$\mathrm{TB}_{\mathrm{surf}} = \epsilon_{\mathrm{surf}}\, \mathrm{T}_{\mathrm{eff}}. \tag{2.2}$$

Here, the effective temperature $\mathrm{T}_{\mathrm{eff}}$ contains the influence of the different temperatures within the profile of snow or snow and sea-ice: depending on the microwave frequency, the radiation received at the radiometer originates from different layers within the profile.

ARTIST Sea Ice Algorithm

Since the start of the Special Sensor Microwave/Imager (SSM/I), the 85 GHz data with a higher resolution than lower-frequency channels became available. The ARTIST Sea Ice algorithm (ASI Kaleschke et al., 2001) is an enhancement of the SVENDSEN algorithm (Svendsen et al., 1987), which was the first algorithm to use higher-frequency channels to retrieve SIC. ASI was adapted for measurements at 89 GHz from the Advanced Microwave Scanning Radiometer onboard EOS (AMSR-E Spreen et al., 2008). Here, we shortly explain how ASI derives sea ice concentrations (SIC) following Spreen et al. (2008):

Surface emissivity differences are similar for most ice types and considerably smaller than for open water. With the physical temperature having the same influence for horizontally and vertically polarized brightness temperatures (TB), the emissivity controls changes in TB. One can distinguish the different surface types ice and water also by using the brightness temperature polarization difference (at 89 GHz for AMSR-E) P_{89}, which is defined as

$$\mathrm{P}_{89} = \mathrm{TB}_{89\mathrm{V}} - \mathrm{TB}_{89\mathrm{H}} \tag{2.3}$$

with V for vertical and H for horizontal polarization. Svendsen et al. (1987) introduced an approximation for the influence of the atmosphere on P_{89}, which is valid for the horizontally stratified Arctic atmosphere and a diffusely reflecting surface for an incidence angle of $\approx 50°$. Then, the vertical atmospheric temperature profile can be replaced by an effective temperature and the atmospheric influence can be described by

$$P_{89} = P_{89,s}\, a_c = P_{89,s}\, e^{-\tau}\, (1.1\, e^{-\tau} - 0.11) \tag{2.4}$$

where τ denotes the atmospheric opacity and $P_{89,s}$ the surface polarization difference. Not only is the atmospheric influence a function of the ice concentration C, but also P_{89} depends on the atmosphere:

$$P_{89}(C) = P_{89,s}\, a_c = (C\, P_{89,s,i} + (1 - C)\, P_{89,s,w})\, a_c \tag{2.5}$$

where $P_{s,i}$ and $P_{s,w}$ denote surface polarization differences for ice and water, respectively. The atmospheric influence is a function of the sea ice concentration (Svendsen et al., 1987), because the water vapour content and cloud liquid water decrease with increasing ice cover. This is because reduced open water areas decrease evaporation. Using Equation 2.5, the polarization difference for an open water surface at 90 GHz becomes

$$P_w = a_w\, P_{89,s,w} \tag{2.6}$$

where the atmospheric influence and the surface polarization for open water are denoted as a_w and $P_{89,s,w}$. For a closed ice surface, the polarization difference accordingly becomes

$$P_i = a_w\, P_{89,s,i}. \tag{2.7}$$

These polarization differences define the so-called tie-points for the surface types open water (w, C=0) and sea ice (i, C=1). Using Taylor expansion of Equation 2.5 for values around open water (C=0) leads to

$$P_{89} = a_w\, C\, (P_{89,s,i} - P_{89,s,w}) + P_w \text{ for } C \to 0. \tag{2.8}$$

For values of sea ice (C=1), Equation 2.5 leads to

$$P_{89} = a_i\, (C - 1)\, (P_{89,s,i} - P_{89,s,w}) + P_i \text{ for } C \to 1. \tag{2.9}$$

In Equation 2.8 and Equation 2.9, higher order terms and the derivatives of the atmospheric influence a'$_w$=0 for C=0 and a'$_i$ = 0 for C=1 can be neglected (Spreen et al., 2008). We can rearrange Equation 2.8 and Equation 2.9 and substitute the atmospheric influence:

$$C = \left(\frac{P_{89}}{P_w} - 1\right) \left(\frac{P_{89,s,w}}{P_{89,s,i} - P_{89,s,w}}\right) \text{ for } C \to 0 \tag{2.10}$$

$$\mathrm{C} = \frac{\mathrm{P}_{89}}{\mathrm{P}_\mathrm{i}} + \left(\frac{\mathrm{P}_{89}}{\mathrm{P}_\mathrm{i}} - 1\right)\left(\frac{\mathrm{P}_{89,\mathrm{s,w}}}{\mathrm{P}_{89,\mathrm{s,i}} - \mathrm{P}_{89,\mathrm{s,w}}}\right) \text{ for } C \to 1. \tag{2.11}$$

Svendsen et al. (1987) derived $\mathrm{P}_{89,\mathrm{s,w}}/(\mathrm{P}_{89,\mathrm{s,i}} - \mathrm{P}_{89,\mathrm{s,w}} = -1.14$ from typical sea ice signatures. ASI interpolates between the solutions for C=0 (Equation 2.10) and C=1 (Equation 2.11) to retrieve SIC between open water and 100 % ice concentration using a third-order polynomial (Kaleschke et al., 2001),

$$\mathrm{C} = \mathrm{d}_3\,\mathrm{P}_{89}^3 + \mathrm{d}_2\,\mathrm{P}_{89}^2 + \mathrm{d}_1\,\mathrm{P}_{89} + \mathrm{d}_0. \tag{2.12}$$

The factors d_0 to d_3 are found by solving a linear equation system, which is determined by using Equation 2.10 and Equation 2.11 and their first derivatives. Then Equation 2.12 can be used to calculate the sea ice concentration C. For polarization differences outside a range between 0 and 1, C is set equal to zero for $\mathrm{P}_{89} > \mathrm{P}_\mathrm{w}$ and equal to one for $\mathrm{P}_{89} > \mathrm{P}_\mathrm{i}$.

Several studies have shown how sensitive the choice of the tie-points is on the retrieval (e.g., Lomax et al., 1995; Lubin et al., 1997; Kaleschke et al., 2001). Kaleschke et al. (2001) and Spreen et al. (2008) improved the retrieval by using several weather filters based on lower-frequency measurements of TB to reduce the influence of weather on the retrieval. For AMSR-E (Spreen et al., 2008), these filters include a threshold using the gradient ratio (GR) of the 36.5 and 18.7 GHz channels (Gloersen and Cavalieri, 1986), a threshold using GR of the 23.8 and 18.7 GHz channels (Cavalieri et al., 1995), and a filter, where ASI pixels were set to zero, when corresponding Bootstrap pixel (Comiso et al., 2003) are equal zero.

Spreen et al. (2008) introduced an error estimation for ASI using the standard deviations of the surface polarization differences $\mathrm{P}_{89,\mathrm{s,w}}$ and $\mathrm{P}_{89,\mathrm{s,i}}$ and the atmospheric opacity over open water τ_w and the atmospheric opacity over sea ice τ_i measured during the ship campaigns NORSEX and MIZEX (Svendsen et al., 1987), when all required quantities were measured simultaneously. The standard deviation in P_{89} is then given as

$$\begin{aligned}
\sigma_{\mathrm{P}_{89}} =& \sqrt{\left(\frac{\partial \mathrm{P}_{89}}{\partial \tau}\right)^2 \sigma_\tau^2 + \left(\frac{\partial \mathrm{P}_{89}}{\partial \mathrm{P}_{89,\mathrm{s,w}}}\right)^2 \sigma_{\mathrm{P}_{89,\mathrm{s,w}}}^2 + \left(\frac{\partial \mathrm{P}_{89}}{\partial \mathrm{P}_{89,\mathrm{s,i}}}\right)^2 \sigma_{\mathrm{P}_{89,\mathrm{s,i}}}^2} \\
=& [(\mathrm{C}\,\mathrm{P}_{89,\mathrm{s,i}} + (1-\mathrm{C})\,\mathrm{P}_{89,\mathrm{s,w}})^2 \\
& (-2.2\,e^{-2\,\tau} + 0.11\,e^{-\tau})^2\,\sigma_\tau^2 \\
& + (e^{-\tau}\,(1.1\,e^{-\tau} - 0.11)(1-\mathrm{C}))^2\,\sigma_{\mathrm{P}_{89,\mathrm{s,w}}}^2 \\
& + (e^{-\tau}\,(1.1\,e^{-\tau} - 0.11)\,\mathrm{C})^2\,\sigma_{\mathrm{P}_{89,\mathrm{s,i}}}^2]^{1/2}
\end{aligned} \tag{2.13}$$

The standard deviation of the ice concentration C follows from the polynomial in Equation 2.12:

$$\sigma_C = |\frac{\partial C}{\partial P_{89}} \sigma_P| = |\left(3\,d_3\,P_{89}^2 + 2\,d_2\,P_{89} + d_1\right)\,\sigma_P|. \tag{2.14}$$

Spreen et al. (2008) showed that σ_C decreases from 25 % to 5.7 % when C increases from 0 % to 100 % using the tie-points derived for SSM/I. Augmented with an estimation of the radiometric accuracy of lower frequency algorithms to a measuring uncertainty of 1 K for AMSR-E at 89 GHz, Spreen et al. (2008) assumes an overall accuracy of lower frequency algorithms of approximately 7 %. However, Cavalieri et al. (2006b) found discrepancies reaching 30 %. In general, Andersen et al. (2006, 2007) showed that for near 90 GHz retrieval this range is suitable at high SIC. But for cases with high cloud liquid water in the atmosphere, retrieval algorithms using TB at near 90 GHz may considerably overestimate sea ice concentration at low SIC.

2.3 Data Basis

In this section, we introduce the data sets used for the investigations in this thesis. These data sets can be grouped into the following classes:

- Remote sensing data from passive microwave radiometers on-board a platform in orbit around the Earth; we use brightness temperatures that are derived from the radiometer's measurements.
- In-situ observation of the sea ice cover from vessels navigating through the ice.
- Brightness temperature and emissivity data simulated by a combined thermodynamic snow/ice and emissivity model.

2.3.1 Passive Microwave Data

As explained in the previous Section, ASI uses near 90 GHz TB measurements to derive SIC. TB measurements at 85 GHz became available with the start of the Special Sensor Microwave/Imager (SSM/I), which has been launched onboard the Defense Meteorological Satellite Program (DMSP) satellites. The Special Sensor Microwave Imager/Sounder (SSMIS) replaced the SSM/I in 2003 and augments the SSM/I with several higher frequency channels to retrieve atmospheric parameters. The 85 GHz channels were replaced with channels at 91.655 GHz. The Advanced Microwave Scanning Radiometer onboard EOS (AMSR-E) started in 2003 and provided an improved spatial resolution. AMSR-E's near 90 GHz channels measured at 89.0 GHz. In 2012, Advanced Microwave Scanning Radiometer 2 (AMSR2) started measuring with improved spatial resolution at 89.0 GHz. Further explanation on SSM/I, SSMIS, and AMSR-E are provided in Section 3.2.2. AMSR2 will be further explained in Section 4.2.

2.3.2 ASPeCt Ship Observations

In this thesis, we compare passive-microwave derived SIC with visual ship-based observations of SIC around Antarctica. The ship-based observation were comprised in the Antarctic Sea Ice Processes and Climate (ASPeCt) program. The ASPeCt data will be further explained in Section 3.2.1.

2.4 Microwave Emission Modeling of Layered Snowpacks on Sea Ice (MEMLSI)

To quantify the influence of varying surface emissivities and changing atmospheric water content on the ASI algorithm, we use simulated data of emissivities and TB from a combined thermodynamic snow/ice and emissivity model, the Microwave Emission Modeling of Layered Snowpacks on Sea Ice (MEMLSI Tonboe, 2010; Tonboe et al., 2011) with an atmospheric radiative transfer model (Wentz and Meissner, 2000). MEMLSI is a sea ice version of the Microwave Emission Model of Layered Snowpacks (MEMLS) (Wiesmann and Mätzler, 1999; Mätzler and Wiesmann, 1999). MEMLS was developed for snow cover on land surfaces; MEMLSI is augmented to include models for sea ice dielectric properties and is valid in the 1-183 GHz region. The model considers scattering within snow and sea ice layers and distinguishes small brine pockets and air bubbles that serve as scatters in first-year ice and multi-year ice, respectively. The sea ice emission model relates microwave emissivity to physical properties in the sea ice and the overlying snow cover. Such properties include density, temperature, inclusions of snow crystals and brine. These properties directly influence the radiation in the microwave spectrum through attenuation, scattering and reflectivity.

The data that we use were simulated for the ESA-CCI Sea Ice Essential Climate Variable Project Round Robin Data Package (RRDP, Pedersen and Saldo, 2012). For the simulations with MEMLSI, the thermodynamic snow and ice model is driven by European Centre for Medium Range Weather Forecast (ECMWF) reanalysis ERA40 data. Parameters that drive MEMLSI include the surface air pressure, the 2 m air temperature, the dew point temperature, the 10 m wind speed, the incoming shortwave solar radiation and long-wave radiation, and the precipitation data. From these parameters, the thermodynamic model provides the microphysical variables needed in the emission model for a time step of 6 hours.

Based on the physical snow and ice properties like density, temperature, snow crystal, and brine inclusion size from the thermodynamic model, the emission model simulates the microwave attenuation, scattering and reflectivity in the snow and ice. Individual precipitation events and subsequent snow metamorphosis determine the vertical resolution in the snow. The model retains precipitation until a threshold of $1\,\mathrm{kg\,m^{-2}}$ is reached. The vertical resolution in the ice is 5 cm. From the simulated microwave

parameters—attenuation, scattering and reflectivity—surface emissivities and TBs are calculated for different frequency channels according to the scanning characteristics of the AMSR-E sensor. The atmospheric emission that contributes to TB as they are measured from space is simulated by using an atmospheric radiative transfer model (Wentz and Meissner, 2000).

Chapter 3

Comparison of SSM/I and AMSR-E Sea Ice Concentrations with ASPeCt Ship Observations around Antarctica[1]

We compare passive-microwave (PM) derived sea ice concentrations (SIC) with more than 21600 ship-based observations (OBS) of SIC acquired around Antarctica. PM SIC are derived from SSM/I-SSMIS and AMSR-E measurements in 1991–2009 and 2002–2010, respectively, with ARTIST Sea Ice (ASI), Comiso Bootstrap (BST), NASA-Team (NT), enhanced NASA-Team (NT2), and EUMETSAT OSI-SAF (OSI). We compare correlation coefficients (CC), root-mean-square-deviations (RMSD) and biases, separately for SSM/I-SSMIS data for algorithms ASI, BST, OSI, and NT, and for AMSR-E data for algorithms ASI, BST and NT2. With OBS SIC and PM SIC being on fundamentally different spatio-temporal scales, we develop a new co-location approach using daily-average along-ship-track SIC values. CC between OBS SIC and PM SIC agree within their uncertainty for all algorithms and sensors. Year-round CC values are around 0.85 (AMSR-E) and 0.82 (SSM/I); CC values are similar during summer, but drop significantly during winter. Year-round RMSD values range from 13 % (BST and OSI) to 17 % (NT) for SSM/I and from 12 % (BST) to 16 % (NT2) for AMSR-E. RMSD values are similar during summer, but decrease for winter: BST: 8 % for AMSR-E and 10 % for SSM/I. For AMSR-E, biases are below 0.5 % for BST and ASI but between 5 % (winter) and 9 % (summer) for NT2. For SSM/I, biases are smaller during summer: -0.7 % for BST to -7.8 % for NT, than winter: -3.6 % for BST to -13.9 % for NT. Overall, best agreement between OBS and PM SIC is found for BST.

[1] This chapter is published as: Beitsch, A., Kern, S., and Kaleschke, L., 2015: Comparison of SSM/I and AMSR-E Sea Ice Concentrations with ASPeCt Ship Observations around Antarctica. *IEEE Transactions On Geoscience And Remote Sensing*, **53(4)**, 1985–1996, doi:10.1109/TGRS.2014.2351497.

3.1 Introduction

The Antarctic continent and surrounding sea ice covered regions are vast and remote. Precise knowledge about the sea ice extent and concentration is needed for many applications in geoscientific research, e.g., for modeling the formation of deep water masses (Stossel, 2010), and for providing realistic boundary conditions for modeling quantities that are dependent on sea surface and ice conditions (Uotila et al., 2011; Donlon et al., 2012). The only tool to receive weather- and daylight-independent daily coverage of the current ice situation is satellite microwave radiometry. Measured brightness temperatures are input to retrieval algorithms that detect sea ice concentration (SIC), which, among other differences, use distinct combinations of frequencies and polarization to retrieve SIC. Validation of retrieved SIC is possible by comparing with ground truth data, for example from vessels navigating through the sea ice cover. The longest ship-based observation (OBS) data set of the Antarctic sea ice cover is available through the Antarctic Sea Ice Processes and Climate (ASPeCt) program, which collects observations that have been carried out following the ASPeCt standards, that are also known as the ASPeCt protocol. Several studies have been using single or sequences of cruises that contribute to the ASPeCt data as a ground truth data source for comparison with satellite passive microwave (PM) SIC products based on Special Sensor Microwave/Imager (SSM/I), Special Sensor Microwave Imager/Sounder (SSMIS) and Advanced Microwave Scanning Radiometer for the Earth Observing System (AMSR-E) measurements (Worby and Comiso, 2004; Knuth and Ackley, 2006; Ozsoy-Cicek et al., 2009). However, to our knowledge, there has not been a study using all available ASPeCt data extended by OBS from cruises in recent years and comparing them with the most used SIC retrieval algorithms. In this study, we want to assess the quality and performance of the most used SIC retrieval algorithms by comparing with an extended ASPeCt data set around Antarctica. Moreover, we want to infer if there are significant differences among the tested algorithms or if there exists one algorithm that we can recommend as the most reliable algorithm providing data of daily PM-derived SIC.

Prior to this work, Worby and Comiso (2004) investigated the sea ice edge derived from SIC data with two different algorithms, namely enhanced NASA Team (NT2) and Bootstrap (BST), based on SSM/I measurements and ASPeCt data in the years 1989–2000. Regarding geographical latitude, they find an accurate detection of the ice edge between March and October with maximum mean differences of 0.11°. Sea ice concentrations that are derived using BST give best results. Correlations are reduced during the melt season (November–February), when the sea ice and its snow cover become wet and flooded, so that surface signatures appear as a mixture of ice and open water to microwave sensors. Tekeli et al. (2011) examine data from field cruises in West Antarctica, comparing snow and ice properties derived by Envisat Advanced Synthetic Aperture Radar (ASAR), AMSR-E measurements and ASPeCt observations. Especially during the melt season, radar properties of thick first-year and multi-year ice are altered and a correct interpretation of observed radar backscatter values and

their variation over time becomes difficult to make. Kern (2004) compares about 850 OBS taken during several cruises in 1994–1998 with BST, the PELICON algorithm (Heygster et al., 1996), and the SEA LION algorithm (Kern, 2001; Kern and Heygster, 2001). All algorithms underestimate OBS SIC by 5 % to 17 % and show correlations below 0.6. Knuth and Ackley (2006) compare SSM/I-based NT SIC and BST SIC with OBS SIC from 3 cruises and 1 helicopter-based data set during 1999–2004. While from December to mid-February PM SIC over- and underestimate OBS SIC to an equal amount, PM SIC provide better estimates of OBS SIC during mid-February to April, when air temperatures drop. Correlations tend to be higher for fall data. Estimates of NT's maximum error (∼15 %) exceed those of BST (∼10 %) and the ∼10 % observation error for OBS. Weissling et al. (2009) confirm the average accuracy of ASPeCt SIC observations to be 10 % or better. In accordance with Nihashi et al. (2005), Knuth and Ackley (2006) find floe size and resolution as the most contributing factors of PM SIC's underestimation in a medium range sea ice concentration regime (<70 %). Ozsoy-Cicek et al. (2009) examine AMSR-E-based SIC of NT2 and BST for their accuracy in detecting the sea ice concentration, the sea ice extent and the location of the sea ice edge and compare them with ASPeCt protocol-based OBS. A good correlation was found inside the ice pack, but the correlation reduced in the Marginal Ice Zone (MIZ). Both sets of SIC, NT2 and BST, tend to underestimate low ice concentrations and show the location of the ice edge further south than in-situ measurements. This becomes especially apparent during melting conditions. Ozsoy-Cicek et al. (2011) make similar investigations for other cruises finding a low ice concentration bias with AMSR-E-based sea ice extents showing the tendency to underestimate US National Ice Center ice edges.

Despite this number of studies using single cruise observational data sets or a limited number of years from the ASPeCt data, there has not been—to our knowledge—a comparison of the full record of ASPeCt ship-based SIC observations with SSM/I-SSMIS and AMSR-E SIC. Here, we present a comparison of OBS SIC from extended ASPeCt data—that we regard as ground truth—with different PM SIC products. We append additional OBS SIC to the freely available ASPeCt data set (`http://aspect.antarctica.gov.au/`) from other cruises in 2006–2011 where SIC has been observed according to the ASPeCt protocol (Worby et al., 1999). For the comparison, we use different PM SIC to compare with the extended ASPeCt data. Four of the PM SIC data sets are based on SSM/I-SSMIS measurements and three data sets are based on AMSR-E measurements. We do a third comparison, in which we compare two algorithms, namely BST and ASI, that provide SIC that are based on measurements of both sensors, SSM/I-SSMIS and AMSR-E. This henceforth called sensor comparison emphasizes differences due to the different spatial resolutions of the sensors. We assess the performance of PM SIC by calculating correlation coefficients, root-mean-square-deviations (RMSD) and bias with respect to OBS SIC. Eventually, we are able to rank the sea ice concentration retrieval algorithms used for comparison in this study.

The paper proceeds in the following way: Section 2 gives details about the sensors

and the PM sea ice concentration data used, as well as an explanation of the method we apply to compare those data sets with ship-based observation. Section 3 describes the results for the different comparisons, namely the SSM/I-SSMIS-based comparison, the AMSR-E-based comparison, and the sensor comparison. In Section 4, we discuss our results and we end with our conclusions in Section 5.

3.2 Data and Methods

3.2.1 The Reference Ground-Truth Data Det: the extended ASPeCt Data Set

The ASPeCt data archive contains data from 81 voyages and 1663 aircraft-based observations for the period 1980–2005 (Worby et al., 2008). The data contain each individual observation, including characteristics of different ice types and snow cover. We use the total SIC, which—among other quantities—is estimated visually from the ship's bridge typically every hour while the ship is within an ice cover. A single ship observation accounts for an elliptically shaped area with about 1 km semi-minor axis. The ellipse's semi-major axis is aligned along the ship track. Ideally, the observation area should be a disc of 1 km radius. However, due to the ship's movement and the average duration of each observation of 5 to 10 minutes, this disc is distorted to an ellipse. With reduced visibility due to fog, clouds or precipitation, the area of observation can be even further reduced. Each individual OBS SIC is compared with the value from a PM SIC grid cell co-located to that location as will be described later.

We extend the ASPeCt data set with sea ice observations from cruises in 2006–2011. The ice observations on these cruises have been carried out according to the ASPeCt protocol. The appended data were collected on the following cruises:

- WWOS (September–October 2006; S. Willmes, pers. comm.; Haas et al. (2009)),
- SIMBA and SIPEX (September–October 2007; B. Ozsoy-Cicek, pers. comm.; Ozsoy-Cicek et al. (2011)),
- ODEN and PALMER (December 2007–January 2008, December 2008–January 2009, January–February 2009; A. H. Tekeli, pers. comm.; Tekeli et al. (2011)),
- ICEBELL (November–December 2010; S. Ackley, pers. comm.)
- ODEN (December 2010–January 2011; S. Ackley, pers. comm.)

Limitations exist for the accuracy of the ASPeCt observations, i.e., OBS SIC. Total SIC is estimated to the nearest 10 %, which can give a rounding error of up to 5 %. A human ice observation is subjective and prone to contain errors which may vary

between observers and which are difficult to quantify. However, tests with different observers have shown that simultaneous observations of total SIC rarely differ by more than 10 % (Worby and Comiso, 2004). Due to the duration of a single ice observation, the SIC estimate can represent an average of the real ice situation (Weissling et al., 2009). Especially in the MIZ, SIC changes can be abrupt over short time scales with alternating bands of open water and consolidated ice. Depending on the weather situation, visibility can be low, reducing the validity of the observed SIC value. To ensure as much consistency as possible, the ASPeCt data have been taken through quality control processes (Worby et al., 1999). The analysis carried out by Weissling et al. (2009) further that the average accuracy of ASPeCt SIC observations is 10 % or better.

3.2.2 Sea Ice Concentrations from Satellite Data

The SSM/I instrument has been launched onboard the Defense Meteorological Satellite Program (DMSP) satellites. These satellites circuit the Earth in a sun-synchronous, near-circular, polar orbit. During one day, a complete coverage of the polar regions is achieved. The instrument is a multichannel PM radiometer scanning the ground scene at constant angle of about 53 °incidence angle (Hollinger et al., 1987). With the launch of DMSP F-16, SSM/I has been replaced by its successor, the SSMIS instrument. SSMIS augments SSM/I's imaging channels by several atmospheric sounding channels, but still holds SSM/I's capabilities in recording brightness temperatures (TB) with imaging channels that are relevant for sea ice concentration retrievals, namely the 19 GHz, the 22 GHz, the 37 GHz and the 85 GHz imaging channels. The 85 GHz data provide higher spatial resolution and thus a finer grid resolution in contrast to the low-frequency channels usually used for sea ice concentration retrievals; the area of one 85 GHz grid cell is just one fourth of the grid cell area of the low-frequency channels. 85 GHz data became only usable with DMSP F-11 in late 1991; for SSM/I on DMSP-F8 and DMSP-F10, the 85 GHz channels were too noisy at time and could not be used (Tateyama and Enomoto, 2001). For coherency, data from SSM/I and SSMIS have been inter-calibrated (Yan and Weng, 2008).

The AMSR-E instrument has been launched aboard the Aqua satellite (Kawanishi et al., 2003). Like the DMSP satellites, Aqua is on a sun-synchronous, near-circular, polar orbit. The AMSR-E instrument scans at similar frequencies and at a similar incidence angle like the SSM/I and SSMIS instruments but has an improved spatial resolution in comparison to SSM/I and SSMIS instruments (see Table 3.1). For instance, the resolution of the AMSR-E 89 GHz channels is about three times finer than for the SSM/I 85 GHz channels, which reduces the 85/89 GHz footprint area by a factor of 8 (Spreen et al., 2008).

From here onwards, we refer to the combined SIC data based on SSM/I and SSMIS measurements when we mention SSM/I.

Table 3.1: Footprint sizes of the different channels of SSM/I (Hollinger et al., 1990), SSMIS (Grumman, 2002), and AMSR-E (Kawanishi et al., 2003).

Frequency (GHz)	19.35(SSM/I)	22.235(SSM/I)	37.0(SSM/I)	85.5(SSM/I)
	19.35(SSMIS)	22.235(SSMIS)	37.0(SSMIS)	91.655(SSMIS)
	18.7(AMSR-E)	23.8(AMSR-E)	36.5(AMSR-E)	89.0(AMSR-E)
SSM/I (km x km)	43x69	40x60	28x37	13x15
SSMIS (km x km)	45x74	45x74	28x45	13x15
AMSR-E (km x km)	16x27	18x32	8x14	4x6

3.2.3 Sea Ice Concentration Retrieval Algorithms

The sea ice concentration data used in the SSM/I comparison are based on the ARTIST Sea Ice (ASI), the NASA Team (NT), the Bootstrap (BST) and EUMETSAT's OSI-SAF (OSI) retrieval algorithms. In the AMSR-E comparison, we use the enhanced NASA Team (NT2) algorithm instead of NT. Moreover, OSI SIC are not available based on AMSR-E data. An overview of the algorithms that we compare is given in Table 3.2. All algorithms use a set of brightness temperature values—so-called tie-points—that account for 0 % and 100 % ice concentration. These tie-points have been derived from observations of different surface types like open water and sea ice separately for each of the algorithms. Tie-points represent typical radiometric signatures of these surface types. However, these signatures may vary considerably due to temperature changes, ice and snow property changes and water vapor in the atmospheric column between the surface and the radiometer onboard a satellite . These variations can result in sea ice concentration biases and differences among the different algorithms.

NT uses 19 GHz and 37 GHz TB values to compute TB polarization ratios (PR) and gradient ratios (originally described in Cavalieri et al. (1984); Gloersen and Cavalieri (1986)). The main SIC information comes from PR at 19 GHz. NT SIC has a grid resolution of 12.5 km x 12.5 km for AMSR-E and 25 km x 25 km for SSM/I.

NT2 is an enhancement of the NT algorithm that has been designed to mitigate some of the problems inherent to NT (Markus and Cavalieri, 2000). Besides 19 GHz and 37 GHz channels, it uses 85 GHz (SSM/I) or 89 GHz (AMSR-E) TB values to compute TB polarization ratios (PR) and gradient ratios. The main SIC information again comes from PR at 19 GHz. The other channels included mitigate the influence of different ice types and layering in the snow that caused problems with NT. A weather-correction is applied that uses a catalogue of simulated SIC depending on standard atmospheric states. NT2 SIC has a grid resolution of 12.5 km x 12.5 km for AMSR-E and 25 km x 25 km for SSM/I.

For Antarctica, BST utilizes vertically polarized TB values measured by the 19 GHz and 37 GHz channels (Comiso, 1995; Comiso et al., 2003). The BST algorithm interpolates between TB value pair clusters forming for 0 % and 100 % SIC in TB space.

BST SIC has a grid resolution of 12.5 km x 12.5 km for AMSR-E and 25 km x 25 km for SSM/I.

OSI SIC (EUMETSAT, 2011; Eastwood et al., 2011) are retrieved from a hybrid algorithm based on BST and the Bristol algorithm (Smith, 1996). It uses TB values measured by the 19 GHz and 37 GHz channels. Instead of a weather filter, OSI incorporates an atmospheric correction through the use of a radiative transfer model. OSI SIC has a grid resolution of 10 km x 10 km for SSM/I.

ASI uses 85 GHz (SSM/I) and 89 GHz (AMSR-E) TB polarization difference to calculate SIC from tie-points for 0 % and 100 % ice concentration (Kaleschke et al., 2001; Spreen et al., 2008). Using the higher-frequency TB measurements reduces the footprint size and leads to an increased spatial resolution. As a trade-off, these channels are more sensitive to influences from atmospheric cloud liquid water and water vapor on TB (Oelke, 1997). ASI SIC has a grid resolution of 6.25 km x 6.25 km for AMSR-E and 12.5 km x 12.5 km for SSM/I.

Except OSI, the SIC retrieval algorithms use the gradient ratio of vertically polarized 19 GHz and 37 GHz TB values to filter out spurious SIC over open water (Gloersen and Cavalieri, 1986; Cavalieri et al., 1995). A second weather filter involves vertically polarized 19 GHz and 22 GHz (AMSR-E: 23 GHz) TB values. However, these filters can lead to a truncation of low SIC and of SIC associated with new ice due to the contribution from atmospheric parameters like cloud liquid water or water vapor (Andersen et al., 2006). But, an increase of such parameters can also lead to erroneously increased SIC. This increase is more pronounced for low SIC (Andersen et al., 2006).

For AMSR-E, NT2 and BST data were obtained from the National Snow and Ice Data Center (NSIDC) as part of the (*AMSR-E/Aqua Daily L3 12.5 km Brightness Temperature, Sea Ice Concentration, & Snow Depth Polar Grids data set*; Cavalieri et al., 2003). The ASI SIC used here originate from a re-processing of the AMSR-E TB time series until 2011. This data set is available via the Integrated Climate Data Center at the University of Hamburg (ICDC, `http://icdc.zmaw.de`). Note that the tie-points used for this re-processing have been developed for the Arctic and have not yet been adapted to meet the perhaps different conditions in the Antarctic (Spreen et al., 2008). For SSM/I, NT and BST, were obtained from NSIDC, as part of the (*Sea Ice Concentrations from Nimbus-7 SMMR and DMSP SSM/I-SSMIS Passive Microwave Data*; Cavalieri, D. J., and C. Parkinson, and P. Gloersen, and H. J. Zwally, 1996) and the (*Bootstrap Sea Ice Concentrations from Nimbus-7 SMMR and DMSP SSM/I-SSMIS data sets*; Comiso, 1999). OSI-SAF SIC (EUMETSAT, 2011) were downloaded from ICDC (`http://icdc.zmaw.de`), as were ASI SIC (Integrated Climate Data Center (ICDC), 2012).

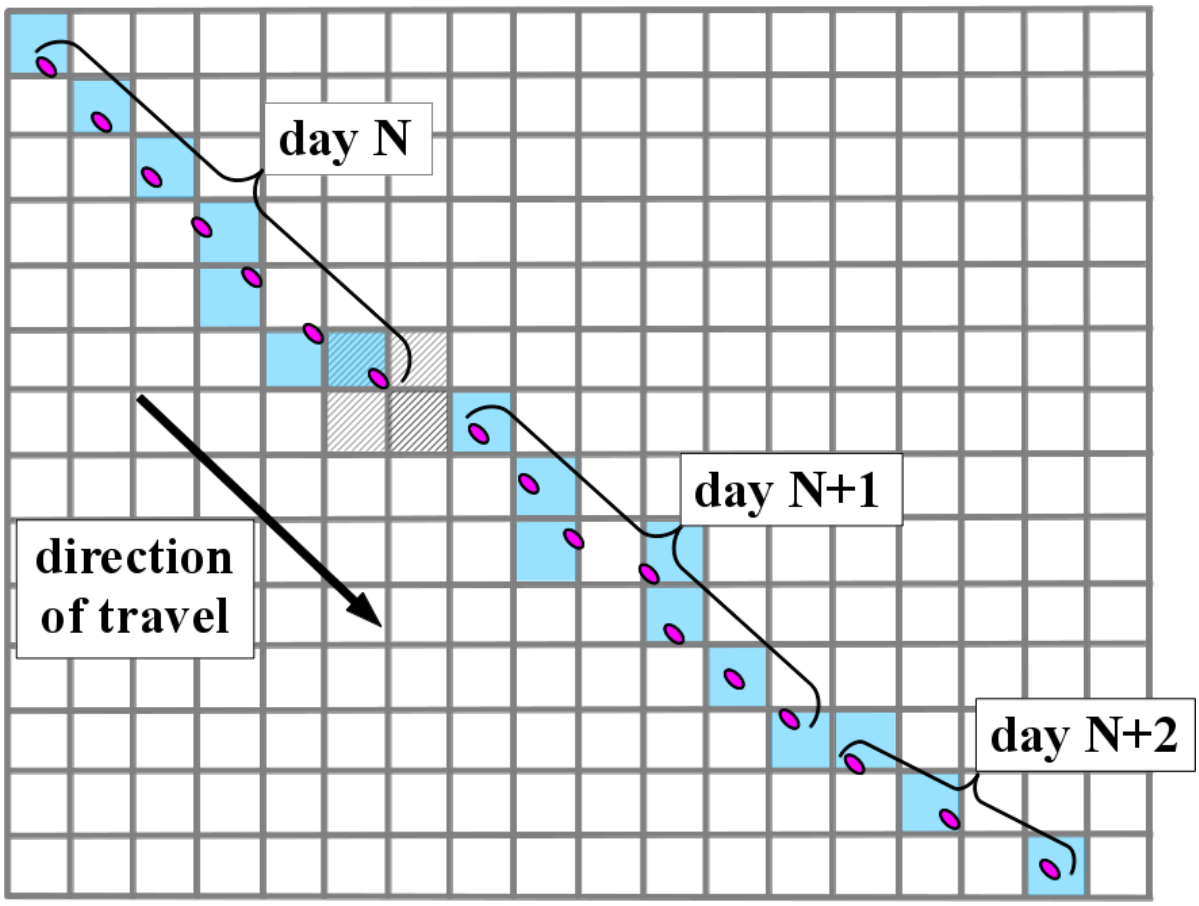

Figure 3.1: Scheme of the co-location method. See text for explanation.

Table 3.2: Overview of the sea ice concentration algorithms; "V" and "H" refer to vertical and horizontal polarization, respectively.

Algorithm	**Acronym**	**Frequencies**	**References**
ARTIST Sea Ice	ASI	85/89V, 85/89H	Svendsen et al. (1987), Kaleschke et al. (2001), Spreen et al. (2008)
Bootstrap Comiso	BST	19V, 37V	Comiso et al. (1997), and references therein
Bristol	BRI	19V, 19H, 37V, 37H	Smith (1996)
EUMETSAT OSI-SAF	OSI	19V, 19H, 37V, 37H	EUMETSAT (2011), Eastwood et al. (2011), Tonboe and Nielsen (2011)
NASA-Team	NT	19V, 19H, 37V	Comiso et al. (1997), and references therein
NASA-Team-2	NT2	19V, 19H, 37V, 37H, 85/89V, 85/89H	Markus and Cavalieri (2000)

3.2.4 Co-location and Comparison Method

Ship OBS represent sea ice conditions on a scale on the order of 1 km for a defined time. An average speed of 4 knots (about 7 km/h) is a reasonable assumption, if a ship crosses the sea ice cover during navigable sea ice conditions. Therefore, during one day, a ship is able to transit a distance of 150-200 km, which corresponds to 12-16 grid cells with 12.5 km resolution; during light ice conditions, the ship's speed and the distance traveled are accordingly larger. In contrast, PM SIC are daily averages. Data from several satellite overpasses from different times of one day are combined into one PM SIC value. In addition, this PM SIC value represents sea ice conditions on a scale on the order of 10-50 km. Temporal and spatial scales between OBS SIC and PM SIC are therefore quite different. It can be expected that OBS SIC is more variable than PM SIC, and a direct comparison of OBS SIC and PM SIC as they are is therefore questionable. As a solution of this caveat, we suggest to compare both data sets on a daily along-track average basis to align the different spatial and temporal scales of ship-based observations with the satellite data.

Throughout this paper, the co-location of OBS SIC with PM SIC is as follows: PM SIC are transformed onto a Cartesian grid (Fig. 3.1). The distance to the center of the surrounding PM SIC grid cells is computed for each OBS SIC location, as shown in Fig. 3.1 by the hatched pixels for the last ship position on day N. The grid cell

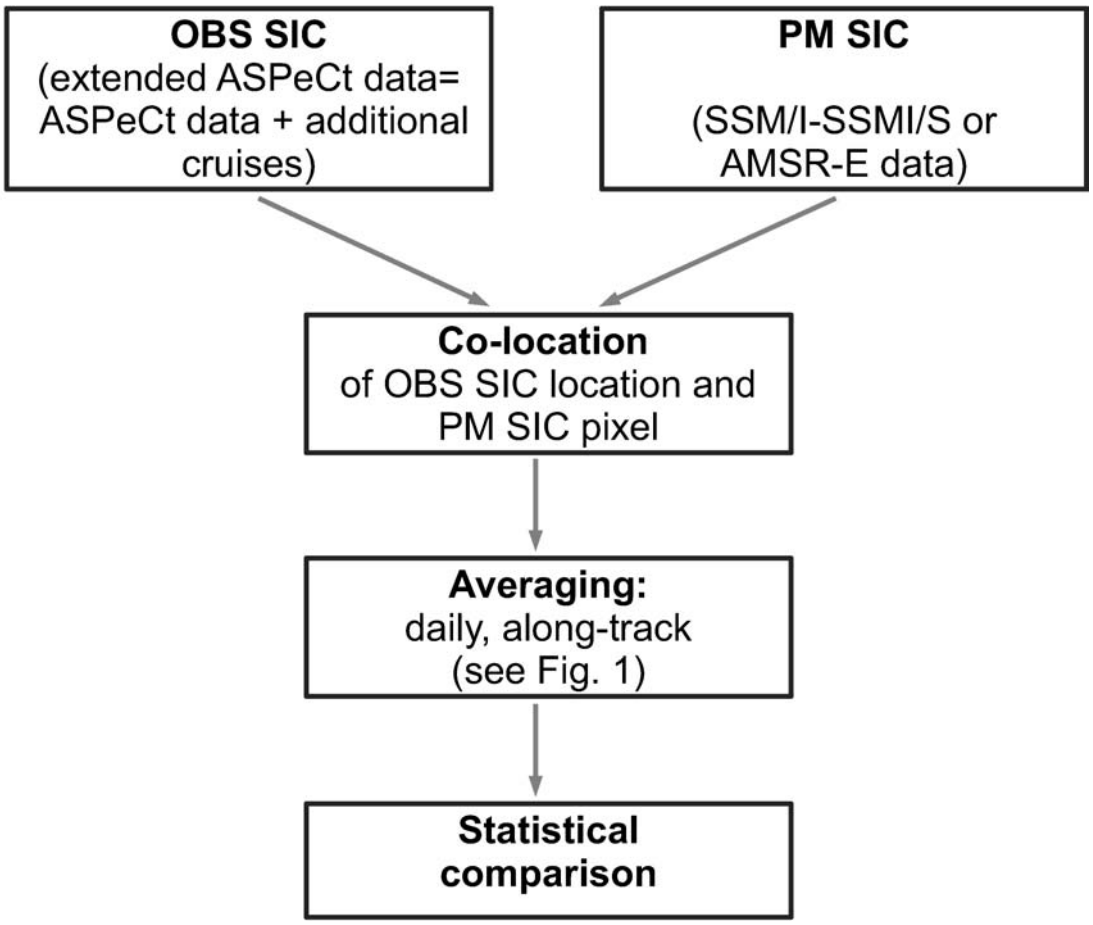

Figure 3.2: The analysis structure in this investigation shown in flow chart form.

with the minimum distance is selected for the comparison, which is shown by the blue colored pixels in Fig. 3.1. After the co-location, we compute the average along-ship track OBS SIC for all observations of one day (N_{day}) and the average PM SIC for all N_{day} co-located PM SIC grid cells (see Fig. 3.2).

For a single point in time, we require all data sets to provide a value: if one of the data sets has a missing value, the specific point in time is not used for the comparison. For the SSM/I comparison, this procedure yields a period from December 1991 until February 2009 with 21625 OBS/PM SIC data pairs. Limits in the comparison time frame are due the 85 GHz channels only being reliably available from the start of DMSP F-11 in December 1991 (see Section 3.2.2) and from the reprocessed OSI data ending in 2009. For the AMSR-E comparison, we investigate the period from August 2002 until December 2010 with 3871 OBS/PM SIC data pairs. For the daily along-track averaging, cases with $N_{day} < 3$ were discarded. This led to 1132 SIC daily averages in total to be used for our SSM/I comparison, 516 of which were from winter months (April–September) and 616 from summer months (October–March). For the AMSR-E comparison, we obtain 320 SIC daily averages, 84 of which were from winter months and 236 from summer months.

3.2.5 Statistical Comparison

We assess the performance of the different PM SIC methods compared to OBS SIC by calculating the correlation coefficient, the root-mean-square-deviation (RMSD) and the bias, which we define here as the mean difference between PM SIC and OBS SIC. Since SIC data are not normally distributed (see in Fig. 3.4, Fig. 3.7 and Fig. 3.9), we calculate Spearman rank correlation coefficients (denoted as r from hereon) instead of Pearson's product moment correlation coefficients for our comparison of PM SIC and OBS SIC.

3.3 Results

3.3.1 SSM/I period

The tracks of the ships from which the ice concentration data used in our comparison are shown in Fig. 3.3. Positions are overlaid onto an ASI sea ice extent map for 7 September 2005 based on SSM/I data. Due to the advantage of a long comparison period, SIC were collected all around Antarctica. Only an area between 0° and 30° E and 60° and 55° S shows no ship tracks. This area is usually covered by sea ice only at the end of the cold season.

The distribution of daily mean SIC in tenth of 100 % for OBS, ASI, OSI, NT, and BST shows only little differences among the compared SIC algorithms in the 5-15 % to 55-65 % bins (Fig. 3.4, upper panel). In other bins in the histogram, several differences exist. In general, the PM data tend to overestimate SIC values below 25 %, while for high SIC values individual differences occur. In the 75-85 %-bin, NT tends to overestimate SIC. In the >95 %-bin, besides BST, all PM data sets underestimate OBS SIC. During summer, differences only exist in the very low SIC regime (0-5 %-bin) and for very high SIC (>95 %-bin) (Fig. 3.4, middle panel). During winter, however, differences are more pronounced: NT strongly overestimates OBS in the 75-85 %-bin, ASI and OSI overestimate OBS in the 85-95 %-bin and in the >95 %-bin, only BST comes close to the number of SIC values accounted for by OBS (Fig. 3.4, lower panel).

Fig. 3.5 and Table 3.3 summarize the statistical comparison between the individual PM SIC and OBS SIC for the SSM/I data. The differences in the correlation coefficients r lie within the uncertainty of the correlation: BST: $r = 0.82 \pm 0.03$, OSI: $r = 0.83 \pm 0.03$, ASI: $r = 0.80 \pm 0.03$, NT: $r = 0.80 \pm 0.03$. The uncertainty is estimated separately for each satellite product by a Monte-Carlo simulation of the data and 1000 repeated calculations of r. During winter, correlations drop down to $r = 0.67 \pm 0.04$ for BST, $r = 0.70 \pm 0.04$ for OSI, $r = 0.60 \pm 0.05$ for ASI, and $r = 0.65 \pm 0.04$ for NT, respectively. During summer, correlations slightly increase, although the different values for r usually stay within the uncertainty range (BST: $r = 0.86 \pm 0.04$, OSI: $r = 0.87 \pm 0.04$, ASI:

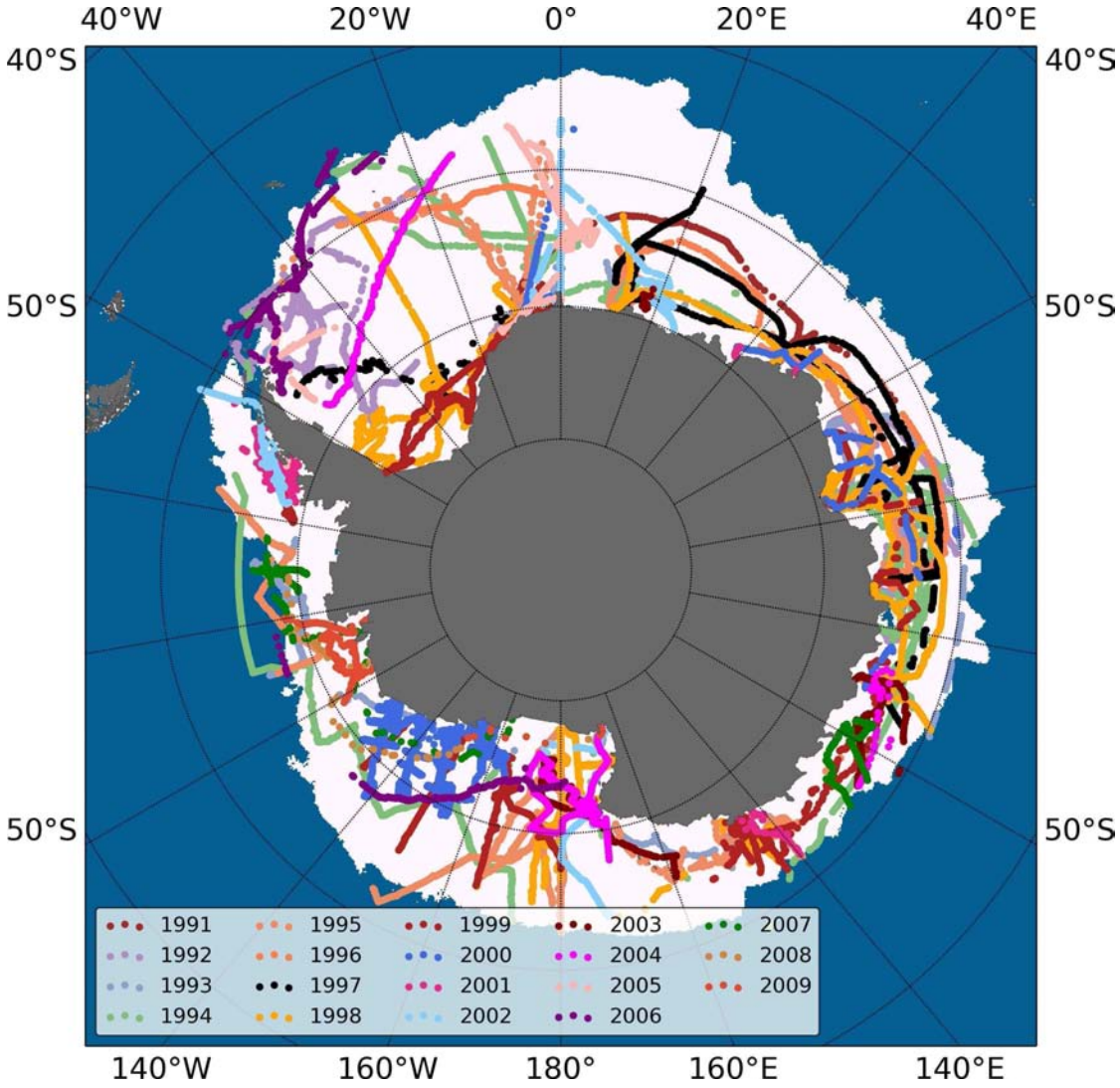

Figure 3.3: ASPeCt ship tracks (OBS) during the SSM/I comparison period (1991–2009) projected onto an ASI sea ice extent map of September 7, 2005.

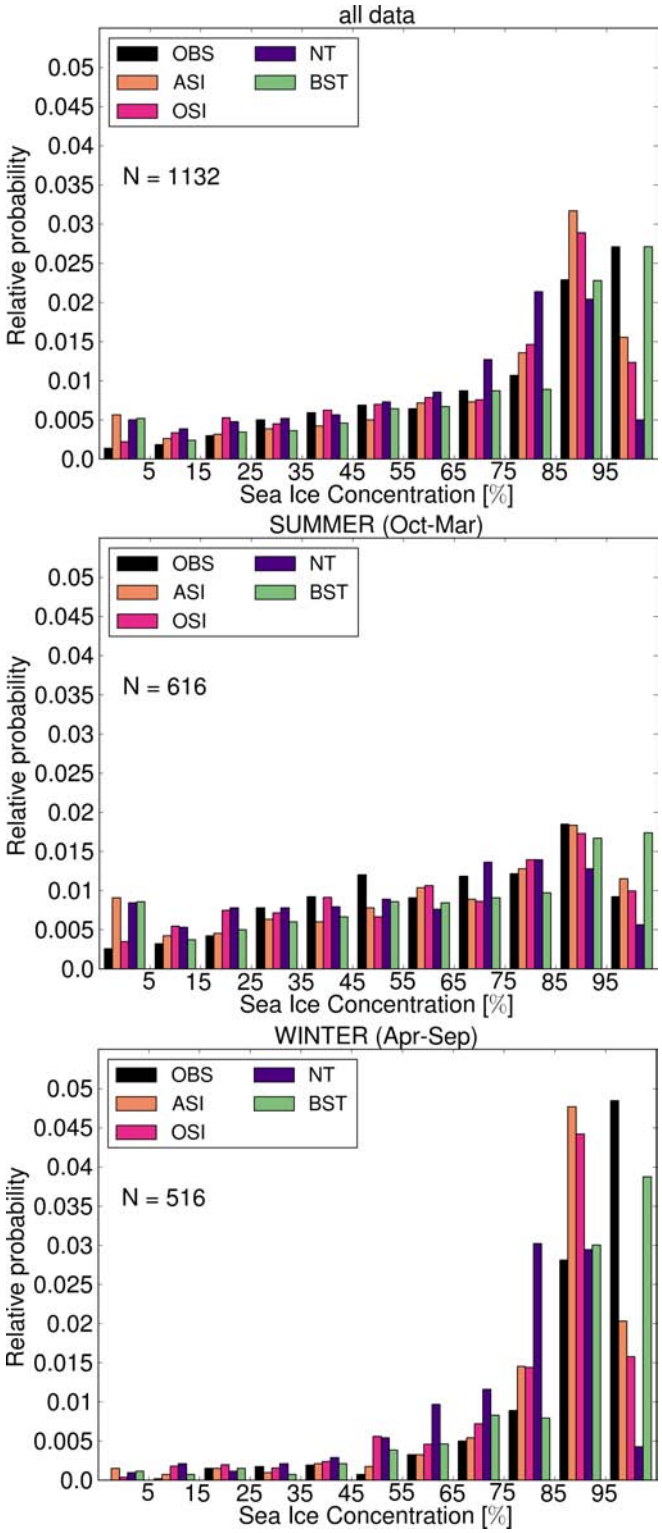

Figure 3.4: Histogram of daily mean along-ship track SIC that are used in the SSM/I-comparison. Top panel: all data, middle panel: data from summer months (October–March), lower panel: data from winter months (April–September). Legends indicate the different algorithms. In each panel, the number of days, N, used in the comparison is shown.

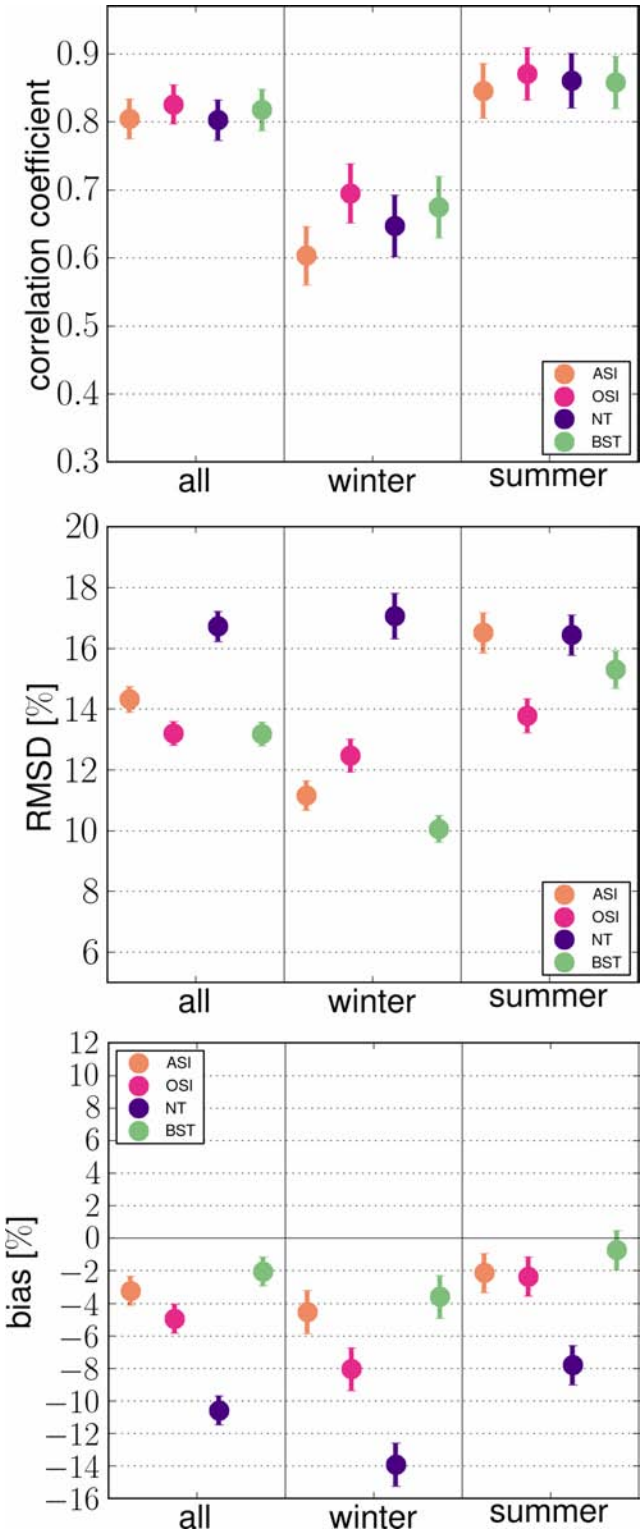

Figure 3.5: Statistics of the comparison of daily mean along-ship track average SIC from PM and OBS for SSM/I. Top panel: correlation coefficient, middle panel: RMSD, lower panel: bias.

Table 3.3: Summary of statistical numbers for SSM/I comparison.

		BST	OSI	ASI	NT
	CC	0.82 ± 0.03	0.83 ± 0.03	0.80 ± 0.03	0.80 ± 0.03
all data	**RMSD**	13.2 ± 0.4	13.2 ± 0.4	14.3 ± 0.4	16.7 ± 0.5
	bias	-2.0 ± 0.9	-5.0 ± 0.9	-3.2 ± 0.9	-10.6 ± 0.9
	CC	0.86 ± 0.04	0.87 ± 0.04	0.85 ± 0.04	0.86 ± 0.04
summer	**RMSD**	15.3 ± 0.6	13.8 ± 0.6	16.5 ± 0.7	16.4 ± 0.7
	bias	-0.7 ± 1.2	-2.4 ± 1.2	-2.1 ± 1.2	-7.8 ± 1.2
	CC	0.67 ± 0.04	0.70 ± 0.04	0.60 ± 0.05	0.65 ± 0.04
winter	**RMSD**	10.1 ± 0.4	12.5 ± 0.5	11.2 ± 0.5	17.1 ± 0.8
	bias	-3.6 ± 1.3	-8.1 ± 1.3	-4.5 ± 1.3	-13.9 ± 1.3

$r = 0.85 \pm 0.04$, NT: $r = 0.86 \pm 0.04$). RMSD and bias show larger differences between the satellite data. Notably, NT shows high values for bias and RMSD: the bias is at least -10 % in all data and almost -14 % in summer months, the RMSD is more than 16 % in all seasons. BST has a very low bias, only increasing to -3.6 % in winter months. RMSD values for OSI range between 12.5 % in winter and 13.8 % in summer. ASI shows a greater RMSD value in summer than winter. The bias is generally slightly lower for ASI than compared to OSI. Both ASI and OSI range between the minimum values for BST and the maximum values for NT. Besides NT, all algorithms show a lower winter than summer bias, but NT's winter bias increases to 17.1 %.

3.3.2 AMSR-E Period

The positions of OBS used for the AMSR-E comparison are overlaid onto a AMSR-E-based ASI sea ice extent map for 7 September 2005 (Fig. 3.6). Due to the limited number of years available for this comparison, OBS SIC were only collected in the Weddell Sea, around the Antarctic Peninsula, Bellingshausen Sea, Amundsen Sea, Ross Sea and the South Indian Ocean.

The distribution of daily mean SIC for OBS, ASI, NT2, and BST shows almost no discrepancies among the compared SIC algorithms in the 5-15 % to 55-65 % bins (Fig. 3.7, upper panel). The NT2 algorithm detects more sea ice in the >95 %-bin than the other SIC algorithms. Furthermore, all algorithms overestimate very sparse ice concentration of OBS. The overestimation of >95 % OBS SIC by PM data is most pronounced in summer, especially for NT2 (Fig. 3.7, middle panel). Note that OBS SIC have a maximum probability in the 85-95 %-bin with a following decrease in the >95 %-bin. This is not matched by the PM data. In contrast to NT2's overestimation of SIC >95 %, NT2 underestimates the number of SIC values falling into the 85-95 %-

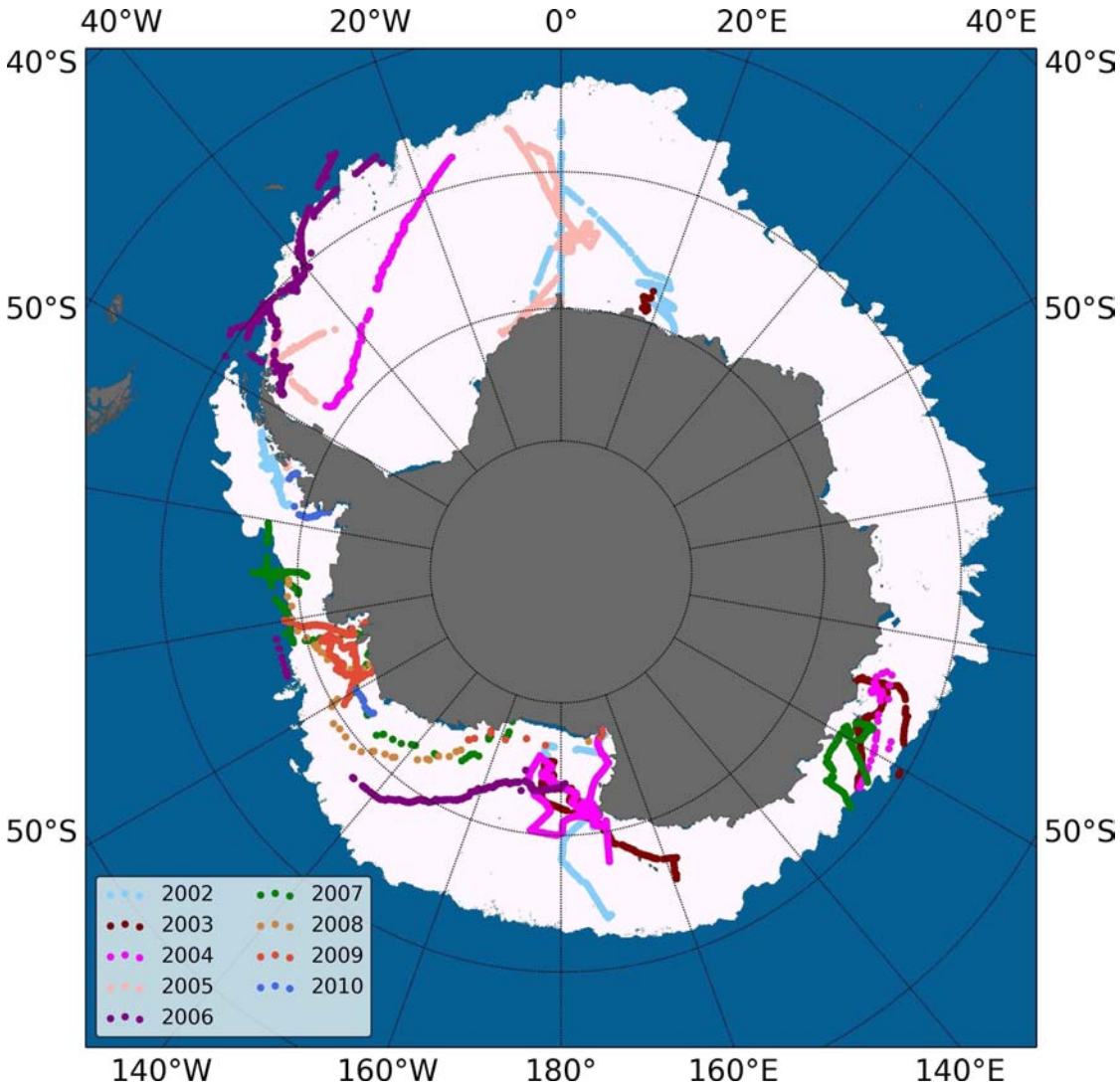

Figure 3.6: ASPeCt ship tracks (OBS) during the AMSR-E comparison period (2002–2009) projected onto an ASI sea ice extent map of September 7, 2005.

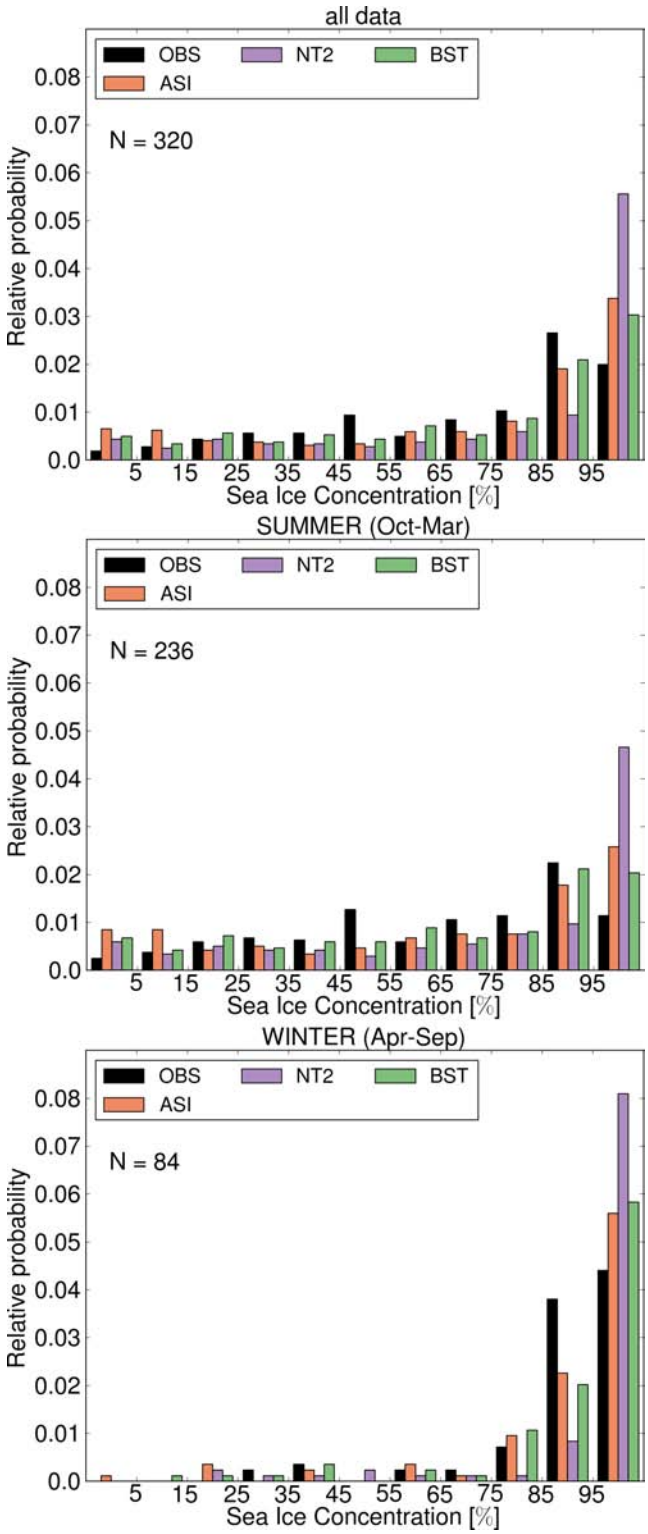

Figure 3.7: Same as Fig. 3.4, but for the AMSR-E comparison.

Table 3.4: Summary of statistical numbers for AMSR-E comparison.

		BST	**ASI**	**NT2**
	CC	0.85 ± 0.06	0.84 ± 0.06	0.84 ± 0.06
all data	**RMSD**	11.6 ± 0.7	13.3 ± 0.7	15.8 ± 0.9
	bias	0.3 ± 1.7	0.0 ± 1.7	8.1 ± 1.7
	CC	0.88 ± 0.06	0.89 ± 0.07	0.87 ± 0.06
summer	**RMSD**	12.7 ± 0.8	14.5 ± 0.9	17.7 ± 1.2
	bias	0.3 ± 2.0	0.1 ± 2.0	9.4 ± 2.0
	CC	0.60 ± 0.11	0.51 ± 0.11	0.55 ± 0.11
winter	**RMSD**	7.8 ± 0.8	9.3 ± 1.0	8.7 ± 0.9
	bias	0.3 ± 3.3	-0.1 ± 3.3	4.7 ± 3.3

bin. ASI and BST also show this discrepancy, but not as pronounced as NT2. In summer months, there is a peak of OBS SIC in the 45-55 %-bin that is not reproduced by PM SIC. During winter, NT2 again overestimates very high ice concentration and underestimates the number of observations in the bin below, the 85-95 %-bin (Fig. 3.7, lower panel). However, due to the small number of data pairs during winter months, these differences are not as significant as in summer.

Fig. 3.8 and Table 3.4 summarize the statistical comparison between the individual PM SIC and OBS SIC for the AMSR-E period. In contrast to the SSM/I comparison, correlation coefficients are slightly increased (BST: $r = 0.85 \pm 0.06$, ASI: $r = 0.84 \pm 0.06$, NT: $r = 0.84 \pm 0.06$), but with a concurrent increase of the uncertainty in r, which is due to the lower number of data pairs for the AMSR-E period. Correlation coefficients in summer increase even further to almost 0.9 for all PM SIC, while they decrease in winter to about 0.5 for ASI and 0.6 for BST. As for SSM/I, we recognize the same tendency for RMSD: summer values are greater than winter values. While there is only very little bias for BST and ASI in both summer and winter, NT2 has a pronounced summer bias, almost twice as large as the 5 % bias in winter.

3.3.3 Sensor Comparison

In a third comparison done is this study, we assess the performance of two PM SIC retrieval algorithms that are applicable to SSM/I and AMSR-E data. We choose BST and ASI for this comparison, as they tend to provide the best results in the previous comparisons. The positions of OBS used for this comparison are identical to those shown in Fig. 3.6.

The distribution of daily mean SIC for OBS, ASI-AMSR-E, ASI-SSM/I, BST-AMSR-E, and BST-SSM/I show the largest differences for both seasons in the

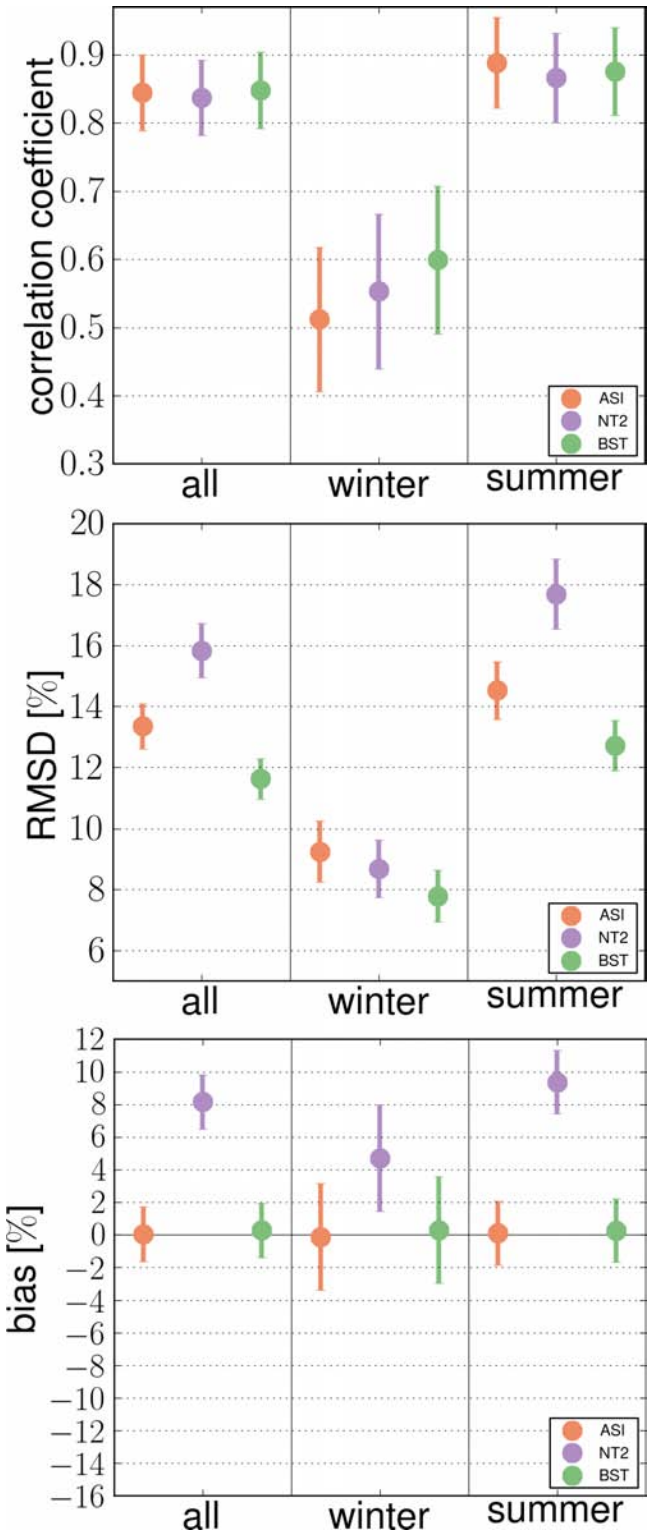

Figure 3.8: Same as Fig. 3.5, but for the AMSR-E comparison.

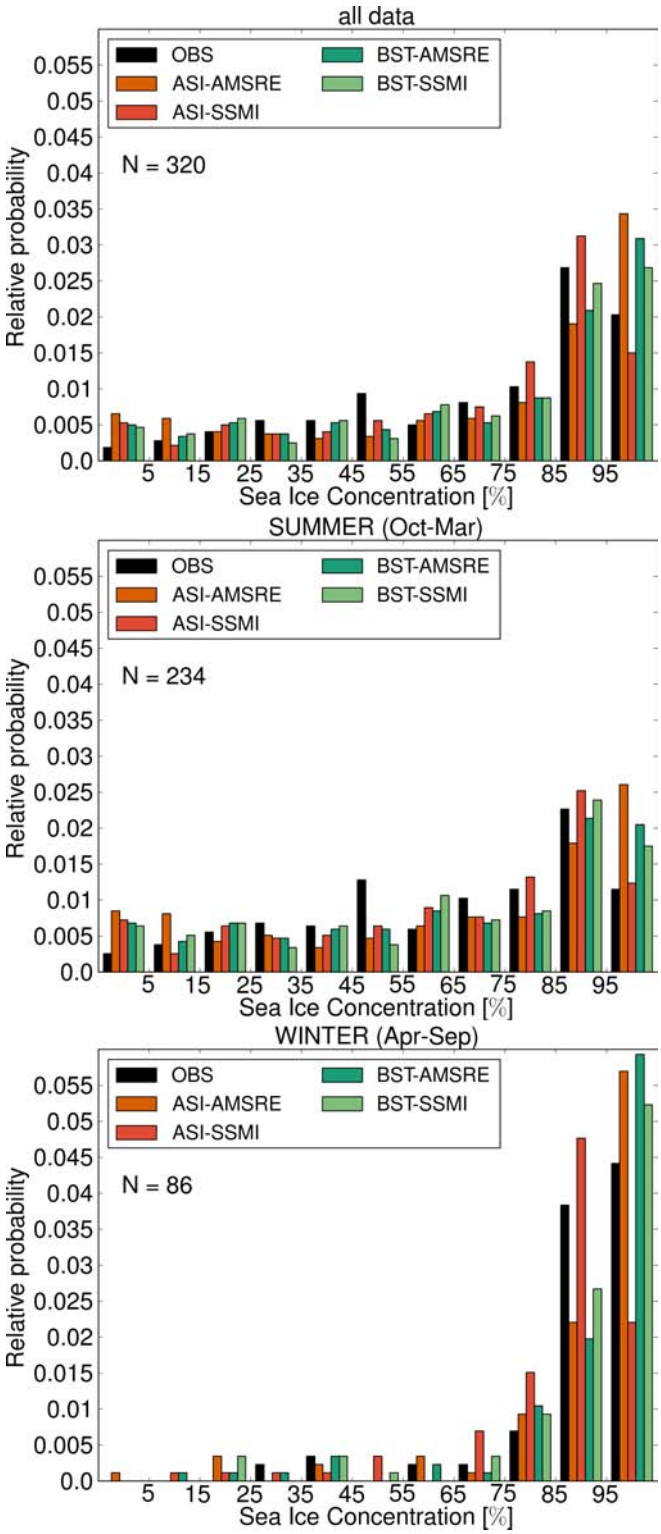

Figure 3.9: Same as Fig. 3.4, but for the sensor-comparison.

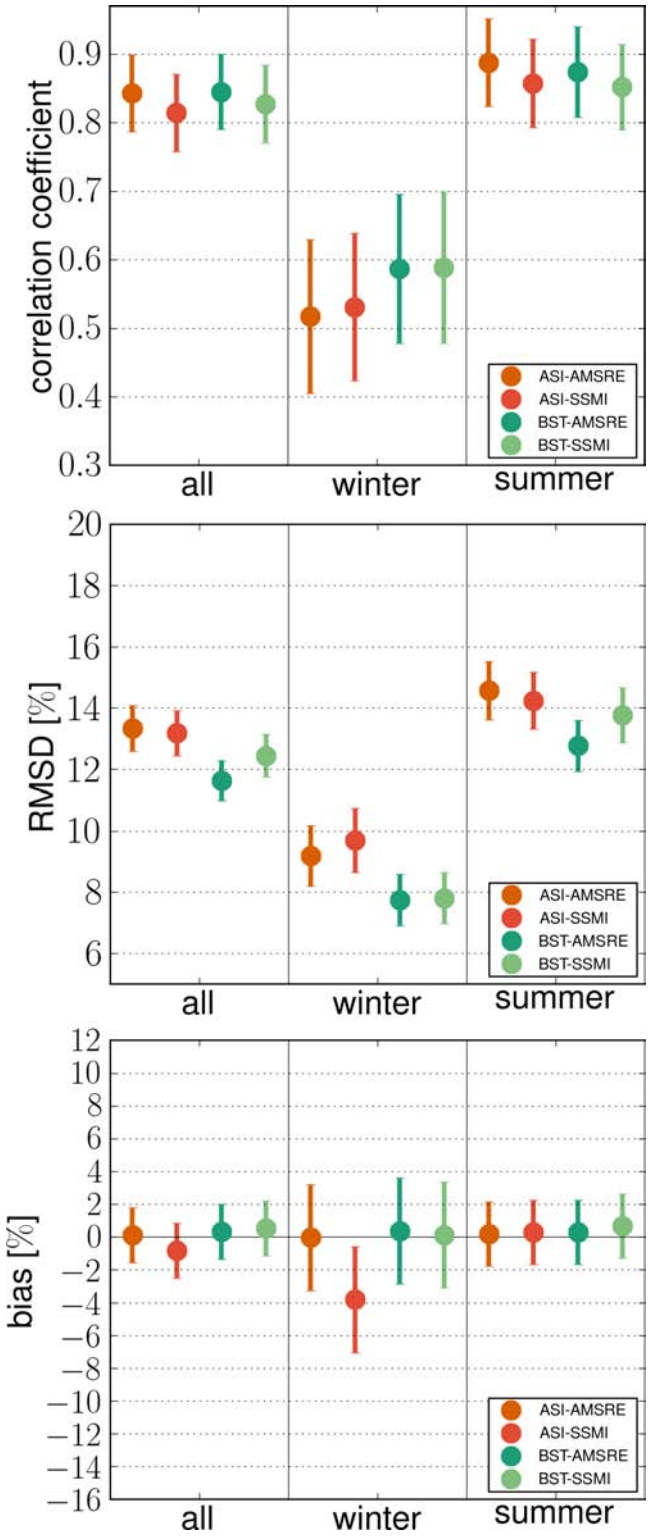

Figure 3.10: Same as Fig. 3.5, but for the sensor-comparison.

Table 3.5: Summary of statistical numbers for inter-sensor comparison for ASI and BST SIC.

		BST/AMSR-E	**BST/SSMI**	**ASI/AMSR-E**	**ASI/SSMI**
	CC	0.84 ± 0.06	0.83 ± 0.05	0.84 ± 0.06	0.81 ± 0.06
all data	**RMSD**	11.6 ± 0.7	12.4 ± 0.7	13.3 ± 0.7	13.2 ± 0.7
	bias	0.3 ± 1.7	0.5 ± 1.7	0.1 ± 1.7	-0.8 ± 1.7
	CC	0.87 ± 0.07	0.85 ± 0.06	0.89 ± 0.06	0.86 ± 0.06
summer	**RMSD**	12.8 ± 0.8	13.8 ± 0.9	14.6 ± 1.0	14.2 ± 0.9
	bias	0.3 ± 2.0	0.7 ± 2.0	0.2 ± 2.0	0.3 ± 2.0
	CC	0.59 ± 0.11	0.59 ± 0.11	0.52 ± 0.11	0.53 ± 0.11
winter	**RMSD**	7.7 ± 0.8	7.8 ± 0.8	9.2 ± 1.0	9.7 ± 1.0
	bias	0.4 ± 3.2	0.1 ± 3.2	0.0 ± 3.2	-3.8 ± 3.2

high SIC regime (SIC >85 %) (Fig. 3.9, upper panel). These differences are more pronounced in winter months. However, winter contains a much lower number (N=86) of data pairs than summer (N=320). In addition, PM SIC tend to overestimate very low SIC (<5 %). This is more pronounced in summer, which depicts the season with a higher fraction of open water within the sea ice cover. Contrary to this, sea ice is often wet in this season and thus difficult to be detected in PM data. It seems that navigating through very open ice areas during summer (and thus causing a low bias) is outweighed by the effect of wet ice being invisible for PM but visible for OBS.

Fig. 3.10 and Table 3.5 summarize the statistical comparison between the individual PM SIC and OBS SIC for the sensor comparison, covering the years 2002–2010. There is no significant difference in accuracy between either different algorithms applied to the same sensor data or the same algorithm applied to different sensor data. A few tendencies, however, are recognizable: considering all statistical numbers, BST shows more congruency to OBS with lower RMSD values, a better correlation in winter, and a near-zero bias. SIC based on AMSR-E data tend to agree better with OBS SIC than SIC based on SSM/I data. Similar to the other two comparisons, RMSD values and correlations are reduced during winter.

3.4 Discussion

In the previous section we have presented the results of our comparison between OBS SIC and co-located satellite PM SIC based on several algorithms. The results turned out to be quite different for the different retrieval algorithms used. But, are the obtained results sufficient to give a recommendation about which SIC retrieval algorithm is best to use based on a comparison with OBS SIC? This is going to be discussed in the following section.

Retrieval algorithms for SIC differ in how ice concentration values are derived from PM-measured brightness temperatures. They use different combinations of different channels that have distinct characteristics, e.g., the frequencies differ in their sensitivity to atmospheric water vapor and liquid water content, both of which influence the radiation received at the radiometer. Additionally, the algorithms need to use tie-points that represent typical radiometric signatures of ice and open water. These tie points are usually derived from satellite measurements and contain the influence of the mean atmospheric state. In atmospheric conditions that are different from this mean atmospheric state, the derived tie-points will lead to biased SIC values. While the open water tie-point is generally influenced by atmospheric variability, the ice tie-point is influenced by sea ice emissivity variations. Therefore, concentrations retrieved at low ice concentrations are most sensitive to the choice of the open water tie-point and high ice concentrations are prone to surface processes (Andersen et al., 2006). Generally, one seeks for a high signal-to-noise ratio when choosing the tie-points aiming for a high sensitivity in retrieving PM SIC. Open water tie-points are usually set very close to a minimum brightness temperature or maximum brightness temperature polarization difference or ratio, which corresponds to a clear-sky, dry atmosphere and a smooth water surface. The use of weather filters reduces the influence of atmospheric water and wind on the emissivity of the open water surface. However, this can lead to a cut-off of low SIC values. Only the reprocessed OSI data provide SIC without a cut-off by using dynamic tie-points that, for instance, minimize the effect of atmospheric emission (Eastwood et al., 2011).

Improvements of AMSR-E data over SSM/I data that are relevant for this comparison include higher spatial resolution at all scanned frequencies and a wider swath width. The wider swath width leads to more brightness temperature measurements that are used to calculate a daily-mean SIC value from the specific algorithm and, thus, can increase the significance of a calculated daily-mean SIC value during static ice conditions. In the MIZ, this can still lead to a smearing of the ice edge, especially under very dynamic ice conditions, e.g., during the passing of a cyclone. When retrieving geophysical parameters like the sea ice concentration, the higher spatial resolution of AMSR-E reduces uncertainties. Such uncertainties can partly be due to smaller spatial variability of differently emitting surfaces, e.g., different ice types, snow cover or water surfaces. These different surface types particularly influence the use of mixing algorithms (Comiso and Nishio, 2008), especially in the MIZ, where the higher spatial resolution of the AMSR-E sensor allows for a more precise detection of the ice edge (Worby and Comiso, 2004). In our case, with a finer spatial resolution one should get a better representation of leads and open water areas in high ice concentration regimes, i.e., of SIC in the range >85 %. The same applies to using 85 GHz (SSM/I) or 89 GHz (AMSR-E) data compared to using the standard frequencies 19 GHz and 37 GHz as was demonstrated for SSM/I by Kaleschke et al. (2001) and Kern (2004).

Sea ice continuously changes its emissivity from its initial growth stage to thick first-year ice (Perovich et al., 1998; Grenfell et al., 1998; Hwang et al., 2007). In particular

thin sea ice with thicknesses below about 20 cm often has lower microwave emissivities than thicker sea ice or snow covered sea ice. Therefore, PM SIC retrieval algorithms can underestimate SIC in areas of thin sea ice by an unknown amount (Cavalieri, 1994; Comiso et al., 2003; Spreen et al., 2008).

We have shown SIC values in the histograms (Fig. 3.4, Fig. 3.7 and Fig. 3.9) sorted in bins for 0 %-5 %, 5 %-15 %, 15 %-25 % $\cdots$ 85 %-95 %, and 95 %-100 % sea ice concentration according to the increments used in the ASPeCt protocol when observing SIC. Due to the daily averaging, we have values that differ from this quantization into 10 % increments. In order to keep this quantization visible and to also consider the accuracy of the ASPeCt observations, we used as division of PM SIC the same increments that were used in the ASPeCt protocol. However, the differences between PM SIC and OBS SIC shown in the histograms (Fig. 3.4, Fig. 3.7, and Fig. 3.9) are highest in neighboring bins: 85-95 % and >95 %. We cannot exclude that using a different binning like 0 %-10 %, 10 %-20 % $\cdots$ 90 %-100 % might change the results of the histograms. However we are confident that the main results of our study, which are summarized in Fig. 3.5, Fig. 3.8, and Fig. 3.10, will not change due to a different binning.

The number of data pairs differs for the different seasons. Especially in the AMSR-E comparison, only 25 % of the data fall into winter months. However, due to the number of data points, with at least 3 observations required for a daily-average value, the results for the winter season can still be regarded as significant.

Ship-based observations are often biased towards thin ice regions, because ships tend to avoid thick and ridged ice areas and rather follow leads and openings (Ozsoy-Cicek et al., 2011). Ridged ice areas can correspond to regions of convergent ice motion and, thus, high ice concentrations while regions with many leads and openings correspond to divergent ice motion and can have lower ice concentrations. Therefore, we cannot exclude that OBS SIC are slightly biased towards low ice concentrations, particularly during summer when leads and openings do not freeze over. At the same time, however, PM SIC might also be biased low in areas with leads and openings due to the higher fraction of thin ice; this effect would be more pronounced during winter though.

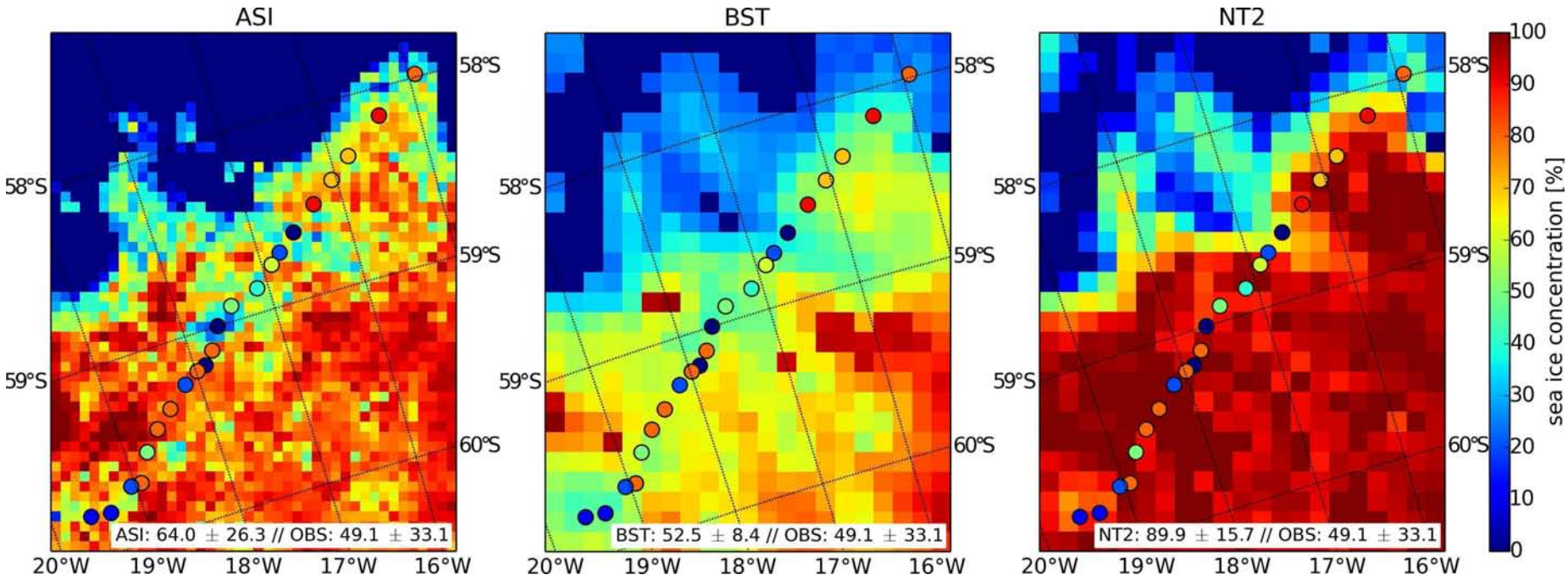

Figure 3.11: Example of a daily track crossing the sea ice edge in the Weddell Sea on November 14, 2004. Sea ice concentrations based on AMSR-E are shown for (left to right): ASI (grid resolution: 6.25 km), BST (grid resolution: 12.5 km), and NT2 (grid resolution: 12.5 km). The daily mean and the daily standard deviation for OBS, ASI, BST and NT2 are 49.1 % ± 33.1 %, 64.0 % ± 26.3 %, 52.5 % ± 8.4 %, and 89.9 % ± 15.7 %, respectively.

In this study, we do not distinguish between different regions and potentially different sea ice regimes. The Bellingshausen Sea, for instance, is known for more compact, thicker, and less mobile first year sea ice (Worby et al., 2011). Distinguishing between different regions could help to understand where different algorithms have their strengths or limitations. However, this is not intended in this study, which rather looks at the performance of different algorithms compared to a long-term basin-scale ground-truth data set. Due to the number of observations, we regard our conclusion as robust and being generally true for the Antarctic sea ice as a whole. If we had looked at different ice types or had tried to distinguish between different regions, the number of data pairs would have dropped substantially and the results would have been less robust.

In all 3 comparisons shown in this study, BST SIC has the closest correspondence to OBS SIC, both for SSM/I and AMSR-E data. However, the higher resolution of the ASI algorithm can provide more information than algorithms using the lower frequency channels for their retrievals. One aspect is the higher spatial variability that is more accurately reproduced by ASI (see Fig. 3.11). This can be an advantage for navigational purposes and for mesoscale process studies (Kaleschke et al., 2001).

3.5 Conclusion

We compare passive microwave (PM) derived sea ice concentration (SIC) with those from ship-based observations (OBS) and we focus on different retrieval algorithms that are based on SSM/I-SSMIS and AMSR-E measurements. OBS SIC are collected according to the Antarctic Sea Ice Processes and Climate (ASPeCt) protocol. We assess the quality of PM SIC by calculating correlation coefficients, root-mean-square-deviations (RMSD) and biases with respect to OBS SIC. In contrast to previous studies, we apply a different method to compare the co-located OBS SIC with PM SIC to account for the different temporal and spatial scales between locally observed SIC on a scale on the order of 1 km and those derived with PM sensors on a scale on the order of 10 km. We use daily along-ship track average SIC.

According to our analysis, we can rank the investigated retrieval algorithms: in the SSM/I comparison, Bootstrap (BST) SIC reveal a high correlation, the smallest RMSD, and a very low negative bias compared to OBS SIC and thus again performs best out. EUMETSAT's OSI-SAF (OSI) SIC show a similar RMSD, but a larger absolute bias than BST and thus OSI ranks as second best algorithm. ARTIST Sea Ice (ASI) SIC show a significantly larger RMSD and also a very low bias. NASA Team (NT) SIC, while providing a similarly high correlation, clearly perform worst out of our choice with highest RMSD values and a significantly larger bias of -10 % or more. In the AMSR-E comparison, BST SIC reveal the smallest RMSD, and a near zero bias compared to OBS SIC and thus perform best out of our choice of algorithms.

ASI SIC show a significantly larger RMSD and also a near zero bias. Like NT in the SSM/I-SSMIS comparison, enhanced NASA Team (NT2) SIC provide a similarly high correlation, but perform worst out of our choice of algorithms with RMSD values, except for winter, above those for ASI SIC and a significantly larger bias of roughly 8 %.

Due to the length of the different PM SIC time series, we have an overlap of OBS SIC and PM SIC that leads to periods of investigation spanning 1991–2009 for SSM/I data, a total of 21625 data pairs, and spanning 2002–2010 for AMSR-E data, a total of 3871 data pairs. To our knowledge, there has not been a comparison with this number of ship-based observations of sea ice concentrations with PM-derived sea ice concentrations and we therefore regard our results as robust. This work is an important contribution to sea ice concentration evaluation in the in-situ data sparse region of the Southern Ocean.

Acknowledgment

We acknowledge funding by the Federal Ministry of Economics and Technology (BMWi) through the IRO-2 project and the National German Science Foundation (CliSAP). We thank: the National Snow and Ice Data Center in Boulder, Colorado and the JAXA EORC (Earth Observation Research Center), Tokyo, for providing SSM/I, SSMIS and AMSR-E data, ice observers aboard the Antarctic research voyages that contributed data for the ASPeCt data used in this study, as well as A. H. Tekeli and S. F. Ackley (both at Univ. San Antonio), as well as B. Ozsoy-Cicek (now at Technical University Istanbul), and S. Willmes (Univ. Trier) for providing additional ship-based observation to extend the ASPeCt data.

Chapter 4

Investigating high-resolution AMSR2 sea ice concentrations during the February 2013 fracture event in the Beaufort Sea[1]

Leads with a length on the order of 1000 km occurred in the Beaufort Sea in February 2013. These leads can be observed in Moderate Resolution Imaging Spectroradiometer (MODIS) images under predominantly clear sky conditions. Sea ice concentrations (SIC) derived from the Advanced Microwave Scanning Radiometer 2 (AMSR2) using the Bootstrap (BST) algorithm fail to show the lead occurrences, as is visible in the MODIS images. In contrast, SIC derived from AMSR2 using the Arctic Radiation and Turbulence Interaction Study (ARTIST) sea ice algorithm (ASI) reveal the lead structure, due to the higher spatial resolution possible when using 89 GHz channel data. The ASI SIC are calculated from brightness temperatures interpolated on three different grids with resolutions of 3.125 km (ASI-3k), 6.25 km (ASI-6k) and 12.5 km (ASI-12k) to investigate the effect of the spatial resolution. Single-swath data is used to study the effect of temporal sampling in comparison to daily averages. For a region of interest in the Beaufort Sea, BST and ASI-3k show area-averaged SIC of 97% ± 0.7% and 93% ± 7.0%, respectively. For ASI-6k, the area-averaged SIC are similar to ASI-3k, while ASI-12k data show more agreement with BST. Visual comparison with MODIS True Color imagery exhibits good agreement with ASI-3k. In particular, ASI-3k are able to reproduce lead structure and size in the sea ice cover, which are not or are less visible in the other SIC data. The results will be valuable for selecting a SIC data product for studies of the interaction between ocean, ice, and atmosphere in the polar regions.

[1] This chapter is published as: Beitsch, A., Kaleschke, L., and Kern, S., 2014: Investigating High-Resolution AMSR2 Sea Ice Concentrations during the February 2013 Fracture Event in the Beaufort Sea. *Remote Sens.*, **6(5)**, 3841–3856, doi:10.3390/rs6053841.

4.1 Introduction

The polar regions are essential components of the global climate system. The Arctic and Antarctic sea ice cover have considerable effects on ocean-atmosphere heat transfer (Maykut, 1982) and on the formation of deep water masses (Stossel, 2010). The albedo of the polar ice cover is crucial for the global heat balance of the Earth's climate (Curry et al., 1995). During the last three decades, the use of remote sensing products to understand key processes in the global climate system has substantially increased (Stroeve et al., 2012). For instance, sea ice concentrations (SIC) are used for investigations in climate research and for data assimilation in Numerical Weather Prediction (Uotila et al., 2011; Donlon et al., 2012). Additionally, changes in sea ice extent have large impacts on the Arctic climate system, e.g., the connection of and interaction between sea ice, air temperature and permafrost on continents and ocean shelves is a matter of current research (Parmentier et al., 2013). Since the 1970s, numerous satellite missions have been launched and a considerable number of algorithms has been developed to derive SIC from passive-microwave (PM) data. These algorithms use approximations of the radiative transfer equation for electromagnetic waves in the microwave regime, empirical approaches that consider relationships between brightness temperatures (TB) and SIC, or a combination of both (Steffen et al., 1992).

In the course of the "Arctic Radiation and Turbulence Interaction Study" (ARTIST), the ARTIST sea ice algorithm (ASI) was developed using the 85 GHz channels of the Special Sensor Microwave/Imager (SSM/I) to provide high spatial resolution SIC (Kaleschke et al., 2001). The algorithm is based on the Svendsen sea ice algorithm for near 90 GHz frequencies (Svendsen et al., 1987). With the start of NASA's Advanced Microwave Scanning Radiometer (AMSR-E) on-board the Aqua satellite, the spatial resolution at 89 GHz became nearly three times higher than for SSM/I at 85 GHz (Spreen et al., 2008). Consequently, the ASI algorithm was adapted for the use of 89 GHz measurements (Spreen et al., 2008). Despite the enhanced sensitivity to the atmospheric influence at these frequencies compared to lower microwave frequencies, this algorithm provides almost weather-independent SIC (Kaleschke et al., 2001; Spreen et al., 2008). A detailed description and derivation of the algorithm and the weather filtering can be found in Kaleschke et al. (2001) and Spreen et al. (2008).

AMSR-E-based ASI SIC provide a horizontal resolution that is up to four times higher than another algorithm that is widely used to retrieve SIC, the Bootstrap algorithm (Comiso et al., 1997, 2003; Comiso, 2004). The Bootstrap algorithm (BST) mainly utilizes the TB measured at the frequencies of 18.7 and 36.5 GHz and, therefore, depends on a larger footprint size of the measured TB data, which reduces the spatial resolution of the retrieved SIC. With the launch of the Japan Aerospace Exploration Agency's (JAXA) Advanced Microwave Scanning Radiometer 2 (AMSR2), the improved successor of AMSR-E, the spatial resolution of ASI SIC has even further improved, due to both scans available from the feedhorns measuring at 89 GHz.

This work studies the effect of spatial resolution and temporal sampling in ASI SIC on the ability to resolve local structures, like leads within the sea ice cover. Leads are large, elongated or linear-like fractures in a formerly solid sea ice cover that develop due to divergence and shear forces within the sea ice cover (Marcq and Weiss, 2012). Through uncovering the relatively warmer ocean surface to the cold winter atmosphere, leads are of significant importance for the local near-surface heat balance of the winter Arctic atmosphere (Marcq and Weiss, 2012). From a modeling study of atmosphere-ocean heat exchange due to lead openings, it is inferred that a change in SIC of 1% can cause a near-surface temperature increase of up to 3.5 K (Lüpkes et al., 2008).

The paper proceeds in the following way: Section 2 briefly reports new features of the AMSR2 sensors. Section 3 introduces the new 3.125 km ASI SIC and lower resolution derivatives of ASI and JAXA's AMSR2-based SIC that are used in this study for comparison. In Section 4, we present the comparison, and we end with a discussion in Section 5.

4.2 AMSR2

The AMSR2 on-board the Global Change Observation Mission 1st-Water (GCOM-W1) satellite is the successor instrument of AMSR-E (Japan Aerospace Exploration Agency, 2013). It was launched in May 2012 and placed into the Afternoon Constellation (A-Train Japan Aerospace Exploration Agency, 2013). The A-Train consists of a number of Earth observing satellites that orbit the Earth in a sun-synchronous orbit in close proximity at about a 700 km height above the Earth's surface. The constellation crosses the equator at around 1:30 P.M. mean solar time (L'Ecuyer, 2011). AMSR2 Level-1 TB data are available for the period starting in July 2012 via JAXA's GCOM-W1 Data Providing Service.

The AMSR2 instrument is a conically-scanning PM radiometer system that measures in seven frequency bands ranging between 6.925 GHz and 89.0 GHz at both horizontal and vertical polarization. The antenna's different feedhorns scan at an incidence angle of 55°and provide a 1450 km swath width at the Earth's surface (Japan Aerospace Exploration Agency, 2013). Compared to AMSR-E, AMSR2 provides improved characteristics (Japan Aerospace Exploration Agency, 2013):

- The size of its main reflector has increased from 1.6 m (for AMSR-E) to 2.0 m (for AMSR2), which leads to smaller footprints and, thus, higher spatial resolutions for the different frequencies;
- Its calibration system has improved, leading to higher temperature stability when calculating TB from sensor data, due to a more homogeneously calibrated warm load—the High Temperature Noise Source (HTS); and

- A redundant momentum wheel has been added to the system to increase reliability.

4.3 AMSR2-Based Sea Ice Concentrations

4.3.1 Processing of Sea Ice Concentrations using ASI

For the new ASI AMSR2 SIC, we process single swaths of Level-1R TB data that are based on Level-1B TB data. In the Level-1B data, the center of a footprint at each frequency that corresponds to the same scan number or pixel can differ in its location on the Earth's surface by several kilometers (Maeda and Taniguchi, 2013). For the Level-1R data, the different channel's footprints have been resampled to match the same location and the resolution of lower frequency channels. For that, Level-1B TB data are recalculated using the Backus–Gilbert method (see Japan Aerospace Exploration Agency, 2013; Stogryn, 1978; Hunewinkel et al., 1998)). This method improves the retrieval accuracy of higher level products, and we expect the weather filters to give more consistent results when the 18.7 GHz, the 23.8 GHz and the 36.5 GHz channels are georeferenced and Backus–Gilbert-interpolated to the same footprint location. To interpolate the satellite measurements onto a regular grid, we resample the swath-based TB using a nearest neighbor approach. From the gridded swath-based TB data, we calculate daily-mean TB maps. Based on these daily-mean TB maps, SIC are calculated, and the weather filters are applied. For single-swath SIC, the single-swath TBs are processed accordingly without calculating daily-mean TB maps. Then, monthly maximum-extent masks from the National Snow And Ice Data Center (NSIDC User Service, 2013)) are used to remove false SIC that may still exist over open water areas. These monthly maximum-extent masks are provided on the original 25 km grid used for the Nimbus-7 Scanning Multichannel Microwave Radiometer (SMMR) and SSM/I SIC. We interpolate these masks to the 12.5 km, 6.25 km and 3.125 km grids that are used for our data and manually correct for coarse coastlines stemming from the original 25 km resolution. Due to the long-term decline in sea ice extent and SIC (Cavalieri and Parkinson, 2012), we consider the potential very unlikely that the used climatology cuts off sea ice outside of the masked regime. Note that the tie-points used in the AMSR2 SIC processing have not been adapted to the new sensor, and the former AMSR-E derived tie-points (Spreen et al., 2008) are still used. This is a valid approach in this study, because of the similarities of the AMSR2 instrument to the AMSR-E instrument. For long-term time series analysis using data from both sensors, an adjustment would be needed. We provide ASI-AMSR2 3.125 km SIC for both hemispheres on a daily basis through the Integrated Climate Data Center (ICDC) of the University of Hamburg (see `http://icdc.zmaw.de`).

For this study, we also calculate ASI SIC at 6.25 km (ASI-6k) and 12.5 km (ASI-12k) resolution. ASI-6k is intended to simulate AMSR-E-based SIC by only considering

Table 4.1: Advanced Microwave Scanning Radiometer 2 (AMSR2) footprint sizes at the different frequencies according to the Global Change Observation Mission 1st-Water (GCOM-W1) "SHIZUKU" Data Users Handbook (Japan Aerospace Exploration Agency, 2013).

Center Frequency (GHz)	6.925	7.3	10.65	18.7	23.8	36.5	89.0 (A&B)
Field of view (km^2)	35×62	35×62	24×42	14×22	15×26	7×12	3×5

89 GHz B-scan measurements to derive SIC. The A-scan of the 89 GHz feedhorn of AMSR-E measurements started producing corrupted measurements from the period starting in November 2004. For ASI-12k, we simulate the larger footprint size of the 18 GHz channel (see Table 4.1) by resampling multiple 89 GHz scans within a search radius that matches the 18 GHz footprint size. The scans found within the search radius are averaged by Gaussian weighting considering the distance to the center of the search field. Then, the resampled TB data are input to the SIC retrieval. Thereby, we investigate the effect of the larger footprint on the SIC retrieval. The 18 GHz TB data, together with 36 GHz TB data, provide the main ice information in the BST processing (see Section 4.3.2).

4.3.2 AMSR2 BST Sea Ice Concentrations

The ASI-based SIC are compared with SIC that are derived using the Bootstrap algorithm provided as Level-3 data by JAXA (Comiso and Cho, 2013). Daily-mean SIC are provided separately for ascending and descending swaths at 10 km resolution via JAXA's GCOM-W1 Data Providing Service. We average both daily products to one daily-mean SIC map to compare with the ASI-based daily-mean SIC maps.

4.4 Comparison of the High-Resolution ASI SIC with MODIS Data, BST SIC and ASI SIC at Coarser Resolutions

To evaluate the performance of the new high-resolution SIC, we compare ASI-3k with ASI-6k, ASI-12k and AMSR2-based BST SIC for a period in February 2013 in the Beaufort Sea. Additionally, these SIC are compared with 250-m resolution MODIS True Color (MODIS VIS) and 4 km resolution MODIS ice surface temperatures (MODIS IST Hall et al., 2006, Figures 4.1–4.3).

All maps in Figures 4.1–4.3 display a part of the southern Beaufort Sea for 25, 26 and 27 February, respectively. From 21 February onwards, the sea ice cover started moving towards the Bering Strait, with several leads appearing every day in the western area shown in the maps. During the following days, progressively more leads

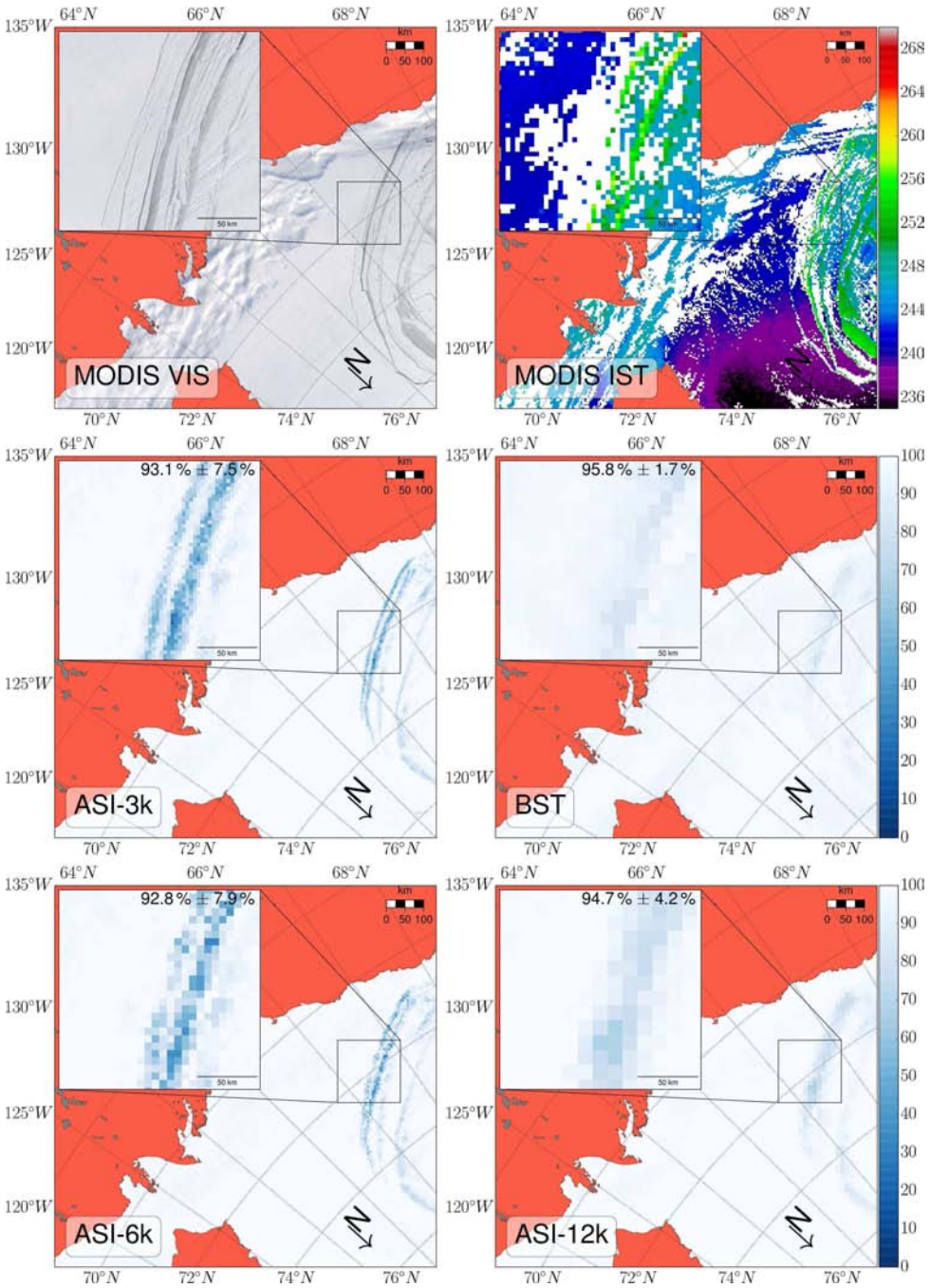

Figure 4.1: Comparison of 250-m MODIS True Color (MODIS VIS), 4 km MODIS ice surface temperature (MODIS IST), ASI-3k, ASI-6k, ASI-12k and Bootstrap (BST) sea ice concentrations (SIC) for 25 February 2013. All maps display a part of the southern Beaufort Sea, with the Canadian and Alaskan coasts in the upper and left parts of the maps. The northern tip of Banks Island can be seen at the lower margin of the maps. An image inset with a zoom of a specified region (170 km × 170 km) is placed on the continental areas for a closer examination of the individual data sets. An arrow depicts the direction to the North Pole. The white areas in MODIS IST depict missing data.

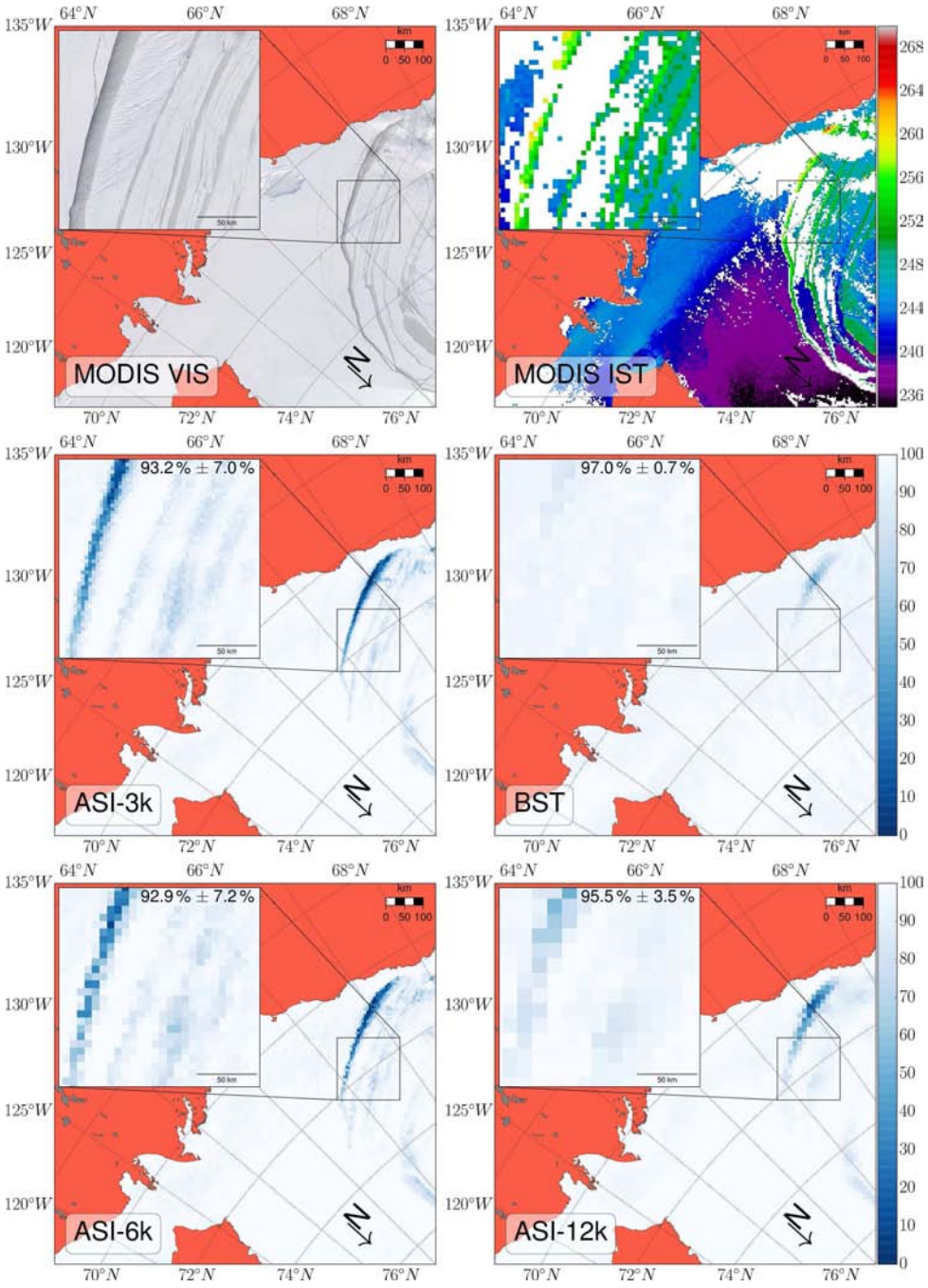

Figure 4.2: Same as Figure 4.1, but for 26 Februar 2013.

appeared towards the Canadian Arctic Archipelago (CAA), until, on 27 February, recently formed and partly refrozen leads pervaded the sea ice cover of the whole Western Arctic. Only the land-fast ice close to the Canadian coast and the sea ice in the CAA was intact. In this study, we focus on a ∼1000 km-long lead (henceforth called Feb-26-lead) that developed between 25 February and 26 February and is located between 76° N and 135° W in the lower right part of the maps and close to the coast of Alaska, near Prudhoe Bay (approximately at 70° N and 148° W, Figure 4.2).

In MODIS VIS (Figure 4.2), the Feb-26-lead appears as a dark opening in the otherwise bright sea ice cover. Distinct temperature differences exist between the partly open and partly refrozen areas of the Feb-26-lead and the surrounding solid ice cover, visible in the MODIS IST map. These temperature differences are 20 K maximum for the inset area. In this inset, parts of the temperature data close to the location of the Feb-26-lead have been filtered due to a cloud mask or because the surface is detected as open water. However, the structure and the position of the Feb-26-lead are recognizable. Most of the full MODIS tile is cloud free and provides clear-sky conditions enabling comparison with the different AMSR2 SIC data.

Other leads, which had formed on 25 February (see Figure 4.1), are located west of the Feb-26-lead and show a higher albedo, indicating a refrozen ice surface. On 26 February, the albedo in the Feb-26-lead increases from left to right (MODIS VIS, Figure 4.2); this suggests the presence of open water at the windward side and a new ice cover becoming progressively thicker, building up towards the leeward side. Additionally, open water patches can be identified at some locations in this new ice cover. The moisture and heat input through the openings into the atmosphere generates clouds. These clouds spread westward by the easterly winds and form cloud streets in the lee of the openings. Most of these clouds are detected by the cloud mask used in the MODIS IST data set (see the inset in MODIS IST, Figure 4.2). The MODIS IST data from within the Feb-26-lead suggest a mixture of open water and thin ice, but the grid resolution of 4 km is too large to adequately discriminate both surface types. The Feb-26-lead shows a higher albedo on 27 February (MODIS IST in Figure 4.3), indicating thickening of the new ice cover. Additionally, MODIS IST exhibits lower temperatures for the lead area (MODIS IST, Figure 4.3). For the solid sea ice cover, ice surface temperatures decrease with increasing latitude, mirroring the low near-surface air temperatures during the period of investigation (not shown).

The lower four panels of Figures 4.1 and 4.2 exhibit quite substantial differences among the SIC data. For the three ASI maps—ASI-12k, ASI-6k and ASI-3k—these differences result from the different grid resolutions and, therefore, from the sampling routines applied (see Section 4.3.1). Most details of the Feb-26-lead are visible in the ASI-3k map. In contrast, BST shows only reduced SIC for the area of the Feb-26-lead. Only close to the Alaskan coast, where the lead has its maximum width, BST SIC are as low as ∼50% SIC. The difference between BST and ASI-3k in area-averaged SIC for the zoomed area in the insets is ∼4 % on 26 February (numbers are shown in the

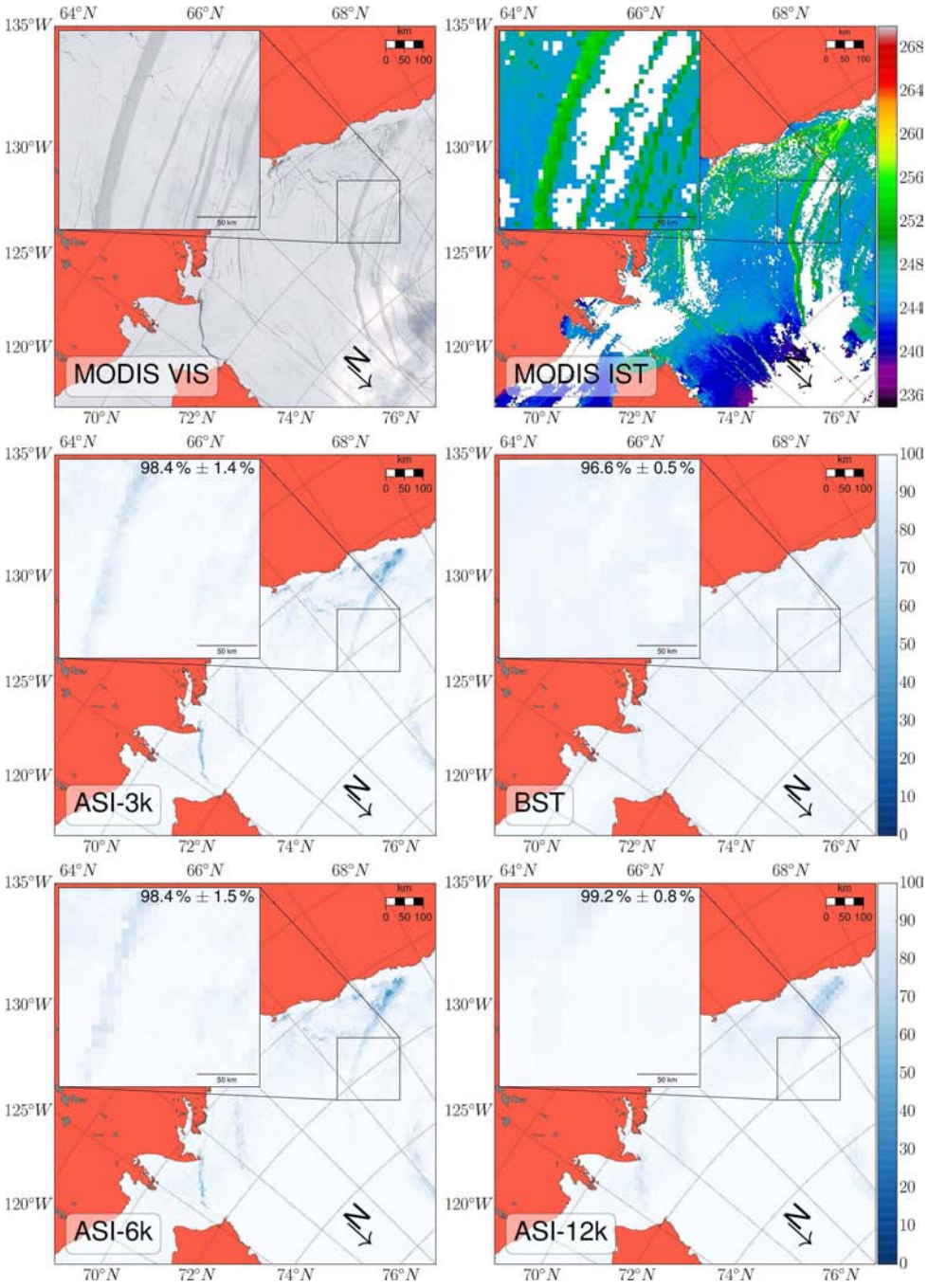

Figure 4.3: Same as Figure 4.1, but for 26 Februar 2013.

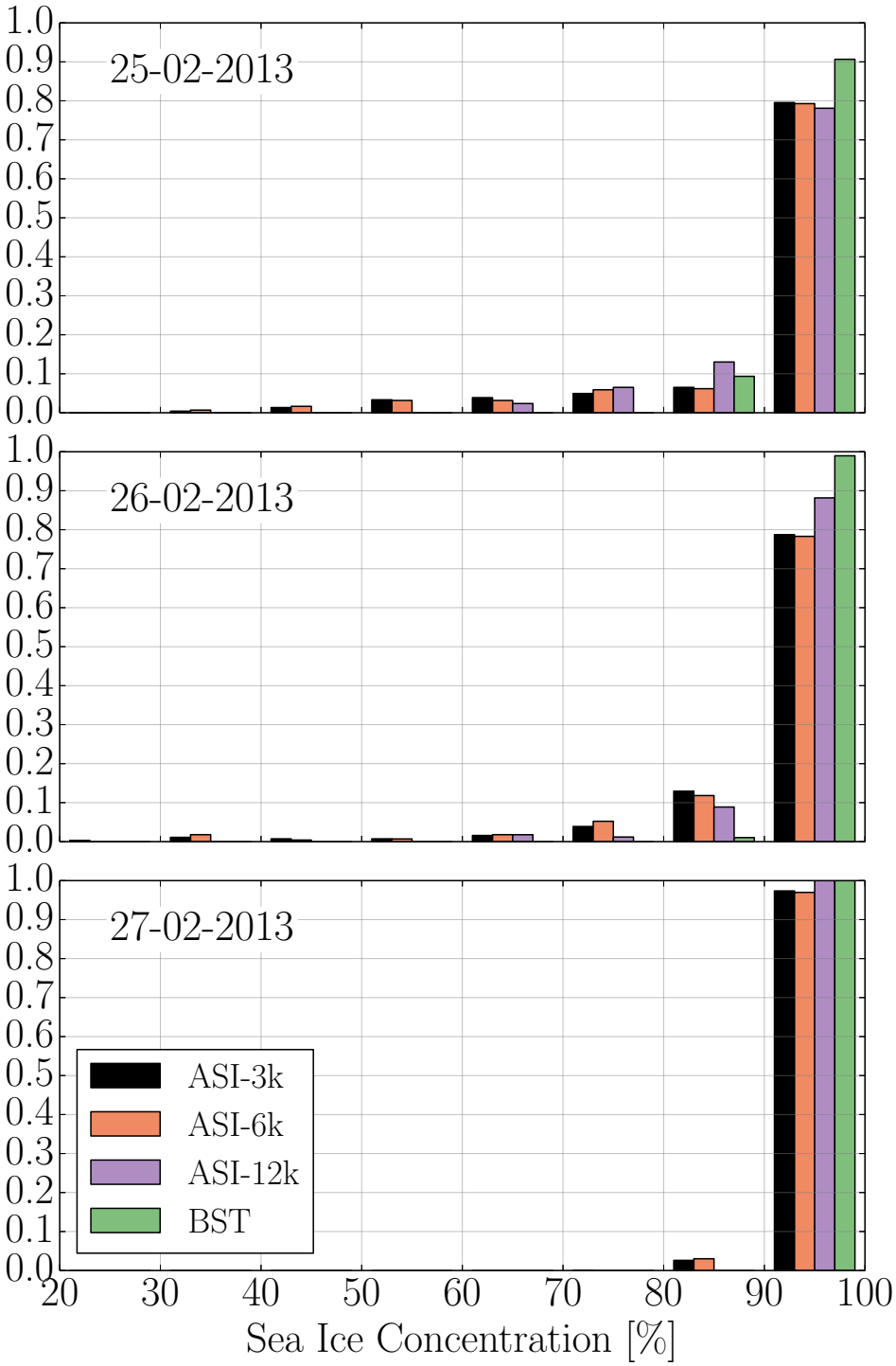

Figure 4.4: Histogram of the relative probability of SIC in the insets shown in Figures 4.1–4.3, respectively. Sea ice concentrations from ASI-3k, ASI-6k, ASI-12k and BST are shown in bins of 10%, for ranges 21%–30%, 31%–40%, ... 91%–100%. A legend in the lowest panel indicates the different data. Note that the abscissa in the three panels start with 20%.

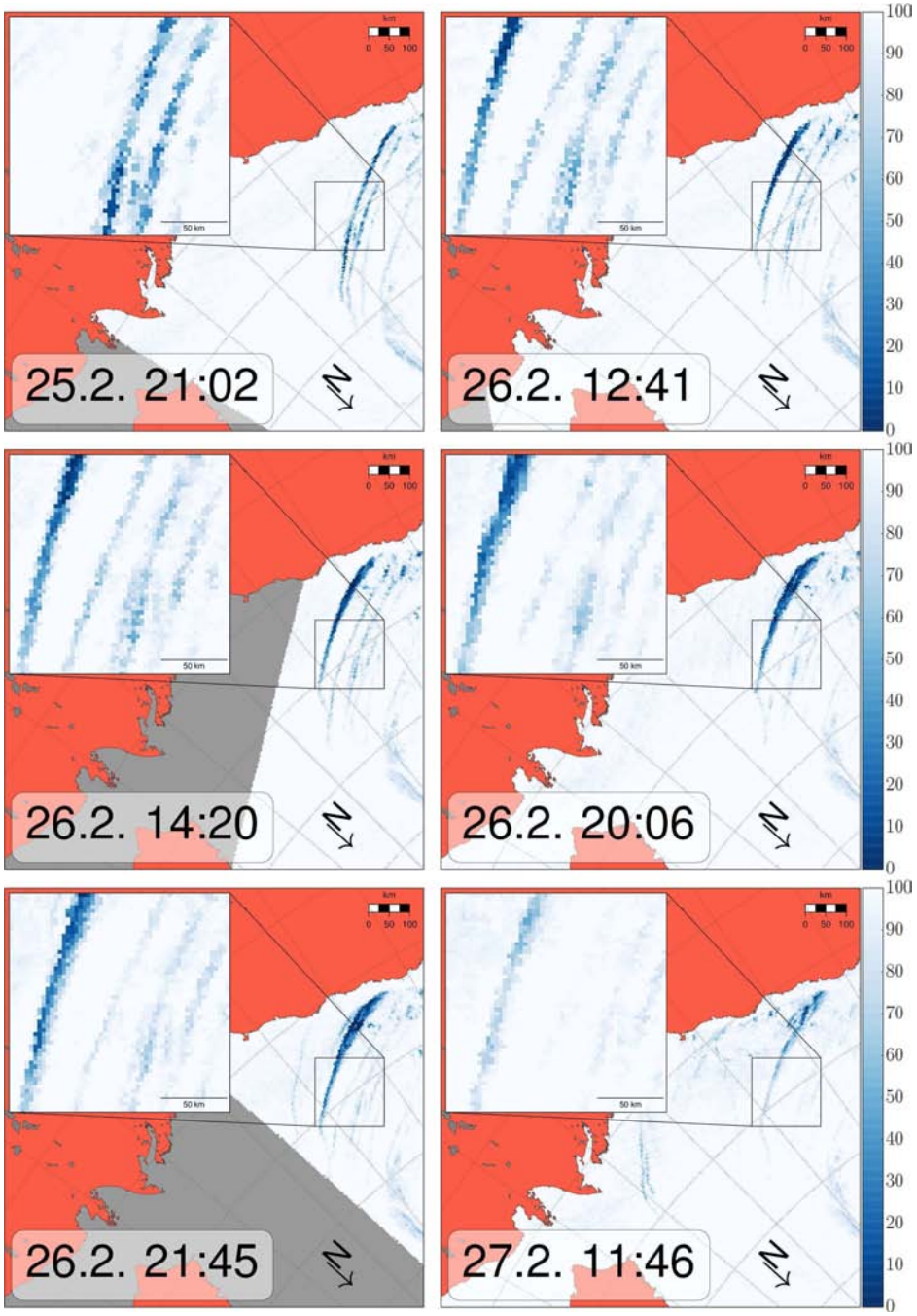

Figure 4.5: Evolution of the Feb-26-lead in ASI-3k from 25 February until 27 February 2013. We choose individual swaths, which cover the region of interest and depict the opening and refreeze of the Feb-26-lead. The date and start time of the individual swaths is displayed in the individual maps. The same projection and labeling as in Figures 4.1–4.3 apply. The gray areas depict missing data.

upper right corner of the individual insets for SIC data in Figures 4.1–4.3). For single pixels within this lead, differences between ASI-3k and BST can be 60 % in sea ice concentration. In contrast, ASI-12k data look very similar to BST, suggesting that the footprints at 18 and 36 GHz are too large to resolve the Feb-26-lead. These footprint's signatures include contributions from the nearby thick sea ice.

The gain of information due to the higher resolution in SIC data is shown in histograms in Figure 4.4. ASI-3k and ASI-6k are able to detect SIC in the range of 30–80% on 25 February and 26 February, respectively. These low- to mid-level SIC stem from the lead, which is westward of the Feb-26-lead (see Figure 4.1). In the high SIC bin (>90%), all ASI-based SIC data reveal less ice than BST. ASI-12k shows the lowest relative probability in this bin due to the larger grid size, but, in contrast to ASI-3k and ASI-6k, ASI-12k is not able to detect SIC less than 60%. The differences in relative probability between ASI-3k and ASI-6k are quite small for 25–26 February. On 27 February, the area in the inset is almost completely refrozen according to the SIC data with only ASI-3k and ASI-6k displaying SIC in the 80%–90%-bin.

The dynamic evolution of the ice cover complicates a comparison on a daily-mean basis. Considering ASI-3k SIC retrieved from single-swath TB data reveals more details on the development of the Feb-26-lead and its refreezing (Figure 4.5). The Feb-26-lead develops between 21:02 UTC on 25 February and 12:41 UTC on 26 February. The MODIS scene, which most of the tile shown (MODIS VIS, Figure 4.2) is based on, was recorded at 20:55 UTC. The lead shows a higher albedo and, therefore, a refrozen surface in the northern part of the image. The southern part, also partly visible in the inset, has substantial open water fractions on the windward side and within the new ice on the leeward side of the lead. We investigate the size of the Feb-26-lead in the SIC data by calculating the open water fraction of the lead separately for each of the swaths shown in Figure 4.5. For that, we select a region around the Feb-26-lead and generate a mask that only considers SIC values below 50% in this region based on the daily-mean ASI-3k data. Note that this analysis is based on the assumption of no drift. This would introduce an error when the lead is displaced. From 25 to 27 February, the open water fraction increases from 0% on 25 February to ∼80% on 26 February and decreases to ∼15% on 27 February. Based on this calculation, the Feb-26-lead reaches its maximum size on 26 February between the AMSR2 overflights at 14:20 UTC and 20:06 UTC.

4.5 Discussion

In the previous section, we presented a case study using a new 3.125 km passive-microwave sea ice concentration (SIC) data set that is calculated based on AMSR2 Level-1R brightness temperature (TB) measurements. In November 2004, the A-scan of the 89 GHz feedhorn of AMSR-E measurements started producing corrupted data,

after which these scan data had to be discarded. With AMSR2, we provide twice the resolution of the previous 6.25 km grid resolution that was used for AMSR-E.

We compared different data sets for a late winter situation when several elongated and relatively wide leads occurred in the Beaufort Sea. One of those leads, the Feb-26-lead, was on the order of 1000 km long. The ASI SIC data on a 3.125 km grid (ASI-3k) resemble the pattern of the fractured sea ice cover as it is visible in a MODIS True Color image (MODIS VIS) and the MODIS ice surface temperatures (MODIS IST). Discrepancies exist when comparing ASI-3k to JAXA's Bootstrap-based SIC data. Bootstrap (BST) is a mature, well-validated algorithm that is known to represent local SIC very accurately (Beitsch et al., 2014). In this particular case, however, BST SIC do not show the Feb-26-lead structures as they are visible in MODIS VIS, the ASI-3k, and the ASI-6k images. ASI-3k and ASI-6k show a considerable open water fraction in the southern part of the Feb-26-lead (above the inset in the maps shown). Our analysis suggests the differences to BST SIC arising from the larger footprints of the lower frequencies that are used in the BST retrieval. At these lower frequencies, the TB signal of pixels located within the Feb-26-lead is influenced by surrounding thicker sea ice, which is characterized by much higher TB than the open water surface and new ice in the lead. Therefore, these pixels show a temperature mix of the open water, new ice, and thick sea ice. Additionally, the microwave signal is very sensitive to the location of one measurement, i.e., the location of the footprint; this can result in large differences for the calculation of SIC if the center of a footprint is located within the open water area or if it is located at the margin of a lead with a considerable influence of the thicker sea ice surface. In the ASI-3k and ASI-6k maps, more structural details of the Feb-26-lead are visible than in the BST SIC map and in the ASI-12k data. ASI-12k simulates the larger footprint of the 18 GHz measurements that are input to the BST retrieval. This simulation confirms the disadvantage of lower-frequency-based SIC retrievals in resolving the details of lead structures during the period that we show in our case study.

We cannot determine quantitatively if and how much ASI-3k overestimates the open water in the Feb-26-lead. The east-west gradient in the albedo within the Feb-26-lead visible in the MODIS True Color maps indicates the presence of both open water and new ice. The albedo of the new ice part of the Feb-26-lead seems to suggest relatively thick new ice, like light nilas or grey ice. However, such a high albedo can also be caused by frost flowers growing on thin new ice, like dark nilas under cold conditions (Nghiem et al., 2012). The existence of cloud streets advected downwind of the Feb-26-lead ensures that a substantial amount of open water existed to which the two used SIC retrieval algorithms are sensitive, provided that the achieved spatial resolution is fine enough. Only with the new ASI SIC data set with 3.125 km grid resolution, the structure, position and size of all the leads displayed in MODIS imagery shown for the tree consecutive days in February 2013 (Figures 4.1–4.3) are depicted correctly.

Larger uncertainties or even biases can be expected in the retrieved SIC, because

the radiometric surface properties of thin ice differ from those of thick ice, whose radiometric properties determine the sea ice tie points used in the SIC algorithms. Evidence for a thin ice SIC bias have been found in a number of studies (Shokr and Kaleschke, 2012; Cavalieri, 1994; Shokr and Markus, 2006; Cavalieri et al., 2006a). In the present study, emphasis is put on the occurrence and structure of the leads rather than onto a correct quantification of SIC in the lead itself. Natural variability in sea ice properties, e.g., due to snow metamorphism or ice-snow interface roughness changes, causes a variability in the retrieved SIC of a few percent (Andersen et al., 2007). This is an uncertainty high enough to make the detection of changes by 1–2% in high ice concentration areas, e.g., due to leads, impossible. In the present study, however, the short duration of the investigation period of three days and the constantly cold, dry conditions ensure minimum day-to-day variation in SIC due to the above-mentioned property changes.

Reductions in winter SIC of a few percent are known to already induce great effects in the lower atmospheric heat budget because of increased ocean-atmosphere heat exchange (Marcq and Weiss, 2012). With a high resolution SIC data set, it is more likely to correctly detect such SIC variations and, hence, to provide the basis for a more realistic quantification of winter-time ocean-atmosphere heat exchange. The ASI-3k is able to depict smaller-scale openings in the sea ice cover and shows an open water fraction, which is 4 % higher than the one from BST for our area of interest of size 170 km × 170 km in the Beaufort Sea. Within this area, differences for single pixels are up 60 % in sea ice concentration.

4.6 Conclusion

In summary, we present a new high-resolution sea ice concentration data set based on satellite microwave radiometry that is able to provide more details of a fractured sea ice cover than sea ice concentration data at lower spatial resolutions. This is achieved by applying the ARTIST Sea Ice (ASI) algorithm to brightness temperatures measured at a frequency of 89 GHz by the Advanced Microwave Scanning Radiometer-2 (AMSR2). This enables to retrieve sea ice concentrations at 3.125 km grid resolution (ASI-3k SIC). The data set has the potential to provide a more realistic boundary condition when calculating atmosphere-ice-ocean exchange processes. A high-resolution SIC data set is an advantage for navigation through the sea ice cover, as well as for mesoscale process studies (Kaleschke et al., 2001), and daily-mean ASI-3k SIC provide a high level of details about the ice pack. However, if knowledge about sea ice concentration for a specific point in time is required (e.g., for data assimilation), we recommend, based on our investigation of spatial resolution and temporal sampling, using ASI-3k SIC calculated from individual swath data if available, because more details of an ice situation for a defined time can then be obtained.

Acknowledgements

We acknowledge funding by the Bundesministerium für Wirtschaft und Technologie (BMWi, Federal Ministry of Economics and Technology) through the project "Ice-Route-Optimization-2" (IRO-2, U-4-6-03-BMW-11-02) in the framework of the program "Shipping and ocean engineering for the 21st century", and funding through the Deutsche Forschungsgemeinschaft (DFG, German Research Foundation) through the Cluster of Excellence (CliSAP, EXC 117). We acknowledge the use of Rapid Response imagery from the Land Atmosphere Near-real-time Capability for EOS (LANCE) system operated by NASA's Goddard Space Flight Center Earth Science Data and Information System (ESDIS) with funding provided by NASA Headquarters. We thank JAXA (`http://www.jaxa.jp/index_e.html`) for the provision of AMSR2 data. Rein Klazes helped to reduce errors in the processing of the AMSR2 data. Monika Onken and David Bröhan provided their Python codes for plotting MODIS tiles and zooming into a data array, respectively; both of these programs were used as a starting point for the graphics shown in Figures 4.1–4.3 and Figure 4.5. Re-sampling was done using Python's pyresample (`https://pyresample.readthedocs.org/en/latest/index.html`). We thank Nina Maaß, Maciej Miernecki, and Mark Carson for valuable discussions and help on the manuscript. Three anonymous reviewer helped to improve the manuscript.

Chapter 5

Snow Surface and Atmospheric Influences on retrieving Sea Ice Concentrations

5.1 Introduction

Uncertainties of up to 5 % for retrieved sea ice ice concentrations have been found during winter when the ice cover is near 100 % (Andersen et al., 2007). Most of the uncertainty can be attributed to surface emissivity variations. Even for 89 GHz-channels, which are especially sensitive to atmospheric water vapour and cloud liquid water, the surface influence very often dominates over the atmospheric influence during winter (Andersen et al., 2007). The atmospheric effects decrease linearly with increasing ice concentrations and are thought to become insignificant near 100 % ice concentration. Therefore, surface emissivity variations are expected to dominate the uncertainty of sea ice retrievals at high ice concentrations due to physical processes in the snow and ice cover.

The polar sea ice is usually covered by a snow layer. Besides increasing the sea ice's insulation of the atmosphere from the ocean, a snow cover usually influences microwave radiation at most frequencies, depending on snow layer depth, snow density, snow grain sizes, liquid water content, and salt intrusion from the ice cover beneath the snow (see Mätzler et al., 1984; Warren et al., 1999; Massom et al., 2001, and references therein). The microwave signature of a snow surface is defined by the attenuation and scattering of the radiation within the ice and snow cover. These processes depend on temperature gradient, the amount of layers of ice and snow, and the bulk physical properties thickness of a single layer, temperature, and salinity (e.g., Wiesmann et al., 2000).

The 89 GHz measurements that are used in the ASI algorithm, i.e., the brightness temperature polarization difference P_{89} (see Section 2.2.1, Chapter 3, and Chapter 4),

are sensitive to snow cover on sea ice. The sea ice has a considerable salinity, which leads to high absorption coefficients and, thus, limits any further penetration. The penetration depth in snow on sea ice is a function of the liquid water content and also depends on the size of the snow grains. In general, the interaction of microwave radiation with snow depend on the frequency of the radiation. While the dielectric loss of snow is small, the attenuation of radiation in dry snow is mainly controlled by scattering. The effect of scattering increases at higher frequencies, for larger particles, and drier snow. Additionally, the higher the liquid water content, the higher is the loss of the radiation in the medium, which eventually dominates over scattering. This means for 89 GHz, increasing wetness in snow leads to a decrease in penetration depth. In summary, the 89 GHz measurements have passive microwave signatures that are ultimately linked to the surface snow. Thus, variations in P_{89} at near 100 % ice concentrations are mostly due to physical changes in the snow cover on top of the sea ice. Linking the observed variations in P_{89} to known changes in snow cover parameters can help to estimate the uncertainty in retrieved sea ice concentrations during winter. Additionally, periods exist with no or very small variations in surface emissivities but simultaneous variations in retrieved brightness temperatures. Then, these variations are caused by increased atmospheric contamination due to water vapour and cloud liquid water droplets.

An example for increased atmospheric water and changes in surface emissivities on retrieving SIC with ASI is given in Figure 5.1. During the period shown, a low-pressure system passed the East Siberian Sea (see Figure 2.1), increased cloudiness and precipitated snow in parts of the Central Arctic close to the Laptev Sea. ASI SIC are reduced for these regions during this period. As we know from previous investigations, this is most probably not a true variability in SIC and can very likely be attributed to a weather effect on the brightness temperatures, which reduces retrieved SIC (Andersen et al., 2007). Weather influences the radiation received at the radiometer directly and indirectly. The direct effect results from the atmospheric contamination; the signal received by the sensor is attenuated when passing through the atmosphere. Another effect is indirect by changing surface properties and, hence, the emissivity of the surface due to precipitation or snow metamorphism or both. The strongest reductions are stationary and, therefore, linked to surface emissivity changes, while other visible reductions travel east-west, starting near Chukchi Sea and moving to the western Arctic, indicating atmospheric parameters to interfere with the retrieval. But how much of these uncertainties can actually be attributed to atmospheric or surface processes? And can we deduce an order of magnitude of the changes linked to variations in SIC?

In this study, we investigate the impact of physical snow and ice parameters, and changing atmospheric opacities on simulated emissivities and simulated brightness temperatures (TBs) from the ESA-CCI Sea Ice Essential Climate Variable Project Round Robin Data Package (RRDP, Pedersen and Saldo, 2012). The data are based on simulations with the combined thermodynamic and emissivity model MEMLSI (described in

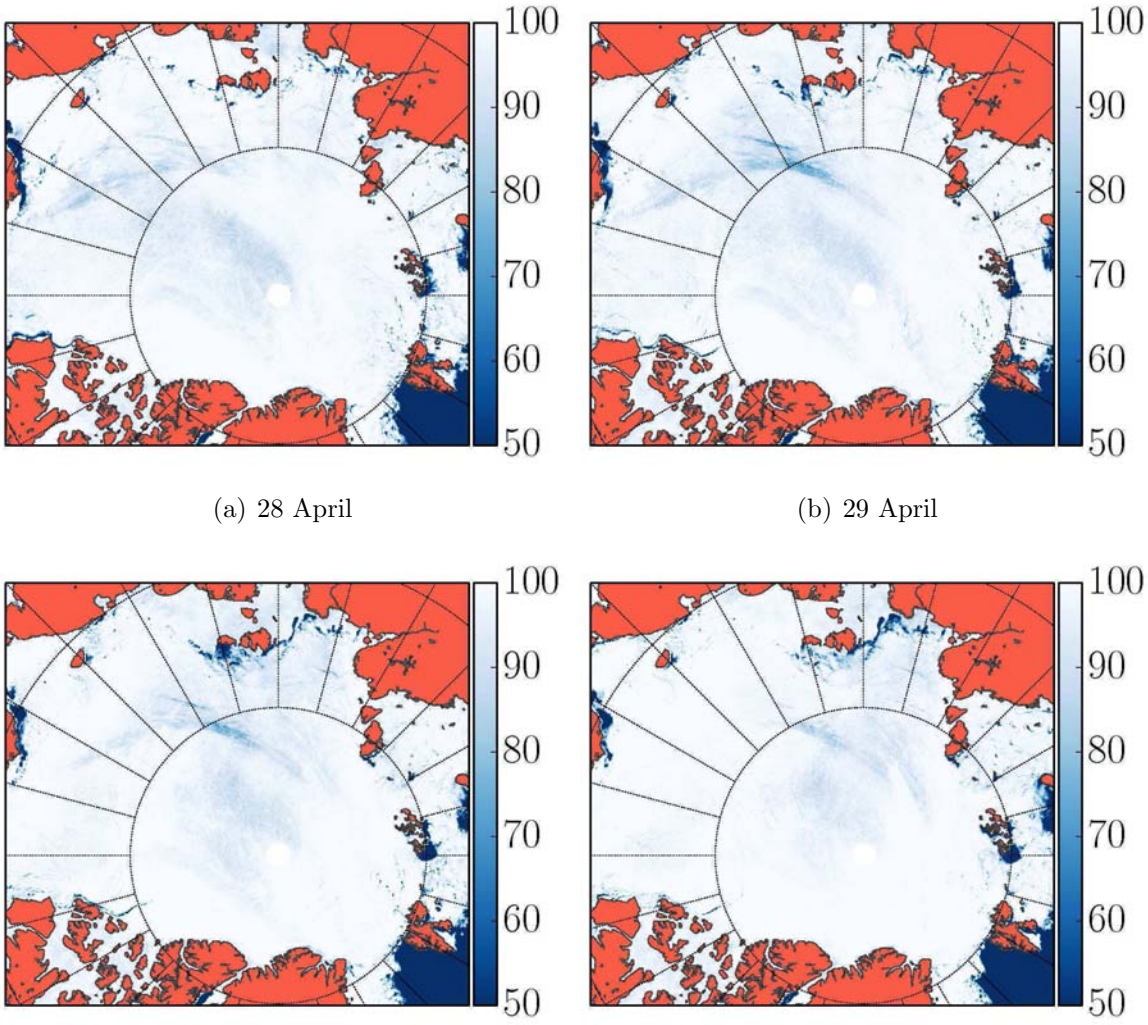

(a) 28 April

(b) 29 April

(c) 30 April

(d) 1 May

Figure 5.1: A series of four daily sea ice concentration (SIC) maps for (a) 28 April, (b) 29 April, (c) 30 April, and (d) 1 May 2014 in the Central Arctic when different processes influence the accuracy of retrieving SIC. The maps are based on SIC retrieved with the ARTIST sea ice algorithm (ASI) using data from the Advanced Microwave Scanning Radiometer 2 (AMSR2). To increase the visibility of changes in SIC in the Central Arctic, we limit the colorbar to SIC values 50-100 %. Continental areas are displayed in coral.

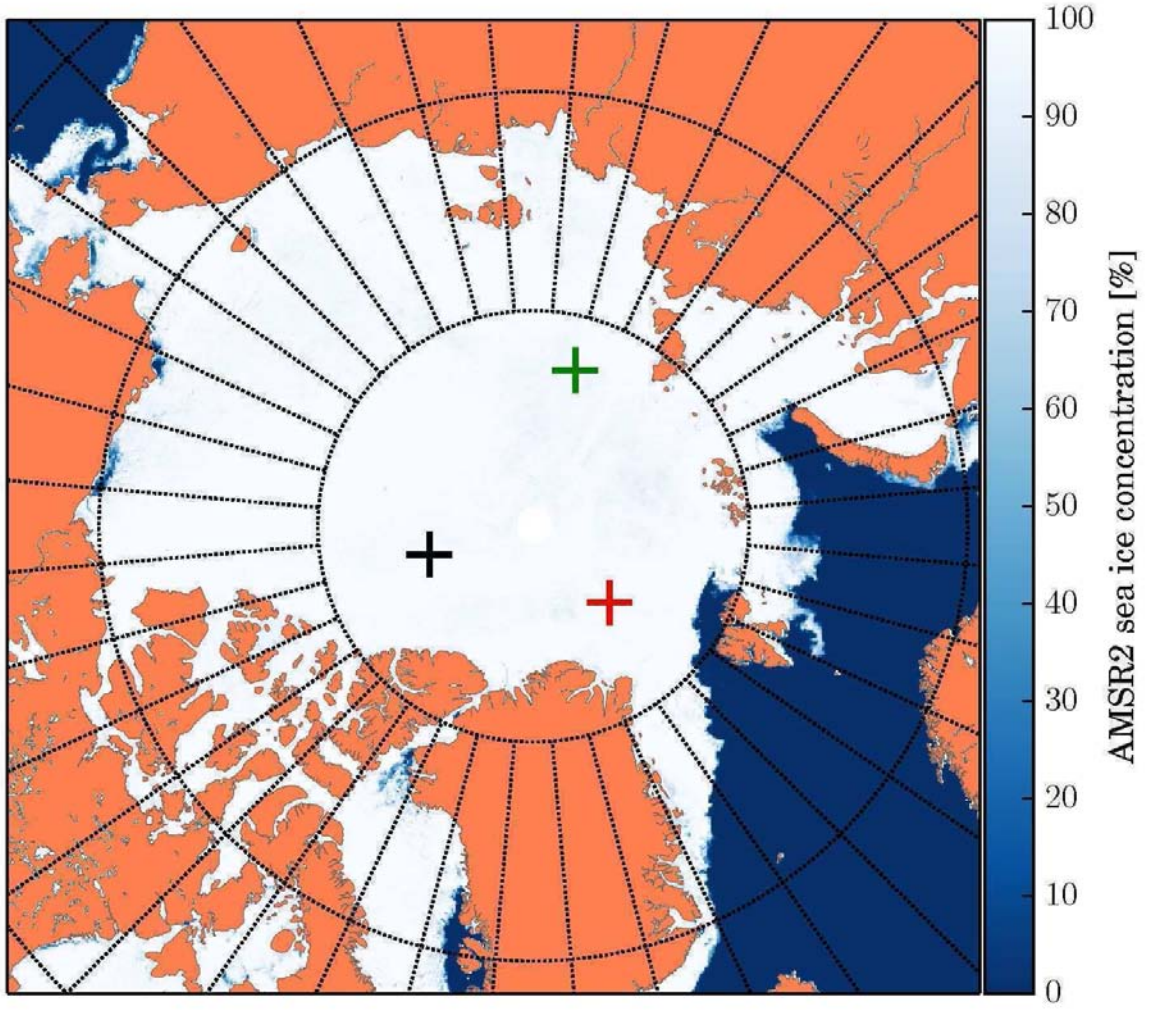

Figure 5.2: Locations for the simulations with MEMLSI marked on a ASI sea ice concentration map for Jan 1, 2014. The red cross denotes a multi-year ice (MYI) location north of Fram Strait (FS), the black cross denotes a MYI location in the Central Arctic (CA), and the green cross denotes a first-year ice (FYI) location in the northern Laptev Sea (LS).

Chapter 2). Based on these simulations, we can estimate the sensitivity of the 89 GHz measurements, and thus on the retrieved sea ice concentrations, to physical changes in the surface snow cover and variations in atmospheric opacity due to water vapour and clouds.

5.2 Influence of Snow Fall Events on retrieving Sea Ice Concentrations at 89 GHz

Penetration of microwave radiation into snow and ice depends on the attenuation and scattering of the microwaves in the media. At 89 GHz, the penetration is very limited

due to strong attenuation by scattering (Barber et al., 1998; Grenfell et al., 1998). If liquid water is present in the snow cover, attenuation increases due to higher extinction in the media. This means that microwave penetration at 89 GHz is usually limited to the snow layer. Therefore, snow surface emissivity variations depend on physical processes within the snow cover. Besides microphysical parameters in the snow profile like physical temperature, salinity, and density, the size of the grains in the snow directly influences the emissivity of the snow. But with all of these parameters being linked to the density, only considering surface snow density changes can serve as a proxy for microphysical snow changes and their impact on microwave radiation.

To estimate the sensitivity of P_{89} to physical changes in the snow, we investigate snow fall events and consequent changes in emissivity polarization difference P_{e89} for three locations in the Arctic (Figure 5.2). In contrast to P_{89}, P_{e89} is not influenced by the atmosphere and we can directly link changes in microwave signals to physical changes in the surface snow layer(s). For two of the three locations, the evolution for multi-year ice (MYI) and its snow cover is simulated starting with a 2.5 m-thick ice layer on 1 September. These simulations are located in the Central Arctic at 85° N and 120° W and north of Fram Strait at 85° N and 0° E. For the third location, the evolution of first-year ice (FYI) and its snow cover is simulated starting with no ice cover on 1 October. This simulation is located in the Laptev Sea at 82.5° N and 120° E as defined in Figure 5.2.

Abrupt changes in P_{e89} are associated with snow fall events (Figure 5.3). We mark snow fall events according to increases in the snow thickness h_{snow} in all time series displayed here (Figures 5.3-5.4) color-coded for the three locations as defined in Figure 5.2.

5.2.1 Simulation in the Central Arctic (CA)

For the location in the Central Arctic (CA), Table 5.1 shows changes in P_{e89}, surface snow density ρ_{snow} (Figure 5.3), and average snow density $\bar{\rho}_{snow}$ (Figure 5.4) for seven snow fall events. Additionally, numbers are provided for the 2 m air temperature T_a just before the snow fall event happens, the 2 m air temperature change ΔT_a, the mass of precipitation Ms, and the change in snow thickness Δh_{snow}. We have three criteria to choose a snow fall event for further investigation. First, the time series of P_{e89} shows a considerable change compared to the values before the event, second, values of P_{e89} show microwave signatures of and can be attributed to snow on sea ice, and third, we regard only snow fall events with a minimum snow thickness increase of 1 cm. These criteria are fulfilled for the events 1–7 labeled in Figures 5.3–5.4. For events 1, 3, 6, and 7, the new surface snow layer has a lower density than the old surface snow layer and we find a decrease of the polarization difference at 89 GHz (see Table 5.1 and the panels in Figure 5.3). A new snow layer with lower density than the old surface snow layer decreases the average snow density of all snow layers $\bar{\rho}_{snow}$ (see Table 5.1 and

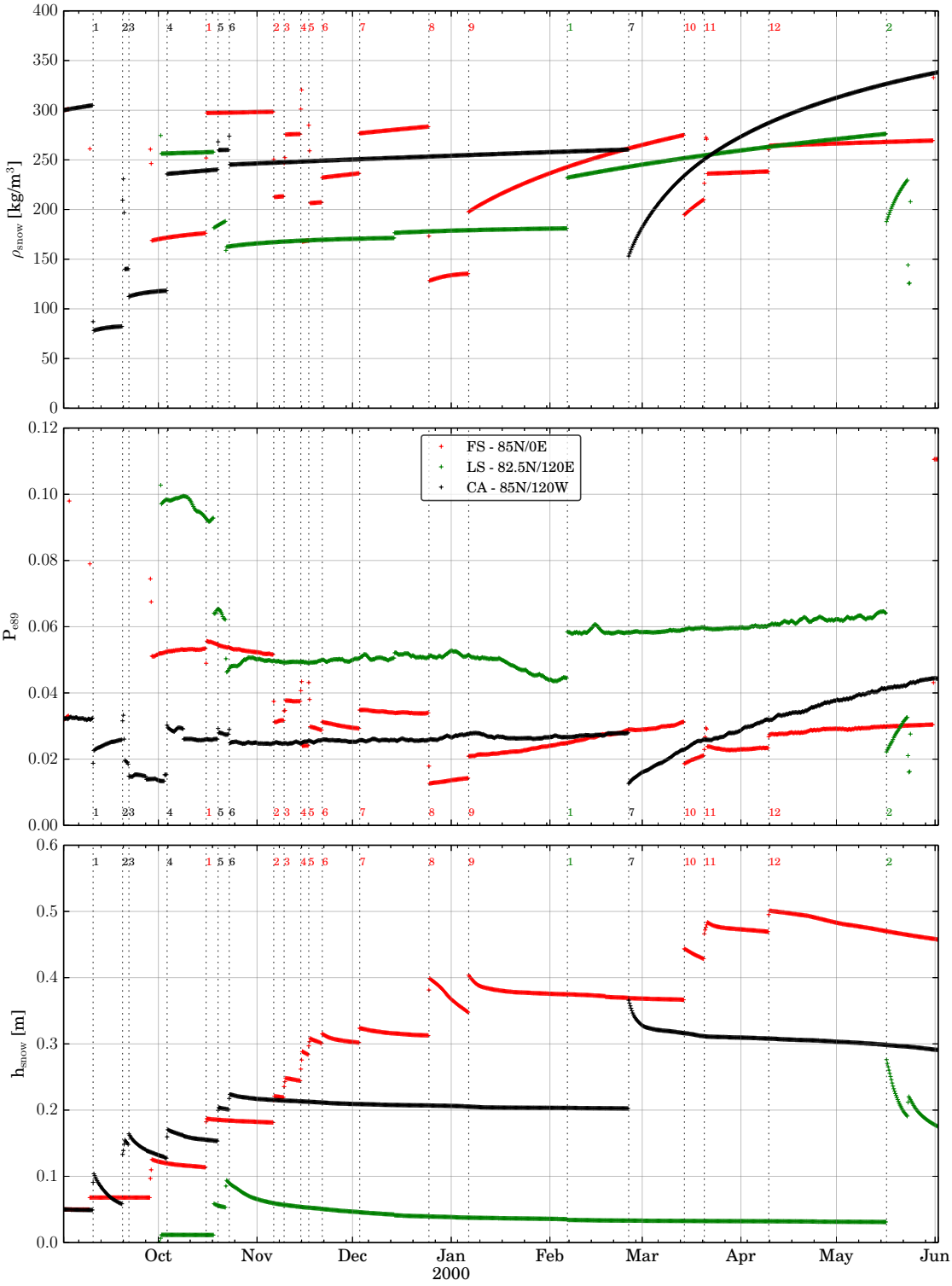

Figure 5.3: Time series of the density of the surface snow layer ρ_{snow} (top), the polarization difference of emissivities at 89 GHz P_{e89} (middle), and the snow thickness h_{snow} (bottom), from MEMLSI modeled for three locations in the Arctic (Figure 5.2). Colors denote the three locations as indicated in the legend. The dashed vertical lines and the color-coded numbers denote certain dates for the individual locations, which we will refer to in the following.

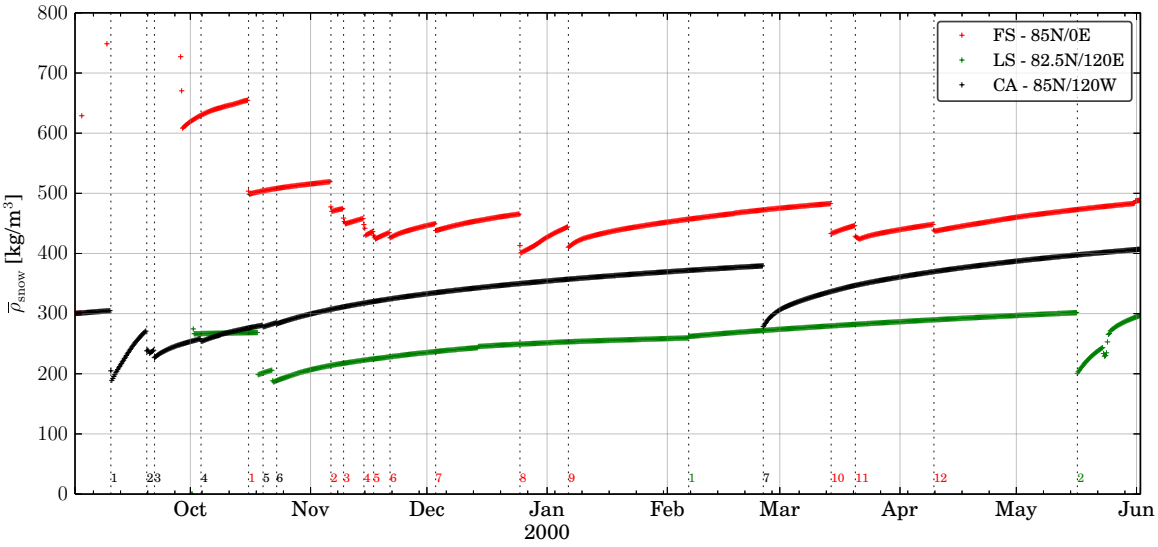

Figure 5.4: Same as Figure 5.3, but only for the average density of the snow, $\bar{\rho}_{\text{snow}}$.

Figure 5.4). However, a new snow layer with denser snow decreases P_{e89} (compare with events 2, 4, and 5). The density of a new surface snow layer formed by precipitation is a function of T_a, and the wind speed (Tonboe et al., 2011). With every snow fall event, air temperatures increase but stay below freezing during all events. The temperature increase is due to the entrainment of warmer air layers above the Arctic inversion. The air aloft the inversion is also warmer due to latent heat release from snow formation in the upper layers and because a precipitation events can often be attributed to an approaching low-pressure system that leads to advection of warmer air.

But how does P_{e89} develop during the periods between the snow fall events? Not only instantaneous changes in P_{e89} due to snow fall events but also the evolution of the density of the surface snow layer between snow fall events has an influence on simulated P_{e89}. Table 5.2 shows the changes in h_{snow}, P_{e89}, ρ_{snow}, and $\bar{\rho}_{snow}$ between new snow fall events. Leaving out periods when there is no clear tendency in P_{e89} during a period, the periods between events 1–2 and the period after event 7 show an increase in ρ_{snow} due to snow metamorphism (Figure 5.3). Consequently, snow thickness reduces. But more importantly, P_{e89} increases when the surface snow layer ages, and mean grain sizes and density increase (Figure 5.3). Especially for a long period starting end of February, a concurrent increase in ρ_{snow} and P_{e89} can been seen. The mean grain size in the different snow layers increases over time as a function of temperature gradient, temperature and density (Tonboe, 2010). As a consequence of the snow metamorphism, the density increase of the other snow layers leads to the simulated decrease in snow thickness. We do not investigate the other periods because of either no or no considerable changes in P_{e89} or ρ_{snow}.

Table 5.1: Qualitative (upper) and quantitative (lower) parameter changes in the snow cover due to the snow fall events at the location CA (Figure 5.2). The investigated parameters include the polarization difference of emissivities at 89 GHz P_{e89}, the density of the surface snow layer ρ_{snow}, the average density of all snow layers ρ_{snow}, the (2 m) air temperature T_a just before a snow fall event happens, the (2 m) air temperature change ΔT_a, the mass of precipitation Ms, and the increase in snow thickness Δh_{snow}. Numbers refer to black labels at snow fall events, shown in Figures 5.3-5.4. An increase or a decrease of a property is indicated by ↑ or ↓, respectively.

Snow event	1	2	3	4	5	6	7
P_{e89}	↓	↑	↓	↑	↑	↓	↓
ρ_{snow}	↓	↑	↓	↑	↑	↓	↓
$\bar{\rho}_{snow}$	↓	↓	↓	-	-	-	↓
ΔT_a [K]	+1.1	+2.1	+2.6	+1.5	+1.4	+5.6	+2.3
T_a [K]	265	269	271	265	257	254	252
Ms [kg/m^2]	5.0	21.0	2.1	10.4	12.5	6.1	25.5
Δh_{snow} [cm]	+1.3	+5.1	+1.0	+4.3	+3.0	+2.4	+14.2

Table 5.2: Qualitative parameter changes between the snow fall events at location CA (shown in Figure 5.2). Numbers indicate periods between the events depicted in Table 5.1. In contrast to Table 5.1, where abrupt changes are considered, an increase or a decrease of a property is now indicated by ↗ or ↘, respectively, because of transient changes during the periods. ¯indicate no change; parentheses indicate insignificant changes.

Period	–1	1–2	2–3	3–4	4–5	5–6	6–7	7–
ΔP_{e89}	-	↗	↘	↘	↘	-	-	↗
$\Delta \rho_{snow}$	↗	↗	(↗)	↗	(↗)	↗	↗	↗
$\Delta \bar{\rho}_{snow}$	↗	↗	-	↗	↗	↗	↗	↗
Δh_{snow}	-	↘	↘	↘	↘	↘	↘	↘

Table 5.3: Same as Table 5.1, but for location FS.

Snow event	1	2	3	4	5	6
P_{e89}	↓	↓	↑	↑↓	↑	↑
ρ_{snow}	↑	↓	↑	↑↓	↑	↑
$\bar{\rho}_{snow}$	↓	↓	↓	↓	↓	↓
ΔT_a [K]	+2.0	+2.1	+0.3	+15.1	-1.7	+1.0
T_a [K]	256	263	255	255	266	269
Ms [kg/m^2]	17.3	8.5	4.0	12.1	3.9	3.5
Δh_{snow} [cm]	+6.8	+3.4	+1.6	+4.4	+1.3	+1.4
Snow event	7	8	9	10	11	12
P_{e89}	↑	↓	↑	↓	↑	↑
ρ_{snow}	↑	↓	↑	↓	↑	↑
$\bar{\rho}_{snow}$	↓	↓	↓	↓	↓	↓
ΔT_a [K]	+1.0	+6.3	-0.55	+2.0	+0.9	+2.3
T_a [K]	250	245	269	256	266	252
Ms [kg/m^2]	6.0	14.4	11.4	15.0	8.7	6.7
Δh_{snow} [cm]	+2.2	+8.6	+5.6	+7.7	+3.8	+2.6

5.2.2 Simulation in the north of Fram Strait (FS)

The location north of Fram Strait (FS) experiences 12 snow fall events that fulfill our criteria. This is considerable more precipitation events as for the MYI location CA, and they usually happen during colder temperatures (Table 5.3). Note that we do not take into account the snow fall event at the end of September, because the surface signatures at 89 GHz do not show values corresponding to a fully covered ice or snow surface (values exceed the range of P_{e89} shown in Figure 5.3). The snow fall events 2, 8, and 10 provide a new snow layer with lower density than the old surface snow layer and show a decrease in P_{e89} (see Table 5.3 and Figure 5.3). During snow fall events 3, 5, 6, 7, 9, 11, and 12, ρ_{snow} and P_{e89} decrease. The event 4 is special in that it shows an increase in ρ_{snow} and P_{e89} followed by a sudden decrease after 2 time steps.

The periods between events 8–9, 9–10, 10–11, and after event 12 show a considerable increase in ρ_{snow} and P_{e89} (Table 5.4 and Figure 5.3). The periods between events 1 –2, 6–7, and 7–8 show increasing ρ_{snow} with a decrease in P_{e89}. The tendency in both parameters are small for these periods, however, they contrast our findings so far. We do not discuss the other periods, because we can not find a clear tendency in ρ_{snow} or P_{e89}.

5.2.3 Simulation in the Laptev Sea (LS)

The third location in the Laptev Sea (LS), experiences 4 snow fall events (Table 5.5). We mark only one of the snow fall events in the time series (event 2 in Figures 5.3-

Table 5.4: Same as Table 5.2, but for location FS.

Period	–1	1–2	2–3	3–4	4–5	5–6	6–7
ΔP_{e89}	↗	↘	-	-	-	-	↘
$\Delta \rho_{snow}$	↗	↗	-	-	-	-	↗
$\Delta \bar{\rho}_{snow}$	↗	↗	-	-	-	-	↗
Δh_{snow}	↘	↘	-	↘	↘	↘	↘

Period	7–8	8–9	9–10	10–11	11–12	12–
ΔP_{e89}	↘	↗	↗	↗	-	↗
$\Delta \rho_{snow}$	↗	↗	↗	↗	-	↗
$\Delta \bar{\rho}_{snow}$	↗	↗	↗	↗	↗	↗
Δh_{snow}	↘	↘	↘	↘	↘	↘

5.4) because the snow cover was very thin during October, the first month of the simulation. However, both of the not marked snow events show a concurrent decrease in ρ_{snow} or P_{e89}. During the second half of May, the last snow fall event happens with air temperatures close to and partly above freezing (not shown). Since MEMLSI is not intended to simulate melt processes and simulated brightness temperatures and emissivities cannot be attributed to surface snow density changes alone, we discard this event. Event 1, although not a snow fall event, is outstanding in that it shows a considerable change in P_{e89} with no concurrent snow fall. During this event, the temperature gradient within the snow cover changes sign and exhibits values close -80 K/m for 2 modeling time steps (not shown). Because the snow layer is already quite thin, the increased snow metamorphosis due to the extreme temperature gradient does not result in a considerable change in h_{snow}, but in ρ_{snow} and therefore P_{e89}. For the snow fall event 2 that provides a considerable snow thickness increase of 25 cm, we observe a considerable decrease in ρ_{snow} and P_{e89}. The period after the event 2 shows a considerable increase in P_{e89} until above freezing temperature are reached in mid-May (Figure 5.3 and Table 5.5).

During the period between events 1–2 snow thickness only slightly decreases, and ρ_{snow} and P_{e89} slightly increase. In contrast, the period after event 2 (increase in snow layer height of ∼25 cm) experiences a considerable increase in P_{e89} and considerable snow metamorphosis afterwards (Table 5.4). During this period, ρ_{snow} and P_{e89} show a strong increase within 10 days (Figure 5.3).

5.2.4 Summary

Snow surface layer density changes due to snow fall events are associated with a change in emissivity polarization difference at 89 GHz P_{e89} of the same sign. P_{e89} decreases if the snow surface layer density decreases and P_{e89} increases if the snow surface layer density increases. After snow fall events, P_{e89} often increases due to snow metamorphism in an aging surface snow layer.

Table 5.5: Qualitative (upper) and quantitative (lower) parameter changes in the snow cover due to the snow fall events (left table) and qualitative parameter changes between snow fall events (right table) at location LS (shown in Figure 5.2). Numbers refer to green labels at snow fall events, shown in Figures 5.3-5.4. An increase or a decrease of a property is indicated by ↑ or ↓ for the snow fall events, respectively. Tendencies during periods in between snow fall events are indicated by ↗ or ↘, respectively.

Snow event	1	2
P_{e89}	↑	↓
ρ_{snow}	↑	↓
$\bar{\rho}_{snow}$	↑	↓
ΔT_a [K]	+3.4	+1.7
T_a [K]	250	267
Ms [kg/m^2]	0.0	46.6
Δh_{snow} [cm]	-0.1	+24.5

Period	-1	1-2	2-
ΔP_{e89}	↘	↗	↗
$\Delta \rho_{snow}$	↗	↗	↗
$\Delta \bar{\rho}_{snow}$	↗	↗	↗
Δh_{snow}	↘	↘	↘

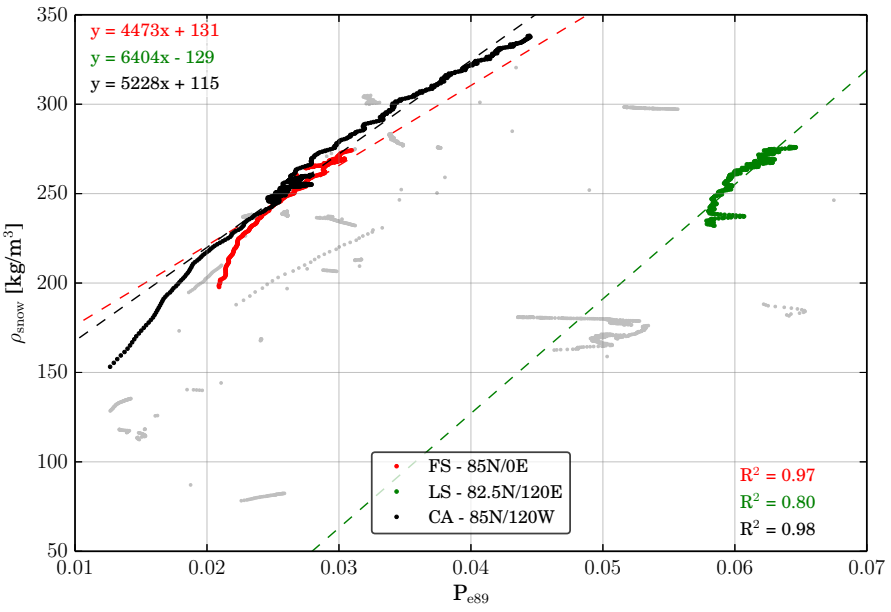

Figure 5.5: Sensitivity of P_{e89} to surface snow density ρ_{snow} for the three locations in the Arctic as defined in Figure 5.2. The correlation between the data and a linear least-squares regression line are shown color-coded for the three locations. Gray dots indicate the data outside the investigated periods and are not considered in the regression. The equations of the individual regression lines are shown in the upper left corner in the figure; the coefficients of determination are given in the lower right corner.

Table 5.6: Sensitivity of P_{e89} to surface snow density ρ_{snow} for the three locations according to the regressions calculated in Figure 5.5). The sensitivity is estimated as the inverse of the slope of the regression. Note that the uncertainties in the regressions are two magnitudes lower than the estimate from the regression. The uncertainty in the MYI mean response are estimated from averaging estimates at locations CA and FS.

Location	regression line	$\Delta P_{e89}/\Delta\rho_{snow}$
CA	$y = 5.2 \times 10^3 x + 115$	$(1.9 \pm 0.0)10^{-2}\,\mathrm{m^3/kg}$
FS	$y = 4.5 \times 10^3 x + 131$	$(2.2 \pm 0.0)10^{-2}\,\mathrm{m^3/kg}$
		$(2.1 \pm 0.2)10^{-2}\,\mathrm{m^3/kg}$
LS	$y = 6.4 \times 10^3 x - 129$	$(1.6 \pm 0.0)10^{-2}\,\mathrm{m^3/kg}$

We derive a sensitivity of P_{e89} to changes in ρ_{snow} by calculating a linear least-squares regression for the data points from the investigated periods, in which we find accordant and considerable changes in P_{e89} and ρ_{snow} as shown in the previous sections (Figure 5.5). We use the surface snow density changes as a proxy for microphysical changes in the snow due to fall events and snow metamorphism from aging. Coefficients of determination R^2 for these periods are around 0.97 for the two MYI locations and p-values are 0, indicating statistical significance (not shown). The regression for the FYI location LS shows a similar slope, however, the regression's R^2 is 0.80. We regard this regression as less meaningful than for the MYI locations and consider it a separate case for two reasons: first, the period at LS does not start with a fresh snow cover (event 1 for LS), and second, the period shows only a small increase in P_{e89} with superposed short-term variability in the polarization difference that stems from stronger signals in the h-polarized emissivity at 89 GHz than in the v-polarized emissivity at 89 GHz (not shown). However, the relation that an increase in ρ_{snow} increases P_{e89} is also confirmed for this period.

Based on these regressions, we calculate the sensitivity of P_{e89} to surface snow density changes $\Delta P_{e89}/\Delta\rho_{snow}$ separately for each location and calculate the average response for MYI (Table 5.6). The mean sensitivity of the emissivity polarization difference P_{e89} to snow density changes and its standard deviation are $\Delta P_{e89}/\Delta\rho_{snow} = (2.1 \pm 0.2)\,10^{-4}\,\mathrm{m^3/kg}$ for MYI and $\Delta P_{e89}/\Delta\rho_{snow} = 1.6\,10^{-4}\,\mathrm{m^3/kg}$ for FYI. With equation 2.2 and using the simulated mean effective temperature at 89 GHz, $\bar{T}_{eff,89}$, for each location and the periods used in the regression, we estimate the sensitivity of brightness temperature polarization difference at 89 GHz to surface snow density changes (Table 5.7).

The mean sensitivity of the brightness temperature polarization difference at 89 GHz to surface snow density changes for locations CA and FS gives a change of ∼2.6 K if the change in surface snow density is 50 $\mathrm{kg/m^3}$. For the FYI location LS, we estimate a sensitivity of ∼2.2 K if the change in surface snow density is 50 $\mathrm{kg/m^3}$. Note that typical changes in in surface snow density range between 30 $\mathrm{km/m^3}$ and

Table 5.7: List of mean effective temperature at 89 GHz $\bar{T}_{eff,89}$ and its standard deviation (middle column) for the data points at each location that are considered in Figure 5.5. $\bar{T}_{eff,89}$ is used to estimate the brightness temperatures polarization difference at 89 GHz to surface snow density (right column).

Location	$\bar{T}_{eff,89} \pm \sigma_{\bar{T},eff89}$	$\Delta P_{89}/\Delta\rho_{snow}$
CA	250.0 ± 9.2	$(4.8 \pm 0.2)10^{-2}\,K\,m^3/kg$
FS	256.6 ± 8.9	$(5.7 \pm 0.2)10^{-2}\,K\,m^3/kg$
		$(5.2 \pm 0.3)10^{-2}\,K\,m^3/kg$
LS	268.6 ± 1.6	$(4.3 \pm 0.0)10^{-2}\,K\,m^3/kg$

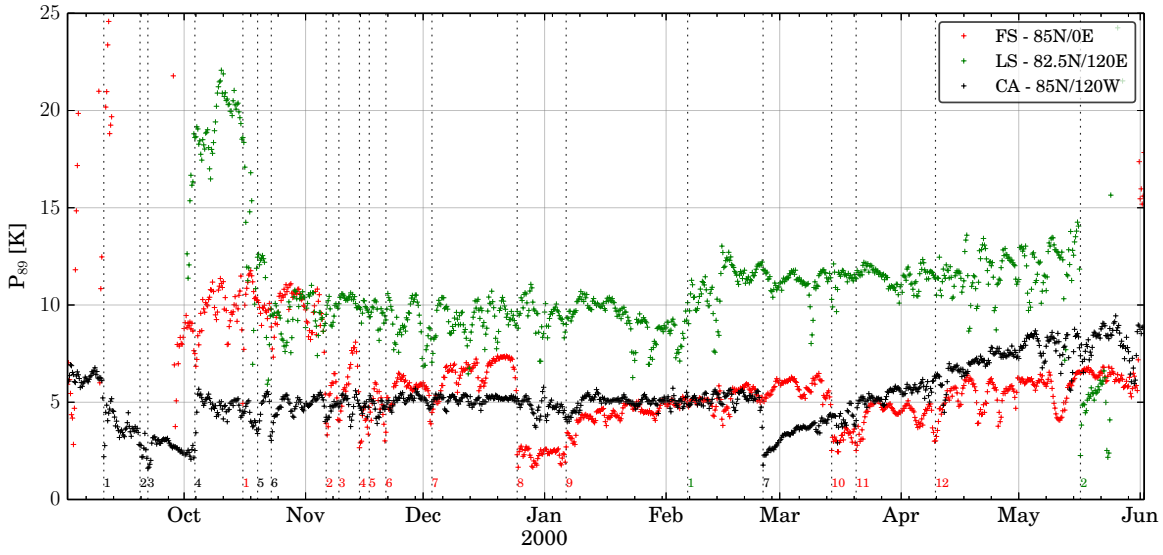

Figure 5.6: Time series of the polarization difference of brightness temperatures at 89 GHz P_{89} from MEMLSI for the three locations in the Arctic as defined in Figure 5.2.

100 km/m^3 (Figure 5.3). We have considered the FYI and MYI locations separately. However, the similarity of the sensitivities for both ice types seems very close if not indistinguishable. However, we suggest to regard the to sensitivities separately for two reasons. First, the FYI location LS shows P_{e89} values considerably higher than for the MYI locations (Figure 5.5). And second, the snow cover at the FYI location LS is considerably lower than for the MYI locations, possibly having an influence on P_{e89} from the underlying ice.

5.3 Atmospheric Influence on Emission Variability

Variations in brightness temperature polarization difference P_{89} (Figure 5.6) can be linked to the atmospheric parameters integrated water vapour IWP, liquid water path LWP, and air temperature T_a (Oelke, 1997; Andersen et al., 2007). These parameters

Table 5.8: Sensitivity of P_{89} to the liquid water path in the atmosphere LWP for the three locations according to the regressions calculated in Figures 5.7-5.9 and summarized in Figure 5.10. The sensitivity is estimated as the inverse of the slope of the regression; the uncertainty of the inverse is estimated from the error of the regression (not shown). Note that we only show two number of digits after the decimal point, but we calculate the sensitivity with all digits calculated in the regression. An explanation why we calculate separate sensitivities for FYI and MYI locations is given in the text.

Location	regression line	$\Delta P_{89}/\Delta$LWP
CA	$y = -0.07x + 0.37$	$-(18.9 \pm 1.5)\,\mathrm{K\,m^2/\,kg}$
FS	$y = -0.05x + 0.32$	$-(17.2 \pm 1.7)\,\mathrm{K\,m^2/\,kg}$
		$-(18.1 \pm 2.3)\,\mathrm{K\,m^2/\,kg}$
LS	$y = -0.03x + 0.37$	$-(29.0 \pm 3.6)\,\mathrm{K\,m^2/\,kg}$

affect sea ice concentration retrievals by increased atmospheric emission and absorption of the microwave radiation or changes imposed on the surface emissivity due to the influence of physical temperature at the surface. Especially at 89 GHz, atmospheric opacity is increased in comparison with 19 or 37 GHz (Lubin et al., 1997)—the frequencies that are used for most other sea ice concentration retrieval algorithms (see Chapter 3). Therefore, frequencies at 89 GHz are sensitive to increased amounts of water vapour and cloud liquid water in the atmospheric column (Oelke, 1997, and Section 2.2.1). By using brightness temperature polarization differences, the effect of surface temperature variations on retrieving ice concentrations is reduced (Cavalieri et al., 1984). However, an influence of the surface temperature on brightness temperatures and, thus, on the polarization difference exists and has not yet been quantified for P_{89} and in the ASI algorithm. We investigate the sensitivity of brightness temperature polarization difference P_{89} to integrated water vapour IWP, liquid water path LWP, and air temperature T_a.

We examine periods with approximately constant surface conditions, i.e., $\sigma_{\bar{P}_{e89}} \approx 0$, and a considerable increase in one of the atmospheric parameters LWP, IWP, and T_a in a short period of about a few days (Table A.1 for LWP, Table A.2 for IWP, and Table A.3 for T_a). For these periods, we assume variability in P_{89} to be induced by atmospheric parameters that interact with microwave radiation at 89 GHz. For the individual periods, we calculate the regression to quantify the sensitivity of P_{89} to one of the atmospheric parameters. Based on multiple regressions at each location and for each parameter, we calculate a mean sensitivity at each location and for each parameter weighted by the coefficients of determination R^2, which are calculated from the individual regressions.

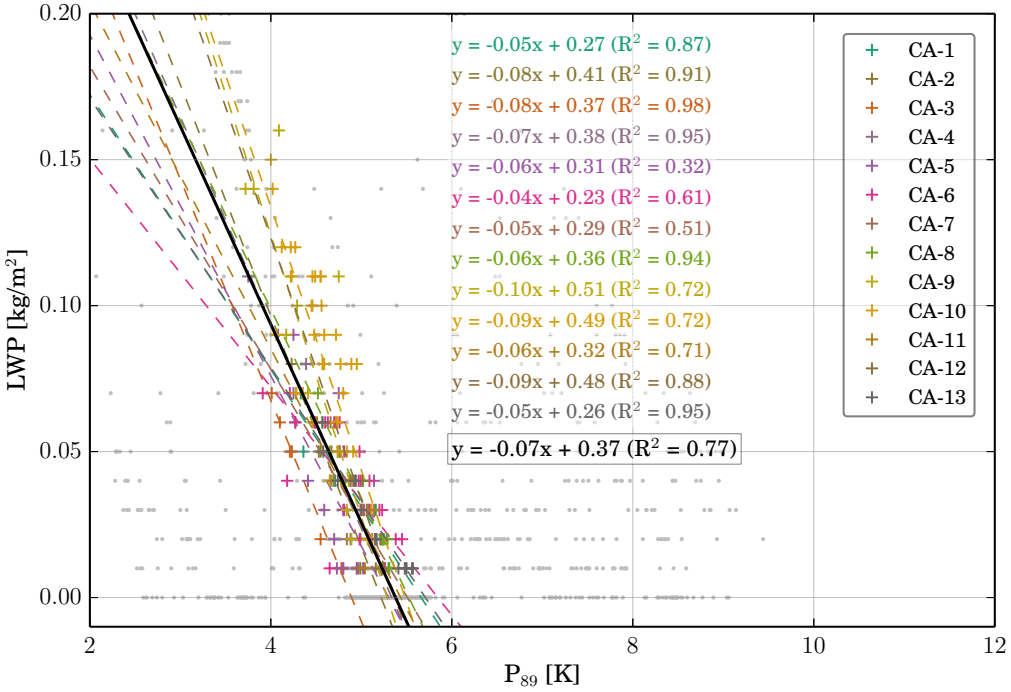

Figure 5.7: Sensitivity of P_{89} on liquid water path in the atmosphere LWP for location CA. The equations of the regression lines and coefficients of determination are shown color-coded for the different periods specified in Table A.1. The weighted mean regression is shown color-coded following the previous color-codes for the location CA (and FS and LS in the following Figures). Gray dots indicate the data outside the periods investigated and are not considered in the regression.

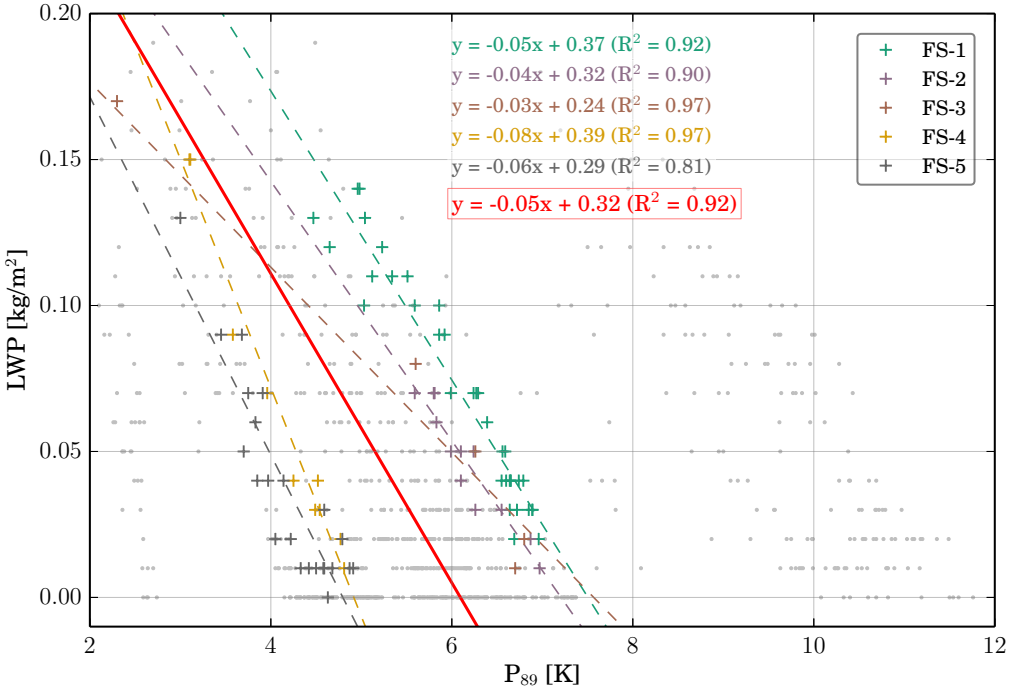

Figure 5.8: Same as Figure 5.7, but for location FS.

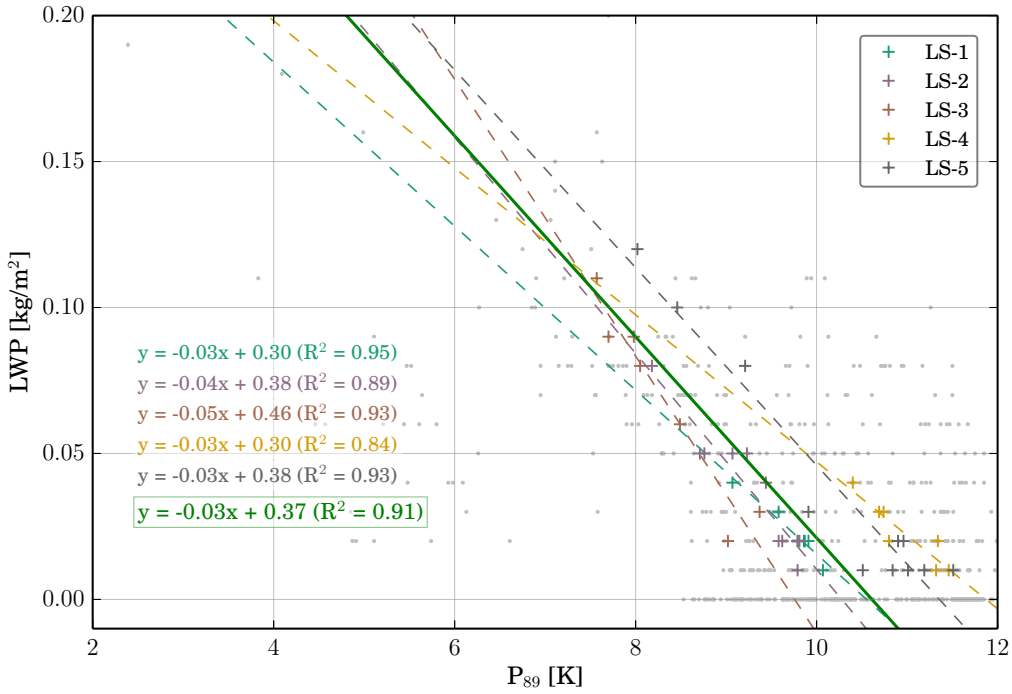

Figure 5.9: Same as Figure 5.7, but for location LS.

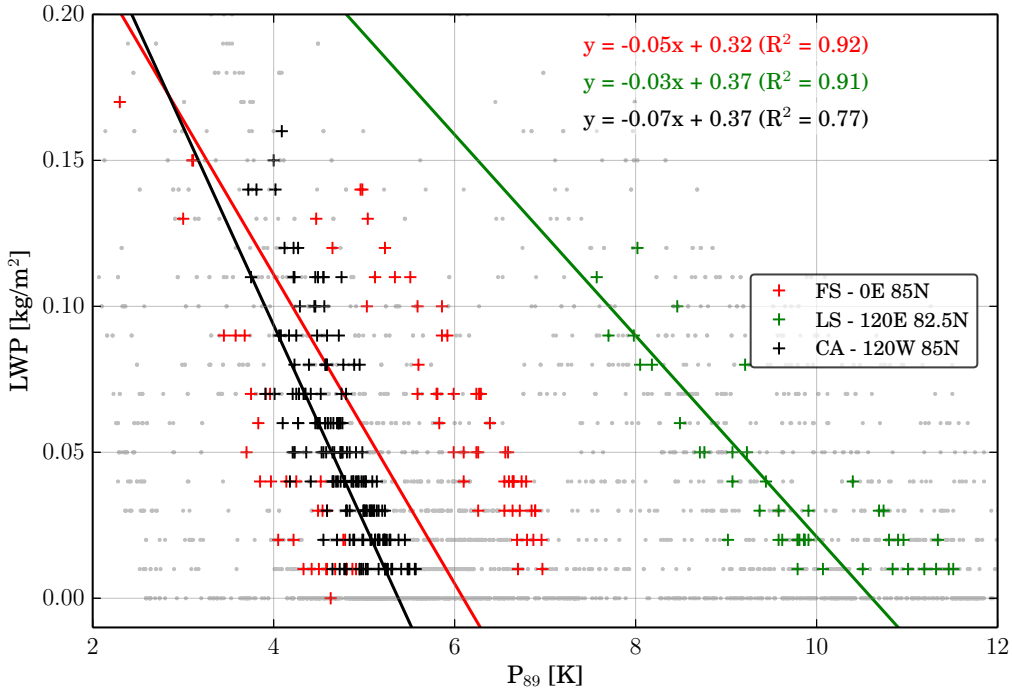

Figure 5.10: Summary of Figures 5.7-5.9: sensitivity of P_{89} to liquid water path in the atmosphere LWP for the three locations. Mean regression lines and mean coefficients of determination are shown color-coded for the three locations. Gray dots indicate the data outside the periods investigated and are not considered in the regression.

5.3.1 Liquid Water Path

The regressions in Figures 5.7-5.9 are based on periods with a considerable increase in LWP during approximately constant surface conditions (see Table A.1). We find most of such periods at the MYI location in the Central Arctic with maximum values of 0.16 kg/m^2 for LWP. Similarly high values for LWP but a smaller number of periods are investigated at location FS. At location LS, the highest values for LWP can be found in November (Table A.1). At location CA, there is a considerable spread among the individual regression lines (Figure 5.7); slopes of the individual regressions are shallowest in fall and steepest in spring. Exceptions to this tendency are the periods CA-5, CA-6, CA-7, CA-10, CA-11, and CA-13; these exhibit a lower coefficient of determination and a smaller range of values in LWP. For locations FS and LS—the locations with fewer periods of investigation—, there is generally less spread among the individual regression lines and high coefficients of determination (Figure 5.8 and Figure 5.9). A summary for the mean regression of the three locations is shown in Figure 5.10 and subsequently derived sensitivities are given in Table 5.8. For the MYI locations, which have smaller polarization differences than the FYI location LS, there is a tendency to be less sensitive to changes in LWP, simply because there is not much more potential for further depolarization at 89 GHz.

Considering a typical change of 0.1 kg/ m^2 for LWP (Fuhrhop et al., 1998, and Table A.1), the mean sensitivity of the brightness temperature polarization difference at 89 GHz to the liquid water path in the atmosphere for locations CA and FS indicates a decrease of ∼1.8 K for an increase in liquid water path of 0.1 kg/ m^2 (Table 5.8). For the FYI location in the Laptev Sea, we estimate a decrease of ∼2.9 K if the liquid water path increases by 0.1 kg/ m^2.

5.3.2 Integrated Water Vapour

Similarly to the investigation of the sensitivity of P_{89} to LWP, we examine the sensitivity of the brightness temperature polarization difference at 89 GHz to integrated water vapour in the atmosphere IWP. The regressions in Figures 5.11-5.13 are based on periods with a considerable increase in IWP during approximately constant surface conditions (see Table A.2). Again, most of such periods can be found at the MYI location CA with maximum values of ∼5.9 kg/m^2 for IWP during winter. The maximum values for IWP at locations FS and LS do not exceed ∼4.3 kg/m^2 and ∼4.0 kg/m^2 during winter, respectively. The spread in regression lines is again largest at location CA with one regression showing a positive slope, contrasting the other periods at this locations with negative slopes in the regression. At locations FS and LS, the slopes of all regressions are negative. In general, most regressions have a low coefficient of determination and results for the sensitivity must be considered with care. A summary for the mean regression of the three locations is shown in Figure 5.14 and subsequently derived sensitivities are given in Table 5.9. Like for LWP, we find the same tendency

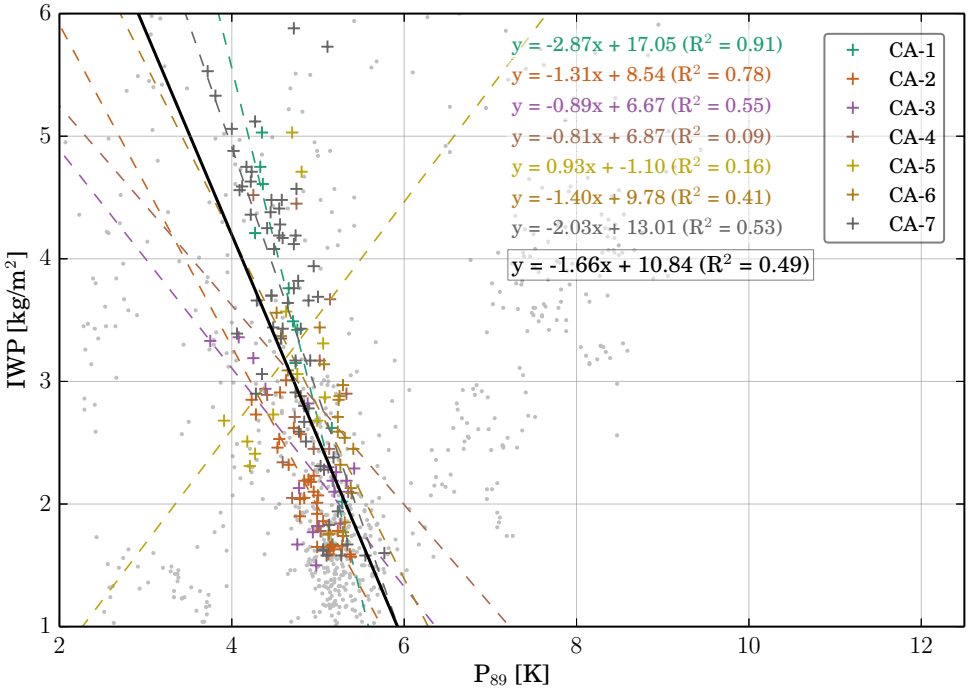

Figure 5.11: Sensitivity of P_{89} on integrated water vapour in the atmosphere IWP for location CA. The equations of the regression lines and coefficients of determination are shown color-coded for the different periods specified in Table A.2. Gray dots indicate the data outside the periods investigated and are not considered in the regression.

that at MYI locations the polarization difference is less sensitive to changes in LWP, because of the missing potential for further depolarization at 89 GHz.

The mean sensitivity of the brightness temperature polarization difference at 89 GHz to integrated water vapour in the atmosphere for locations CA and FS indicates a decrease of ∼0.9 K for a typical increase in the integrated water vapour of 1.0 kg/ m^2 (see Table 5.9). For the FYI location in the Laptev Sea, we estimate a decrease of ∼2.3 K if the integrated water vapour increases by 1.0 kg/ m^2. Low coefficients of determination for the individual and the location-averaged regressions indicate a substantial uncertainty in these estimates. Additionally, the difference between both MYI locations is large in this case.

5.3.3 2 m Air Temperature

Finally, we investigate the sensitivity of P_{89} on changes in 2 m air temperatures T_a. The use of P_{89} for sea ice concentration retrieval algorithms is supposed to reduce the effect of physical temperature on measured brightness temperatures. But the sensitivity of the H- and V-polarizations can be different, leaving a temperature imprint on the brightness temperature polarization difference. The regressions P_{89} to T_a shown in Figures 5.15-5.17 are based on periods with a minimum increase in T_a of 3.5 K dur-

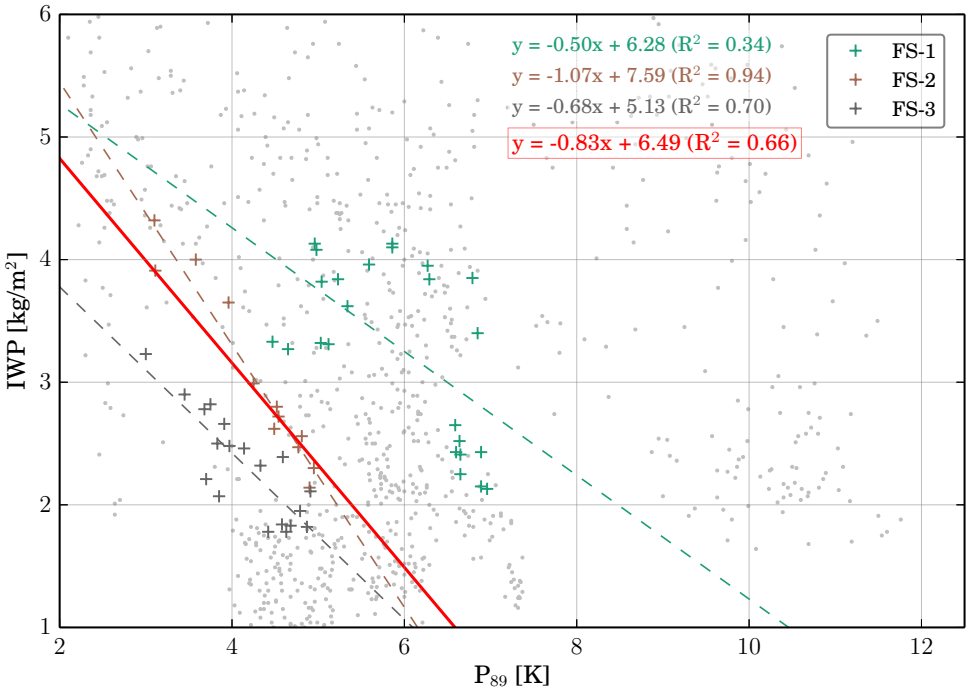

Figure 5.12: Same as Figure 5.11, but for location FS.

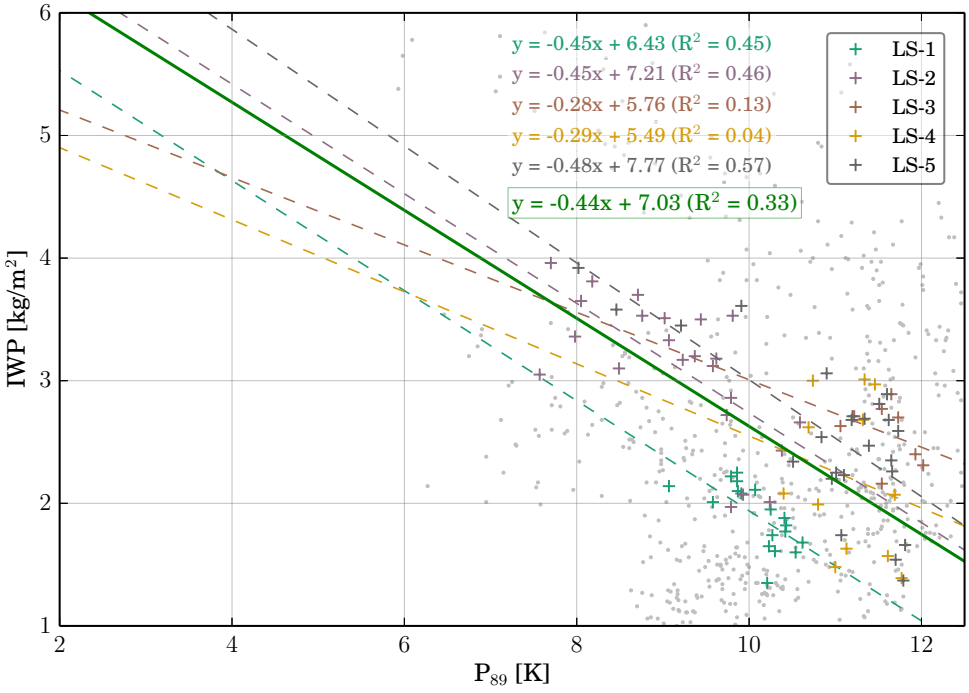

Figure 5.13: Same as Figure 5.11, but for location LS.

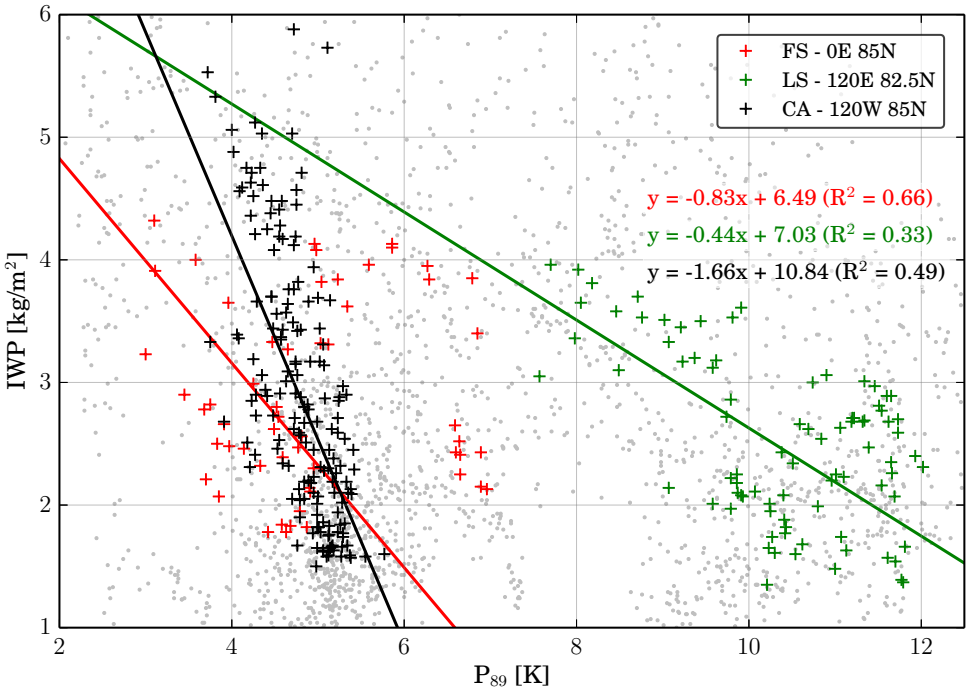

Figure 5.14: Summary of Figures 5.11-5.13: sensitivity of P_{89} to integrated water vapour in the atmosphere IWP for all locations. Mean regression lines and mean coefficients of determination are shown color-coded for the three locations. Gray dots indicate the data outside the periods investigated and are not considered in the regression.

Table 5.9: Sensitivity of P_{89} to integrated water vapour in the atmosphere IWP for the three locations according to the regressions calculated in Figures 5.11-5.13 and summarized in Figure 5.14). The sensitivity is estimated as the inverse of the slope of the regression; the uncertainty of the inverse is estimated from the error of the regression (not shown). Due to the differences in the regressions among the three locations, we expect different sensitivities for FYI and MYI surfaces, and, hence, we calculate a mean sensitivity for the MYI location, CA and FS.

Location	regression line	$\Delta P_{89}/\Delta$IWP
CA	$y = -1.66x + 10.84$	$-(0.6 \pm 0.1)\,\mathrm{K\,m^2/\,kg}$
FS	$y = -0.83x + 7.03$	$-(1.2 \pm 0.2)\,\mathrm{K\,m^2/\,kg}$
		$-(0.9 \pm 0.2)\,\mathrm{K\,m^2/\,kg}$
LS	$y = -0.44x + 7.03$	$-(2.3 \pm 0.7)\,\mathrm{K\,m^2/\,kg}$

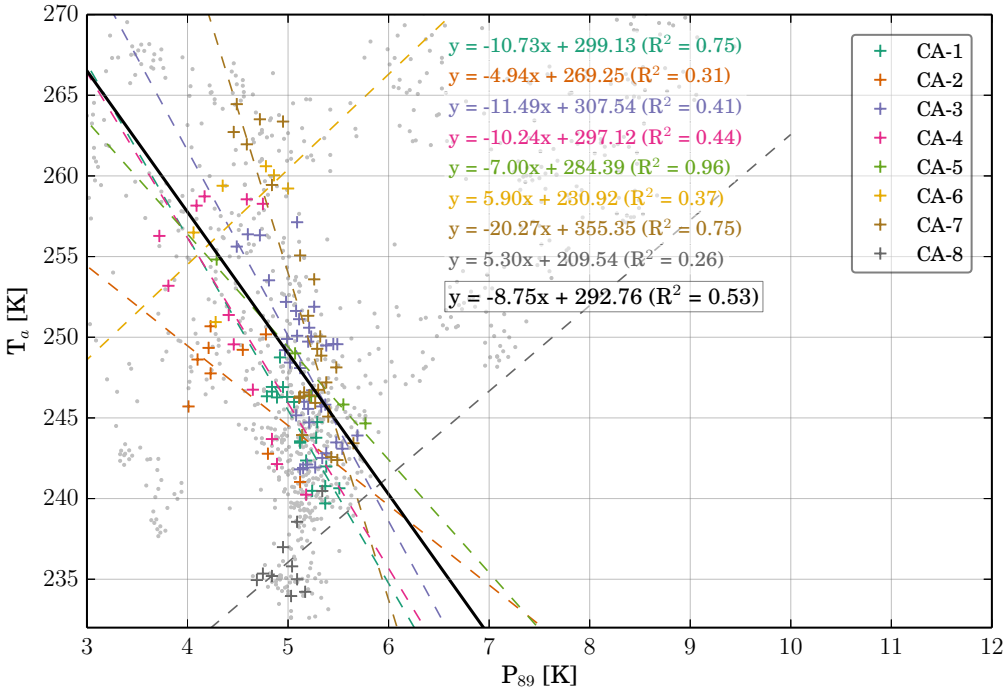

Figure 5.15: Sensitivity of P_{89} on air temperature T_a for location CA. The equations of the regression lines and coefficients of determination are shown color-coded for the different periods specified in Table A.3. Gray dots indicate the data outside the periods investigated and are not considered in the regression.

ing approximately constant surface conditions (see Table A.3). The location-averaged regressions are summarized in Figure 5.18. The coefficients of determination indicate higher confidence than in the sensitivity analysis for IWP. However, the spread among the different regressions for same locations is very large, especially at location LS (Figure 5.17). This suggests a more complex relationship between P_{89} and T_a. Some regression lines indicate increasing P_{89} with increasing T_a, but most of the regression lines indicate decreasing P_{89} with increasing T_a. However, the positively correlated periods show a lower R^2 and, therefore, have a lower significance.

At locations CA and FS, the data point cluster shows more coherency than the data point cluster for the location LS. And also due to the low significance at location LS, we only derive a temperature sensitivity for the two MYI locations (Table 5.10). The mean sensitivity of the brightness temperature polarization difference at 89 GHz to air temperature for locations CA and FS indicates a decrease of ∼1.1 K for a typical increase in the air temperature of 10 K (see Table 5.10). Like for IWP, low coefficients of determination for the individual and the location-averaged regressions indicate a substantial uncertainty in these estimates.

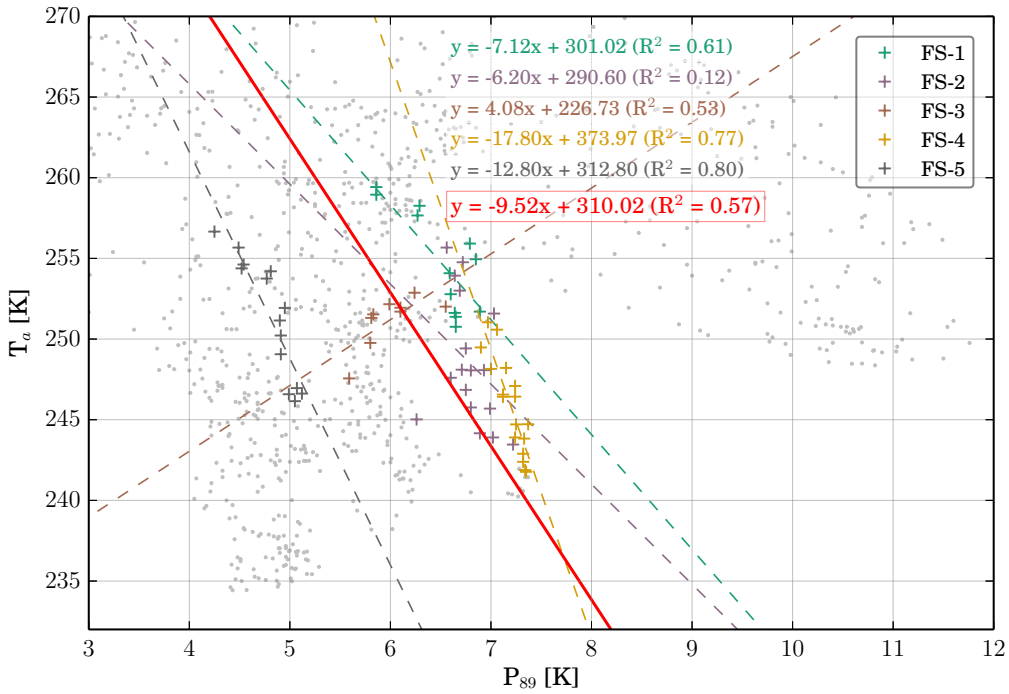

Figure 5.16: Same as Figure 5.15, but for location FS.

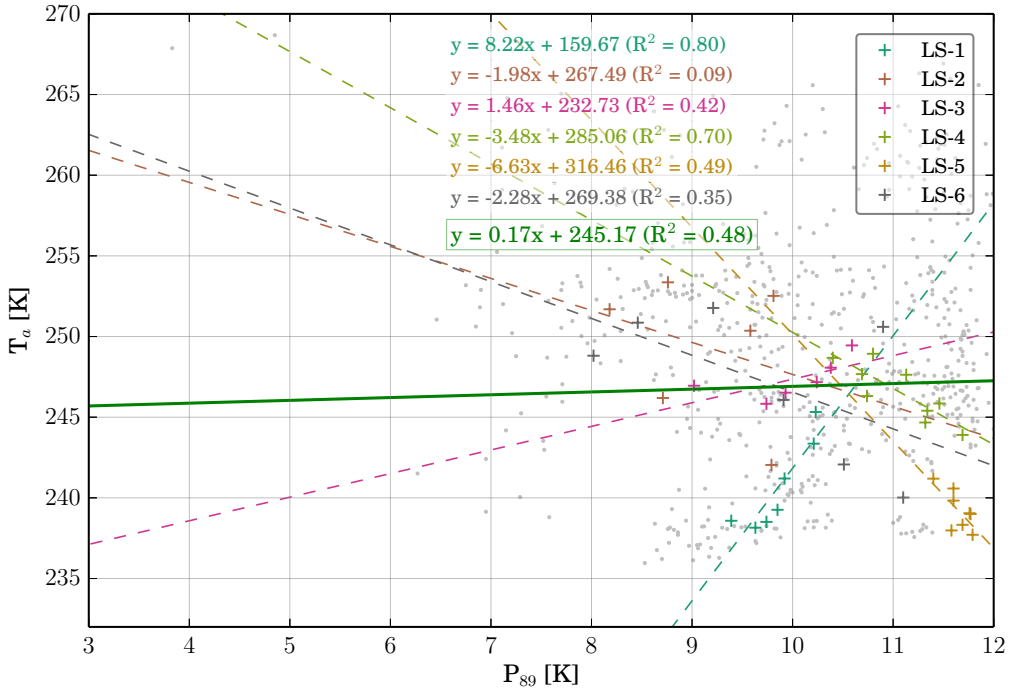

Figure 5.17: Same as Figure 5.15, but for location LS.

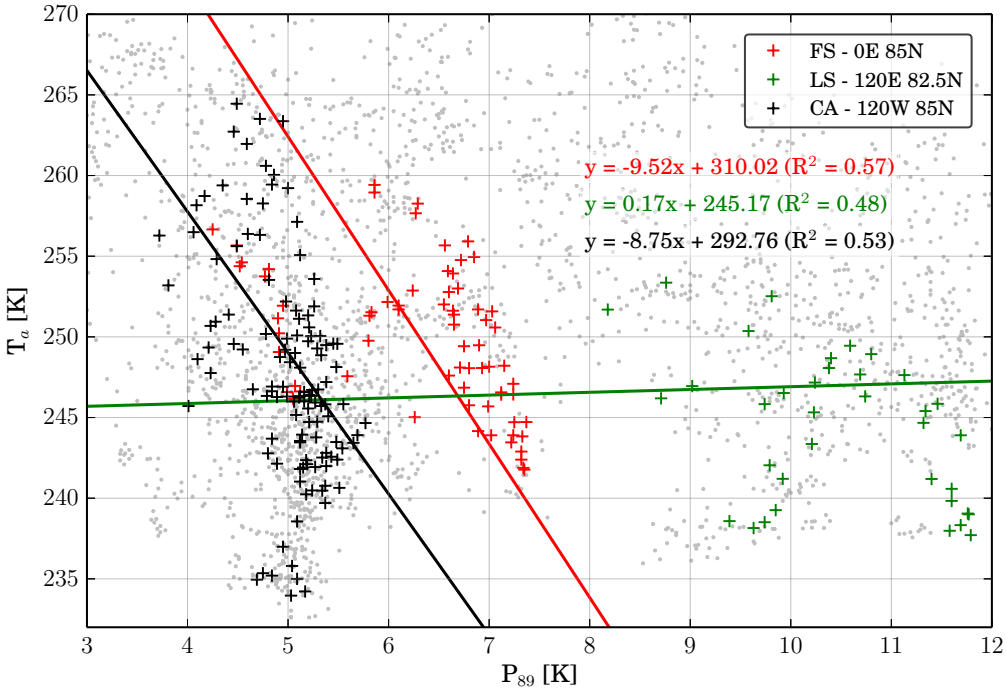

Figure 5.18: Summary of investigating the sensitivity of P_{89} on air temperature T_a for all locations. Mean regression lines and mean coefficients of determination are shown color-coded for the three locations. Gray dots indicate the data outside the periods investigated and are not considered in the regression.

Table 5.10: Sensitivity of P_{89} to air temperature T_a for the two MYI locations according to the regressions in Figure 5.18). The sensitivity is estimated as the inverse of the slope of the regression; the uncertainty of the inverse is estimated from the error of the regression (not shown).

Location	regression line	$\Delta P_{89}/\Delta T_a$
CA	$y = -8.75x + 292.76$	$-(0.11 \pm 0.03)$ K/ K
FS	$y = -9.52x + 310.02$	$-(0.11 \pm 0.02)$ K/ K
		$-(0.11 \pm 0.04)$ K/ K

Table 5.11: Summary of sensitivities of the brightness temperature polarization difference at 89 GHz P_{89} to surface snow density ρ_{snow} and the weather-related parameters cloud liquid water path LWP and integrated water vapour IWP for FYI and MYI locations, and (2 m) air temperature T_a for a FYI location derived from simulated data with the combined thermodynamic and emissivity model MEMLSI.

	$\Delta P_{89}/\Delta\rho_{\text{snow}}$	ΔP_{89} for $\Delta\rho_{\text{snow}} = 50\,\text{kg/m}^3$
FYI	$(4.30 \pm 0.03)10^{-2}\,\text{K m}^3/\text{kg}$	2.2 K
MYI	$(5.20 \pm 0.27)10^{-2}\,\text{K m}^3/\text{kg}$	2.6 K
	$\Delta P_{89}/\Delta\text{LWP}$	ΔP_{89} for $\Delta\,\text{LWP} = 0.1\,\text{kg/m}^2$
FYI	$-(29.4 \pm 3.6)\,\text{K m}^2/\text{kg}$	-2.9 K
MYI	$-(18.1 \pm 2.3)\,\text{K m}^2/\text{kg}$	-1.8 K
	$\Delta P_{89}/\Delta\text{IWP}$	ΔP_{89} for $\Delta\,\text{IWP} = 1.0\,\text{kg/m}^2$
FYI	$-(2.3 \pm 0.7)\,\text{K m}^2/\text{kg}$	-2.3 K
MYI	$-(0.9 \pm 0.2)\,\text{K m}^2/\text{kg}$	-0.9 K
	$\Delta P_{89}/\Delta T_a$	ΔP_{89} for $\Delta T_a = 10\,\text{K}$
MYI	$-(0.11 \pm 0.04)\,\text{K/K}$	-1.1 K

5.4 Discussion and Conclusion

We investigated the influence of the surface snow density ρ_{snow} and the weather-related parameters cloud liquid water path LWP, integrated water vapour IWP, and air temperature T_a, on the brightness temperature polarization difference P_{89}. Our investigation serves as another step towards an improved error estimation of a near-90 GHz sea ice concentration retrieval during winter. The link between changes in one physical parameter at the surface or in the atmosphere and uncertainties in sea ice concentrations has been investigated in several studies (Oelke, 1997; Fuhrhop et al., 1998; Kern, 2004). We use the combined thermodynamic and emission model MEMLSI to investigate the impact of changing surface and atmospheric parameters on brightness temperatures at 89 GHz.

The sensitivities of P_{89} to ρ_{snow}, LWP, IWP, and T_a are summarized in Table 5.11. We find different sensitivities for FYI and MYI locations. MYI locations show higher sensitivities for snow fall events. Clouds and water vapour depolarize the radiation at 89 GHz almost twice as large for a FYI cover. Due to the low significance of the regressions, we cannot determine a temperature sensitivity at FYI locations. We note that, based on the RRDP simulations, we are not able to investigate isolated conditions, for example the impact of increased water vapour on the brightness temperature polarization difference alone. Periods of considerably increased values for IWP and

LWP are partly identical, for example periods FS-4 and FS-5 for LWP (Table A.1) and periods FS-2 and FS-3 for IWP (Table A.2), and there may exist a coupling of the sensitivities for LWP and IWP. Considering other filters for a selection of periods does not necessarily lead to better results. Using a minimum range of 10 K for the selection of periods to investigate sensitivities of P_{89} to T_a or using a maximum length of 3 days, would exclude periods—depending on the location—for which we found higher coefficients of determinations. This would eventually decrease the significance of our results. As a next step, one should investigate periods with no coupling in the investigated parameters to exclude covariances in the sensitivities.

We use the sensitivities derived from simulations with the combined thermodynamic snow/ice and emissivity model to enhance the error estimation of ASI SIC carried out by Spreen et al. (2008), which is expressed in terms of the standard deviation of the polarization difference at 89 GHz in Spreen et al. (2008), as has been introduced in Section 2.2.1 (Eq. 2.14).

Variations in LWP and IWP are linked to variations in the opacity of the atmosphere over sea ice $\sigma_{\tau,\mathrm{i}}$. However, as we are not able to derive the opacity as a function of the ice concentration, we treat the derived sensitivities to LWP and IWP as direct influences on TB over sea ice and, hence, on the ice tie-point $P_{\mathrm{s,i}}$. Therefore, we change the standard deviation of the ice tie-point $P_{\mathrm{s,i}}$ in Equation 2.14. The significance in the sensitivity of P_{89} on T_{a} was considerably lower than for the other parameters, and we were not able to derive a sensitivity over FYI. Therefore, we only consider the sensitivities derived for ρ_{snow}, IWP, and LWP. Because of potential coupling between the sensitivities of P_{89} to IWP and P_{89} to LWP, we estimate a mean sensitivity to both parameters, expressed as the standard deviation in SIC caused by atmospheric water $\sigma_{\mathrm{H_2O}}$. We treat the sensitivities to the snow and to atmospheric water as independent factors that contribute to the function that defines the standard deviation of the ice tie-point, i.e., $\sigma_{\mathrm{P_{s,i}}} = f(\rho_{\mathrm{snow}}, \{\mathrm{LWP}, \mathrm{IWP}\}) = f(\rho_{\mathrm{snow}}, \{\mathrm{atm.water}\})$, and we change the standard deviation in the last term of the error estimation for P_{89} (see Section 2.2.1, Equation 2.13) according to the derived sensitivities:

$$\sigma_{\mathrm{P_{s,i}}} = \sqrt{\sigma^2_{\rho_{\mathrm{snow}}} + \sigma^2_{\mathrm{atm.water}}} = \sqrt{\sigma^2_{\rho_{\mathrm{snow}}} + \frac{\sigma^2_{\mathrm{LWP}} + \sigma^2_{\mathrm{IWP}}}{2}} \tag{5.1}$$

where we use the sensitivities derived for ρ_{snow}, IWP, and LWP as typical standard deviations of these parameters. Then, we use Equation 2.14 to derive a new SIC uncertainty.

For the situation at the end of April 2014, which we presented in Section 5.1, maps of the uncertainty estimate confirm a higher uncertainty for the region influenced by a new snow layer and higher LWP and IWP (Figure 5.19). Highest uncertainties are located in an area between the Central Arctic and the East Siberian Sea. Uncertainties are largest on 29 April and decay during the following days. A pattern of uncertainties with values around 6 % moves from the eastern Arctic to the western Arctic. While the

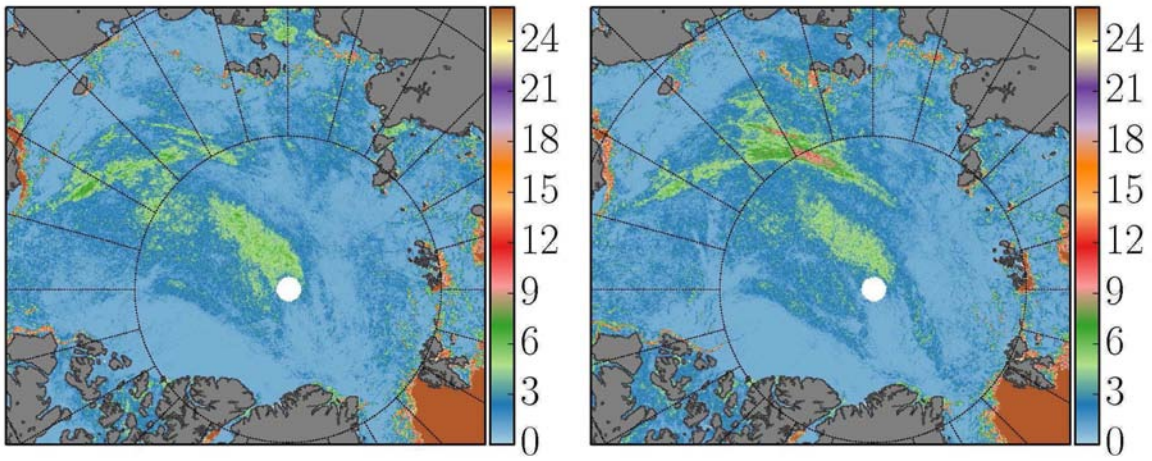

(a) 28 April

(b) 29 April

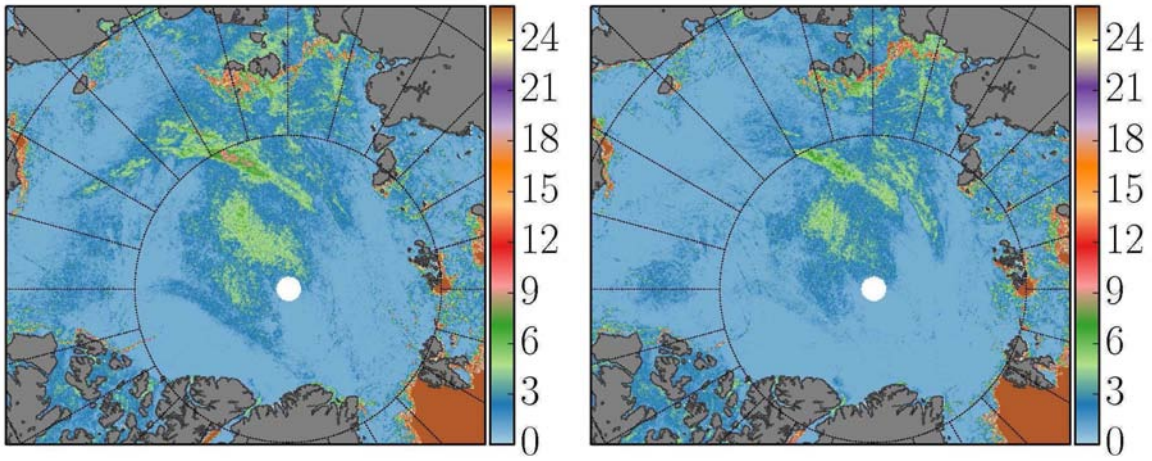

(c) 30 April

(d) 1 May

Figure 5.19: A series of four daily uncertainty estimates for ASI AMSR2 SIC for (a) 28 April, (b) 29 April, (c) 30 April, and (d) 1 May 2014 in the Central Arctic when different processes influence the accuracy of the SIC retrieval. These maps depict the uncertainty for the series of SIC maps displayed in Figure 5.1 assuming all sea ice to be FYI. Note that the uncertainty estimate differs for MYI. Continental areas are displayed in gray.

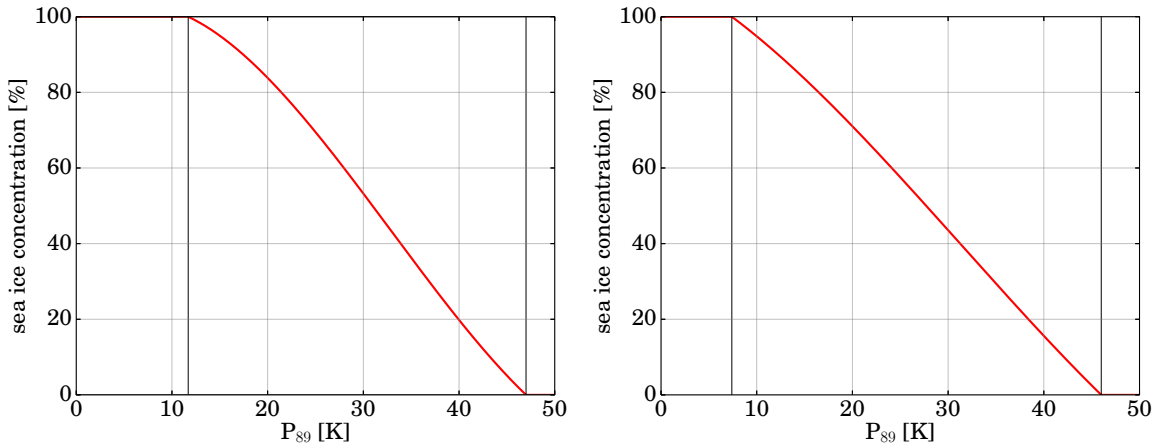

(a) ASI polynomial for TB measured with AMSR-E.

(b) ASI polynomial for TB measured with SSM/I.

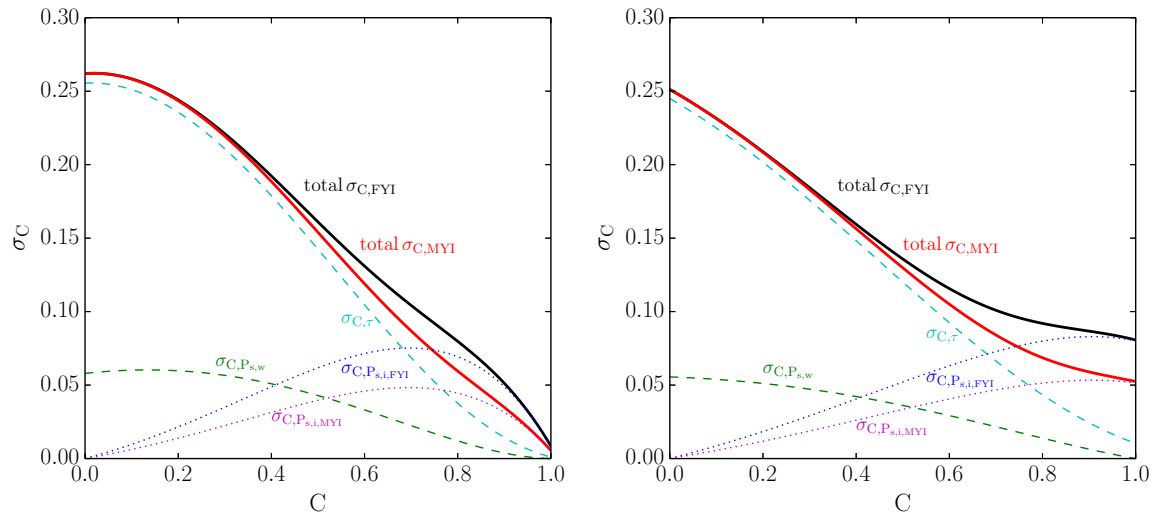

(c) Error estimation using AMSR-E tie-points.

(d) Error estimation using SSM/I tie-points.

Figure 5.20: Comparison of the ASI polynomials (upper panel) and the error estimations for the sea ice fraction C (lower panels) using the tie-points based on measurements for AMSR-E (P_0 =46.0 K and P_1 =7.4 K; Spreen et al., 2008) (left column) and for SSMI (P_0 =47.0 K and P_1 =11.7 K; Kaleschke et al., 2001) (right column). Here, sea ice concentration is shown in fractions of 1. The black and the red curve in the lower panel shows the total expected standard deviation of FYI and MYI, $\sigma_{C,FYI}$ and $\sigma_{C,MYI}$, respectively. The other, not solid curves show the uncertainty contributions of the atmosphere (cyan long-dashed line, $\sigma_{C,\tau}$), and of the surface polarization differences of open water (green long-dotted line, $\sigma_{P_{s,w}}$) and sea ice (blue long-dashed line, shown separately for FYI and MYI, $\sigma_{P_{s,i,FYI}}$ and $\sigma_{P_{s,i,FYI}}$, respectively).

first uncertainty pattern can probably be attributed to snow fall starting on 28 April (not shown), the latter indicates that atmospheric parameters increase the uncertainty in the SIC retrieval probably due to a traveling cloud system with increased LWP and IWP.

Uncertainties of up to 5 % for different SIC retrieval algorithms including ASI have been found during winter when the ice cover is in excess of 99 % (Andersen et al., 2007). Spreen et al. (2008) estimate a minimum error of 7 % for ASI based on the input data into the algorithm and the radiometric accuracy of the AMSR-E sensor. The low error of around 1 % where 100 % SIC were detected seems therefore unrealistic.

Considering the polynomials (Figure 5.20(a) using AMSR-E tie-points, Figure 5.20(b) using SSM/I tie-points) that provide SIC for values between the tie-points for open water and for 100 % SIC and the related error estimations (Figure 5.20(c) for AMSR-E, Figure 5.20(d) for SSM/I) following Spreen et al. (2008), we find the error for the AMSR-E-based tie-points to approach values around 1 % when the ice fraction approaches 1 (= 100 % SIC). For values approaching 100 %, the slope in the polynomial—based on P_{89}, $P_{s,w}$, and $P_{s,i}$—reduces and might loose sensitivity for changes in P_{89}. For the set of SSM/I tie-points, the error near 100 % SIC is between 5 % for MYI and 8 % for FYI (Figure 5.20(d)). This is of the order of the minimum error estimated by Spreen et al. (2008). Thus, the choice of the tie-points has a strong influence on the polynomial and on the derived error estimation.

Chapter 6

Summary and Concluding Remarks

In this thesis, we investigated uncertainties in sea ice concentrations (SIC) that are derived from measurements of brightness temperatures using passive-microwave (PM) radiometers. These uncertainties can arise from various sources. Among them are differences in the resolution of the measurements at different frequencies and from different PM radiometers, influences of atmospheric properties on the radiation as it passes the atmospheric column and reaches a radiometer in space, and surface properties, which alter the signature of the emitted radiation.

In a first investigation, we presented a comparison of sea ice concentration (SIC) retrieval algorithms, which are frequently used, with visual ship-based observations of SIC around Antarctica (Chapter 3). We compare correlation coefficients (CC), root-mean-square-deviations (RMSD) and biases, separately for SSM/I-SSMIS data and for AMSR-E data for a number of algorithms. In contrast to previous studies, we apply a different method to compare the co-located ship-based observations of SIC with satellite-based SIC. To account for the different temporal and spatial scales between in-situ observed SIC on a scale on the order of 1 km and those derived with PM sensors on a scale on the order of 10 km. Therefore, we calculate daily along-ship track average SIC. This comparison indicated that the Bootstrap algorithm (BST) provides the highest agreement with in-situ data based on the visual SIC estimates. The higher-resolution ARTIST Sea Ice algorithm (ASI) tended to deviate more from the ship-based observations, but was more successful in representing the local variability in SIC. The differences among the different algorithms agree within the uncertainty range of the CC, the RMSD, and the bias. The agreement between OBS and PM SIC is best during winter.

In a second investigation, we examined the effect of the instrument's resolution on uncertainties in SIC. A new generation of radiometers—the series of Global Change Observation Mission, as part of a series of JAXA's Earth Observation Missions—with reduced sample footprint size allows retrieval algorithms to provide increased spatial resolution of retrieved SIC. One of these radiometers, the Advanced Microwave Scanning Radiometer 2 (AMSR2), enables to compute ASI SIC at 3.125 km grid resolution.

This improved resolution increases the potential to resolve kilometer-scale inhomogeneities within the ice cover, for example larger leads in a previously compact sea ice cover (Chapter 4). We investigated such features in a subsequent analysis. We compared the ability of ASI and BST for representing leads in a highly consolidated ice cover. ASI showed a higher agreement with MODIS images of the same leads than BST. The difference between ASI and BST in a high SIC regime was about 4 % in area-averaged SIC and up to 60 % for single pixels in the lead. With features such as leads being represented more accurately, high-resolution sea ice concentration data have the potential to provide a more realistic boundary condition when calculating atmosphere-ice-ocean exchange processes using these SIC data.

In a third investigation, we showed an assessment of the uncertainties of SIC that are caused by the influence of weather on the sea ice cover and on the snow on top of the sea ice cover (see Chapter 5). For example, snow fall events directly change the surface emissivity. An indirect effect is generated from atmospheric water that influences the signal received at the radiometer in space. Variations of surface properties are the largest error sources during winter. So far, the effect of atmospheric water was thought to be secondary (Andersen et al., 2007). However, a passing cyclone increases the atmospheric water content considerably, and thus, the uncertainty in SIC considerably increases, too. We derived sensitivities for typical changes in surface emissivity, liquid water and water vapour in the atmosphere on changes in SIC. These changes are different for first-year ice (FYI) and multi-year ice (MYI). Variations in the snow surface have more influence on ASI SIC over MYI than over FYI. Over FYI, however, ASI SIC is more sensitive to atmospheric contamination than over MYI. This sensitivity analysis led to estimates of changes in the brightness temperature polarization difference at 89 GHz due to surface snow density changes, variations in liquid water path, integrated water vapour, and surface air temperature, which we used to present an error estimation for ASI SIC. For winter sea ice covers with SIC close to 100 %, we estimate a minimum uncertainty of 7 % for ASI SIC based on the assumptions of the algorithm and the radiometric accuracy of the sensor.

We have shown that the ASI algorithm provides good results of SIC in different hemispheres and based on measurements from different satellite sensors in comparison with in-situ observations and independent data like MODIS. We investigated the sensitivities to surface emissivity changes and atmospheric water vapour in winter using model simulations of sea ice and snow brightness temperatures and emissivities. This investigation led to an enhanced error estimate for ASI. In addition, the choice of the tie-points influences the retrieval of very consolidated ice near 100 % or close to open water. Moreover, the choice of the tie-points has implications for the error estimation, which is very sensitive to the polynomial used in ASI. We suggest to derive a new set of tie-points for AMSR2 measurements separately for both hemispheres. It should be investigated if a polynomial is the best choice to interpolate between values of 100 % SIC and open water.

Appendix

Table A.1: Mean polarization difference of 89-GHz emissivities, $\bar{P}_{e89}$, and its standard deviation, $\sigma_{\bar{P}_{e89}}$, mean polarization difference of 89-GHz brightness temperatures, $\bar{P}_{89}$ (in K), and its standard deviation, $\sigma_{\bar{P}_{89}}$, and minimum and maximum values for liquid water path in the atmosphere, LWP (in kg/m^2), for periods of approximately constant surface conditions ($\sigma_{\bar{P}_{e89}} \approx 0$) and an increase in LWP of at least $>0.03\,kg/m^3$.The periods that are examined at each location are labeled in successive order for identification in Figures 5.7-5.9.

	Period	$\bar{P}_{e89} \pm \sigma_{\bar{P}_{e89}}$	$\bar{P}_{89} \pm \sigma_{\bar{P}_{89}}$	min(LWP)	max(LWP)
CA					
CA-1	1999-10-24–1999-10-26	0.025 ± 0.0	4.76 ± 0.39	0.01	0.07
CA-2	1999-10-27–1999-10-29	0.025 ± 0.0	4.71 ± 0.32	0.01	0.08
CA-3	1999-11-05–1999-11-07	0.025 ± 0.0	4.36 ± 0.31	0.01	0.07
CA-4	1999-11-12–1999-11-13	0.025 ± 0.0	4.48 ± 0.52	0.01	0.11
CA-5	1999-11-14–1999-11-17	0.025 ± 0.0	4.74 ± 0.26	0.01	0.09
CA-6	1999-11-18–1999-11-27	0.026 ± 0.0	4.90 ± 0.37	0.01	0.07
CA-7	1999-12-02–1999-12-04	0.026 ± 0.0	4.91 ± 0.20	0.01	0.05
CA-8	1999-12-05–1999-12-08	0.026 ± 0.0	5.03 ± 0.31	0.01	0.07
CA-9	1999-12-28–1999-12-31	0.027 ± 0.0	4.44 ± 0.41	0.02	0.16
CA-10	2000-01-01–2000-01-10	0.027 ± 0.0	4.59 ± 0.31	0.01	0.15
CA-11	2000-02-01–2000-02-02	0.027 ± 0.0	4.84 ± 0.30	0.01	0.06
CA-12	2000-02-14–2000-02-15	0.027 ± 0.0	4.99 ± 0.14	0.01	0.04
CA-13	2000-02-17–2000-02-20	0.028 ± 0.0	5.14 ± 0.39	0.01	0.06
FS					
FS-1	1999-12-03–1999-12-11	0.035 ± 0.0	6.06 ± 0.75	0.02	0.14
FS-2	1999-12-15–1999-12-17	0.034 ± 0.0	6.18 ± 0.43	0.01	0.07
FS-3	1999-12-24–1999-12-25	0.028 ± 0.0	4.89 ± 2.30	0.01	0.18
FS-4	2000-03-21–2000-03-24	0.024 ± 0.0	4.11 ± 0.65	0.01	0.15
FS-5	2000-04-04–2000-04-09	0.023 ± 0.0	4.19 ± 0.50	0.00	0.13
LS					
LS-1	1999-11-13–1999-11-15	0.049 ± 0.0	9.75 ± 0.31	0.01	0.04
LS-2	1999-11-19–1999-11-21	0.050 ± 0.0	9.27 ± 0.54	0.01	0.08
LS-3	1999-11-23–1999-11-24	0.050 ± 0.0	8.31 ± 0.68	0.02	0.11
LS-4	2000-02-27–2000-02-28	0.059 ± 0.0	10.96 ± 0.41	0.01	0.04
LS-5	2000-03-08–2000-03-11	0.059 ± 0.0	10.23 ± 1.17	0.01	0.12

Table A.2: Same as Table A.1, but for integrated water vapour in the atmosphere IWP (in kg/m^2) and a minimum increase of $>0.7\,kg/m^3$. The periods that are examined at each location are labeled in successive order for identification in Figures 5.11-5.13.

	Period	$\bar{P}_{e89} \pm \sigma_{\bar{P}_{e89}}$	$\bar{P}_{89} \pm \sigma_{\bar{P}_{89}}$	min(IWP)	max(IWP)
CA					
CA-1	1999-10-24–1999-10-26	0.025 ± 0.0	4.71 ± 0.37	1.7	5.0
CA-2	1999-10-27–1999-11-04	0.025 ± 0.0	4.90 ± 0.28	1.6	3.0
CA-3	1999-11-09–1999-11-13	0.025 ± 0.0	4.88 ± 0.47	1.5	3.4
CA-4	1999-11-15–1999-11-18	0.025 ± 0.0	4.83 ± 0.31	1.8	4.5
CA-5	1999-11-19–1999-11-21	0.026 ± 0.0	4.59 ± 0.38	2.3	5.0
CA-6	1999-12-05–1999-12-09	0.026 ± 0.0	5.14 ± 0.27	1.7	3.6
CA-7	1999-12-26–2000-01-10	0.027 ± 0.0	4.66 ± 0.42	1.6	5.9
FS					
FS-1	1999-12-03–1999-12-09	0.035 ± 0.0	5.92 ± 0.83	2.1	4.1
FS-2	2000-03-21–2000-03-24	0.024 ± 0.0	4.25 ± 0.67	2.1	4.3
FS-3	2000-04-05–2000-04-09	0.023 ± 0.0	4.16 ± 0.54	1.8	3.2
LS					
LS-1	1999-11-11–1999-11-16	0.049 ± 0.0	10.09 ± 0.39	1.6	2.3
LS-2	1999-11-19–1999-11-24	0.050 ± 0.0	9.18 ± 0.86	2.0	4.0
LS-3	2000-02-18–2000-02-19	0.058 ± 0.0	11.59 ± 0.33	2.2	2.9
LS-4	2000-02-26–2000-02-29	0.058 ± 0.0	11.16 ± 0.44	1.4	3.0
LS-5	2000-03-08–2000-03-13	0.059 ± 0.0	10.92 ± 1.03	1.4	3.9

Table A.3: Same as Table A.1, but for the air temperature T_a (in K) and a minimum increase of 3.5 K. The periods that are examined at each location are labeled in successive order for identification in Figures 5.15-5.17.

	Period	$\bar{P}_{e89} \pm \sigma_{\bar{P}_{e89}}$	$\bar{P}_{89} \pm \sigma_{\bar{P}_{89}}$	$\min(T_a)$	$\max(T_a)$
CA					
CA-1	1999-11-01–1999-11-05	0.025 ± 0.0	5.10 ± 0.22	239.7	248.8
CA-2	1999-11-05–1999-11-07	0.025 ± 0.0	4.45 ± 0.38	241.0	250.7
CA-3	1999-11-22–1999-12-01	0.026 ± 0.0	5.17 ± 0.25	241.8	257.1
CA-4	1999-12-28–1999-12-30	0.027 ± 0.0	4.46 ± 0.44	240.2	258.7
CA-5	1999-12-31–2000-01-01	0.027 ± 0.0	5.18 ± 0.57	244.7	254.8
CA-6	2000-01-01–2000-01-02	0.027 ± 0.0	4.55 ± 0.38	250.9	260.6
CA-7	2000-01-09–2000-01-15	0.027 ± 0.0	5.15 ± 0.31	242.4	264.4
CA-8	2000-02-03–2000-02-05	0.027 ± 0.0	5.00 ± 0.20	234.0	240.5
FS					
FS-1	1999-12-05–1999-12-08	0.035 ± 0.0	6.50 ± 0.35	250.8	259.4
FS-2	1999-12-11–1999-12-15	0.034 ± 0.0	6.79 ± 0.22	243.5	255.7
FS-3	1999-12-15–1999-12-17	0.034 ± 0.0	6.00 ± 0.29	247.6	252.9
FS-4	1999-12-17–1999-12-21	0.034 ± 0.0	7.20 ± 0.15	241.8	251.0
FS-5	2000-03-22–2000-03-26	0.023 ± 0.0	4.81 ± 0.26	246.2	256.7
LS					
LS-1	1999-11-15–1999-11-17	0.049 ± 0.0	9.85 ± 0.30	238.2	245.3
LS-2	1999-11-19–1999-11-20	0.049 ± 0.0	9.14 ± 0.68	242.0	253.4
LS-3	1999-11-22–1999-11-23	0.050 ± 0.0	9.98 ± 0.56	245.8	249.4
LS-4	2000-02-26–2000-02-28	0.058 ± 0.0	11.06 ± 0.43	243.9	248.9
LS-5	2000-03-03–2000-03-05	0.058 ± 0.0	11.65 ± 0.13	237.7	241.2
LS-6	2000-03-08–2000-03-09	0.059 ± 0.0	9.73 ± 1.20	240.0	251.8

Acronyms

AMSR-E	Advanced Microwave Scanning Radiometer onboard EOS
AMSR2	Advanced Microwave Scanning Radiometer 2
AO	Arctic Oscillation
ASPeCt	Antarctic Sea Ice Processes & Climate
DMSP	Defense Meteorological Satellite Program
GCOM	Global Change Observation Mission
ECMWF	European Center for Medium-Range Weather Forecast
EUMETSAT	European Organisation for the Exploitation of Meteorological Satellites
ESA	European Space Agency
GHz	Gigahertz
H	Horizontal Polarization
IFOV	Instantaneous Field-of-view
MODIS	Moderate Resolution Imaging Spectroradiometer
MEMLSI	Microwave Emission Modeling of Layered Snowpacks on Sea Ice
MIZ	Marginal Ice Zone
NASA	National Aeronautics and Space Administration
NCAR	National Center for Atmospheric Research
NCEP	National Centers for Environmental Prediction
NOAA	National Oceanic and Atmospheric Administration
NH	Northern Hemisphere

NPC	North Polar Cap
NSIDC	National Snow and Ice Data Center
OSISAF	Ocean and Sea Ice Satellite Application Facility
PM	Passive microwave
SH	Southern Hemisphere
SIC	Sea Ice Concentration
SST	Sea surface temperature
SSM/I	Special Sensor Microwave/Imager
SSMIS	Special Sensor Microwave Imager/Sounder
TB	Brightness Temperature
V	Vertical Polarization

List of Figures

List of Tables

References

Andersen, S., R. Tonboe, L. Kaleschke, G. Heygster, and L. T. Pedersen, 2007: Intercomparison of passive microwave sea ice concentration retrievals over the high-concentration arctic sea ice. *Journal of Geophysical Research-Oceans*, **112 (C8)**, C08 004, doi:10.1029/2006JC003543.

Andersen, S., R. Tonboe, S. Kern, and H. Schyberg, 2006: Improved retrieval of sea ice total concentration from spaceborne passive microwave observations using numerical weather prediction model fields: An intercomparison of nine algorithms. *Remote Sensing of Environment*, **104 (4)**, 374–392, URL `http://www.sciencedirect.com/science/article/pii/S0034425706002033`.

Barber, D., A. Fung, T. Grenfell, S. Nghiem, R. Onstott, V. Lytle, D. Perovich, and A. Gow, 1998: The role of snow on microwave emission and scattering over first-year sea ice. *IEEE Transactions on Geoscience and Remote Sensing*, **36 (5)**, 1750–1763.

Beitsch, A., S. Kern, and L. Kaleschke, 2014: Comparison of SSM/I and AMSR-E Sea Ice Concentrations with ASPeCt Ship Observations around Antarctica. *Submitted to IEEE Transactions On Geoscience And Remote Sensing*.

Cavalieri, D., T. Markus, D. Hall, A. Gasiewski, M. Klein, and A. Ivanoff, 2006a: Assessment of EOS Aqua AMSR-E Arctic Sea Ice Concentrations Using Landsat-7 and Airborne Microwave Imagery. *IEEE Transactions on Geoscience and Remote Sensing*, **44 (11)**, 3057–3069.

Cavalieri, D., T. Markus, J. Maslanik, M. Sturm, and E. Lobl, 2006b: March 2003 EOS Aqua AMSR-E Arctic Sea Ice Field Campaign. *IEEE Transactions on Geoscience and Remote Sensing*, **44 (11)**, 3003–3008.

Cavalieri, D. J., 1994: A microwave technique for mapping thin sea-ice. *Journal of Geophysical Research-Oceans*, **99 (C6)**, 12 561–12 572, doi:10.1029/94JC00707.

Cavalieri, D. J., P. Gloersen, and W. J. Campbell, 1984: Determination of Sea Ice Parameters With the Nimbus-7 SMMR. *Journal of Geophysical Research-Atmospheres*, **89 (ND4)**, 5355–5369, doi:10.1029/JD089iD04p05355.

Cavalieri, D. J., T. Markus, and J. Comiso, 2003: AMSRE/Aqua Daily L3 12.5 km Brightness Temperature, Sea Ice Concentration, & Snow Depth Polar Grids Ver. 2. Boulder, Colorado USA, Digital media.

Cavalieri, D. J. and C. L. Parkinson, 2012: Arctic sea ice variability and trends, 1979–2010. *The Cryosphere*, **6 (4)**, 881–889, URL http://www.the-cryosphere.net/6/881/2012/.

Cavalieri, D. J., K. M. St. Germain, and C. T. Swift, 1995: Reduction of weather effects In the calculation of sea-ice concentration with the DMSP SSM/I. *Journal of Glaciology*, **41 (139)**, 455–464.

Cavalieri, D. J., and C. Parkinson, and P. Gloersen, and H. J. Zwally, 1996: Sea Ice Concentrations from Nimbus-7 SMMR and DMSP SSM/I-SSMIS Passive Microwave Data. Boulder, Colorado USA.

Comiso, J., 2004: Sea ice algorithm for amsr-e. *Rivista Italiana di Telerilevamento*, **30 (31)**, 119–130.

Comiso, J. C., 1986: Characteristics of Arctic Winter Sea Ice From Satellite Multispectral Microwave Observations. *Journal of Geophysical Research-Oceans*, **91 (C1)**, 975–994, doi: 10.1029/JC091iC01p00975.

Comiso, J. C., 1995: SSM/I Sea Ice Concentrations Using the Bootstrap Algorithm. NASA Reference Publiacation 1380, Goddard Space Flight Center.

Comiso, J. C., 1999: Bootstrap Sea Ice Concentrations from Nimbus-7 SMMR and DMSP SSM/I-SSMI/S. Boulder, Colorado USA, Digital media.

Comiso, J. C., D. J. Cavalieri, and T. Markus, 2003: Sea ice concentration, ice temperature, and snow depth using AMSR-E data. *IEEE Transactions On Geoscience and Remote Sensing*, **41 (2)**, 243–252, doi:10.1109/TGRS.2002.808317.

Comiso, J. C., D. J. Cavalieri, C. L. Parkinson, and P. Gloersen, 1997: Passive microwave algorithms for sea ice concentration: A comparison of two techniques. *Remote Sensing of Environment*, **60 (3)**, 357–384, URL http://www.sciencedirect.com/science/article/pii/S0034425796002209.

Comiso, J. C. and K. Cho, 2013: *Descriptions of GCOM-W1 AMSR2 Level 1R and Level 2 Algorithms*, chap. Description of GCOM-W1 AMSR2 Sea Ice Concentration Algorithm, 6–1–6–28. Japan Aerospace Exploration Agency Earth Observation Research Center.

Comiso, J. C. and F. Nishio, 2008: Trends in the sea ice cover using enhanced and compatible AMSR-E, SSM/I, and SMMR data. *Journal of Geophysical Research-Oceans*, **113 (C2)**, C02S07, doi:10.1029/2007JC004257.

Curry, J. A., J. L. Schramm, and E. E. Ebert, 1995: Sea ice-albedo climate feedback mechanism. *J. Climate*, **8 (2)**, 240–247, URL http://dx.doi.org/10.1175/1520-0442(1995)008<0240:SIACFM>2.0.CO;2.

Donlon, C. J., M. Martin, J. Stark, J. Roberts-Jones, E. Fiedler, and W. Wimmer, 2012: The operational sea surface temperature and sea ice analysis (ostia) system. *Remote Sensing of Environment*, **116 (0)**, 140–158, URL http://www.sciencedirect.com/science/article/pii/S0034425711002197.

Eastwood, S., K. R. Larsen, T. Lavergne, E. Nielsen, and R. Tonboe, 2011: Global Sea Ice Concentration Reprocessing -– Product User Manual, Product OSI-409. Tech. Rep. Ver. 1.3, SAF/OSI/CDOP/met.no/TEC/MA/138, available from `http://www.osi-saf.org`.

Eppler, D. T., et al., 1992: Passive microwave signatures of sea ice. *Microwave Remote Sensing of Sea Ice*, American Geophysical Union, 47–71, URL `http://dx.doi.org/10.1029/GM068p0047`.

EUMETSAT, 2011: Global sea ice concentration reprocessing dataset 1978-2009 (v2, 2011). EUMETSAT Ocean and Sea Ice Satellite Application Facility, URL `osisaf.met.no.`, Online.

Fuhrhop, R., T. C. Grenfell, G. Heygster, K. P. Johnsen, P. Schlussel, M. Schrader, and C. Simmer, 1998: A combined radiative transfer model for sea ice, open ocean, and atmosphere. *Radio Science*, **33 (2)**, 303–316, doi:10.1029/97RS03020.

Gloersen, P. and D. J. Cavalieri, 1986: Reduction of Weather Effects In the Calculation of Sea Ice Concentration From Microwave Radiances. *Journal of Geophysical Research-Oceans*, **91 (C3)**, 3913–3919, doi:10.1029/JC091iC03p03913.

Grenfell, T. C., et al., 1998: Evolution of electromagnetic signatures of sea ice from initial formation to the establishment of thick first-year ice. *IEEE Transactions On Geoscience and Remote Sensing*, **36 (5)**, 1642–1654, doi:10.1109/36.718636.

Grumman, N., 2002: Algorithm and data user manual (adum) for the special sensor microwave imager/sounder (ssmis). Technical report, Northrop Grumman Corporation Space Systems Division, 1100 West Hollyvale Street P.O. Box 296 Azusa, California 91702-0296. Contract No: F04710-00-C-0001.

Haas, C., A. Friedrich, Z. Li, M. Nicolaus, A. Pfaffling, and T. Toyota, 2009: Regional variability of sea ice properties and thickness in the northwestern Weddell Sea obtained by in-situ and satellite measurements. *The expedition ANTARCTIC XXIII/7 of the Research Vessel Polarstern in 2006*, P. Lemke, Ed., Alfred Wegener Institute for Polar and Marine Research, Bremerhaven, No. 586 in Reports on Polar and Marine Research.

Hall, D. K., V. V. Salomonson, and G. A. Riggs, 2006: Modis/aqua sea ice extent and ist daily l3 global 4km ease-grid day. version 5. [feb 25-27 2013]. URL `http://nsidc.org/data/docs/daac/modis_v5/myd29e1d_modis_aqua_seaice_extent_ist_daily_global_4km_ease_grid_day.gd.html`.

Hallikainen, M. and D. P. Winebrenner, 1992: The physical basis for sea ice remote sensing. *Microwave Remote Sensing of Sea Ice*, American Geophysical Union, 29–46, URL `http://dx.doi.org/10.1029/GM068p0029`.

Heygster, G., L. Pedersen, J. Turner, C. Thomas, T. Hunewinkel, H. Schottmueller, and T. Viehoff, 1996: Pelicon: Project for estimation of long-term variability of ice concentration. *EC Contract Rep. EV5VCT93*, **268**.

Hollinger, J., R. Lo, G. Poe, R. Savage, and J. Peirce, 1987: Ssm/i user's guide. *Nav. Res. Lab., Washington, DC*.

Hollinger, J., J. Peirce, and G. Poe, 1990: SSM/I instrument evaluation. *IEEE Transactions on Geoscience and Remote Sensing*, **28 (5)**, 781–790.

Hunewinkel, T., T. Markus, and G. C. Heygster, 1998: Improved determination of the sea ice edge with ssm/i data for small-scale analyses. *IEEE Transactions On Geoscience and Remote Sensing*, **36 (5)**, 1795–1808, doi:10.1109/36.718647.

Hwang, B. J., J. K. Ehn, D. G. Barber, R. Galley, and T. C. Grenfell, 2007: Investigations of newly formed sea ice in the cape bathurst polynya: 2. microwave emission. *J. Geophys. Res.*, **112 (C5)**, C05 003–, URL `http://dx.doi.org/10.1029/2006JC003703`.

Integrated Climate Data Center (ICDC), 2012: ASI Algorithm SSM/I-SSMI/S sea ice concentration were obtained for all dates in years 1992-2009. Hamburg, Germany, URL `http://icdc.zmaw,de/`.

Ivanova, N., O. Johannessen, L. Pedersen, and R. Tonboe, 2014: Retrieval of arctic sea ice parameters by satellite passive microwave sensors: A comparison of eleven sea ice concentration algorithms. *IEEE Transactions on Geoscience and Remote Sensing*, **PP (99)**, 1–14.

Japan Aerospace Exploration Agency, 2013: Gcom-w1 "shizuku" data users handbook. Data Users Handbook SGC-120011, GCOM-W1 Data Providing Service's Help Desk, Tsukuba Space Center, Japan Aerospace Exploration Agency.

Kaleschke, L., C. Lupkes, T. Vihma, J. Haarpaintner, A. Bochert, J. Hartmann, and G. Heygster, 2001: Ssm/i sea ice remote sensing for mesoscale ocean-atmosphere interaction analysis. *Canadian Journal of Remote Sensing*, **27 (5)**, 526–537.

Kattsov, V. M., V. E. Ryabinin, J. E. Overland, M. C. Serreze, M. Visbeck, J. E. Walsh, W. Meier, and X. Zhang, 2010: Arctic sea-ice change: a grand challenge of climate science. *Journal of Glaciology*, **56 (200)**, 1115–1121, URL `http://dx.doi.org/10.3189/002214311796406176`.

Kawanishi, T., et al., 2003: The advanced microwave scanning radiometer for the earth observing system (amsr-e), nasda's contribution to the eos for global energy and water cycle studies. *IEEE Transactions on Geoscience and Remote Sensing*, **41 (2)**, 184–194.

Kern, S., 2001: *A New Algorithm to Retrieve the Sea Ice Concentration Using Weather Corrected 85 GHz SSM/I Measurements*. Logos-Verlag.

Kern, S., 2004: A new method for medium-resolution sea ice analysis using weather-influence corrected special sensor microwave/imager 85 ghz data. *International Journal of Remote Sensing*, **25 (21)**, 4555–4582.

Kern, S. and G. Heygster, 2001: Sea-ice concentration retrieval in the antarctic based on the ssm/i 85.5 ghz polarization. *Annals of Glaciology*, **33 (1)**, 109–114.

Knuth, M. A. and S. F. Ackley, 2006: Summer and early-fall sea-ice concentration in the Ross Sea: comparison of in situ ASPeCt observations and satellite passive microwave estimates. *Annals of Glaciology*, **44 (1)**, 303–309, URL http://dx.doi.org/10.3189/172756406781811466.

L'Ecuyer, T. S., 2011: Touring the atmosphere aboard the a-train (vol 63, pg 36, 2010). *Physics Today*, **64 (8)**, 10–10.

Lomax, A. S., D. Lubin, and R. H. Whritner, 1995: The Potential For Interpreting Total and Multiyear Ice Concentrations In Ssm/i 85.5 GHz Imagery. *Remote Sensing of Environment*, **54 (1)**, 13–26, doi:10.1016/0034-4257(95)00082-C.

Lubin, D., C. Garrity, R. Ramseier, and R. H. Whritner, 1997: Total sea ice concentration retrieval from the ssm/i 85.5 ghz channels during the arctic summer. *Remote Sensing of Environment*, **62 (1)**, 63–76, URL http://www.sciencedirect.com/science/article/pii/S0034425797000813.

Lüpkes, C., T. Vihma, G. Birnbaum, and U. Wacker, 2008: Influence of leads in sea ice on the temperature of the atmospheric boundary layer during polar night. *Geophys. Res. Lett.*, **35 (3)**, L03 805–, URL http://dx.doi.org/10.1029/2007GL032461.

Maeda, T. and Y. Taniguchi, 2013: *Descriptions of GCOM-W1 AMSR2 Level 1R and Level 2 Algorithms*, chap. Description of GCOM-W1 AMSR2 Level 1R product, 1–1–1–6. Japan Aerospace Exploration Agency Earth Observation Research Center.

Marcq, S. and J. Weiss, 2012: Influence of sea ice lead-width distribution on turbulent heat transfer between the ocean and the atmosphere. *The Cryosphere*, **6 (1)**, 143–156, URL http://www.the-cryosphere.net/6/143/2012/.

Markus, T. and D. J. Cavalieri, 2000: An enhancement of the nasa team sea ice algorithm. *IEEE Transactions on Geoscience and Remote Sensing*, **38 (3)**, 1387–1398.

Marshall, J. and F. Schott, 1999: Open-ocean convection: Observations, theory, and models. *Rev. Geophys.*, **37 (1)**, 1–64, URL http://dx.doi.org/10.1029/98RG02739.

Massom, R. A., et al., 2001: Snow on antarctic sea ice. *Rev. Geophys.*, **39 (3)**, 413–445, URL http://dx.doi.org/10.1029/2000RG000085.

Mätzler, C., R. Ramseier, and E. Svendsen, 1984: Polarization effects in seaice signatures. *Oceanic Engineering, IEEE Journal of*, **9 (5)**, 333–338.

Mätzler, C. and A. Wiesmann, 1999: Extension of the Microwave Emission Model of layered Snowpacks to Coarse-Grained Snow. *Remote Sensing of Environment*, **70 (3)**, 317–325, doi:10.1016/S0034-4257(99)00047-4.

Maykut, G. A., 1982: Large-scale heat exchange and ice production in the central arctic. *J. Geophys. Res.*, **87 (C10)**, 7971–7984, URL http://dx.doi.org/10.1029/JC087iC10p07971.

Nghiem, S. V., et al., 2012: Field and satellite observations of the formation and distribution of Arctic atmospheric bromine above a rejuvenated sea ice cover. *Journal of Geophysical Research-atmospheres*, **117**, D00S05, doi:10.1029/2011JD016268.

Nihashi, S., K. I. Ohshima, M. O. Jeffries, and T. Kawamura, 2005: Sea-ice melting processes inferred from ice-upper ocean relationships in the Ross Sea, Antarctica. *J. Geophys. Res.*, **110 (C2)**, C02 002–, URL `http://dx.doi.org/10.1029/2003JC002235`.

NSIDC User Service, 2013: Monthly ocean masks and maximum extent masks. URL `http://nsidc.org/data/smmr_ssmi_ancillary/ocean_masks.html`.

Oelke, C., 1997: Atmospheric signatures in sea-ice concentration estimates from passive microwaves: Modelled and observed. *International Journal of Remote Sensing*, **18 (5)**, 1113–1136, doi:10.1080/014311697218601.

Ozsoy-Cicek, B., S. F. Ackley, A. Worby, H. Xie, and J. Lieser, 2011: Antarctic sea-ice extents and concentrations: comparison of satellite and ship measurements from International Polar Year cruises. *Annals of Glaciology*, **52 (57)**, 318–326, URL `http://dx.doi.org/10.3189/172756411795931877`.

Ozsoy-Cicek, B., H. Xie, S. F. Ackley, and K. Ye, 2009: Antarctic summer sea ice concentration and extent: comparison of ODEN 2006 ship observations, satellite passive microwave and NIC sea ice charts. *The Cryosphere*, **3 (1)**, 1–9, doi:10.5194/tc-3-1-2009, URL `http://www.the-cryosphere.net/3/1/2009/`.

Parkinson, C. L. and D. J. Cavalieri, 2012: Antarctic sea ice variability and trends, 1979–2010. *The Cryosphere*, **6 (4)**, 871–880, URL `http://www.the-cryosphere.net/6/871/2012/`.

Parmentier, F.-J. W., T. R. Christensen, L. L. Sorensen, S. Rysgaard, A. D. McGuire, P. A. Miller, and D. A. Walker, 2013: The impact of lower sea-ice extent on arctic greenhouse-gas exchange. *Nature Clim. Change*, **3 (3)**, 195–202, URL `http://dx.doi.org/10.1038/nclimate1784`.

Pedersen, L. T. and R. Saldo, 2012: Sea Ice Concentration (SIC) Round Robin Data Package, Sea Ice Climate Change Initiative: Phase 1, ESA-SICCI-RRDP-06-12, Version 1.0. URL `http://sicci.seaice.dk/RRDP/`, Online.

Perovich, D. K., et al., 1998: Field observations of the electromagnetic properties of first-year sea ice. *IEEE Transactions On Geoscience and Remote Sensing*, **36 (5)**, 1705–1715, doi:10.1109/36.718639.

Serreze, M. C. and R. G. Barry, 2011: Processes and impacts of arctic amplification: A research synthesis. *Global and Planetary Change*, **77 (1-2)**, 85–96, doi:10.1016/j.gloplacha.2011.03.004.

Serreze, M. C. and J. A. Francis, 2006: The Arctic amplification debate. *Climatic Change*, **76 (3-4)**, 241–264.

Shokr, M. and L. Kaleschke, 2012: Impact of surface conditions on thin sea ice concentration estimate from passive microwave observations. *Remote Sensing of Environment*, **121**, 36–50, doi:10.1016/j.rse.2012.01.005.

Shokr, M. and T. Markus, 2006: Comparison of NASA Team2 and AES-york ice concentration algorithms against operational ice charts from the Canadian ice service. *IEEE Transactions on Geoscience and Remote Sensing*, **44 (8)**, 2164–2175.

Smith, D., 1996: Extraction of winter total sea-ice concentration in the greenland and barents seas from ssm/i data. *Remote Sensing*, **17 (13)**, 2625–2646.

Spreen, G., L. Kaleschke, and G. Heygster, 2008: Sea ice remote sensing using AMSR-E 89-GHz channels. *Journal of Geophysical Research: Oceans*, **113 (C2)**.

Steffen, K., J. Key, D. J. Cavalieri, J. Comiso, P. Gloersen, K. S. Germain, and I. Rubinstein, 1992: The estimation of geophysical parameters using passive microwave algorithms. *Microwave Remote Sensing of Sea Ice*, American Geophysical Union, 201–231, URL `http://dx.doi.org/10.1029/GM068p0201`.

Stogryn, A., 1978: Estimates of brightness temperatures from scanning radiometer data. *Antennas and Propagation, IEEE Transactions on*, **26 (5)**, 720–726.

Stossel, A., 2010: Employing satellite-derived sea ice concentration to constrain upper-ocean temperature in a global ocean gcm (vol 21, pg 4498, 2008). *Journal of Climate*, **23 (9)**, 2450–2451, doi:10.1175/2010JCLI3643.1.

Stroeve, J. C., M. C. Serreze, M. M. Holland, J. E. Kay, J. Malanik, and A. P. Barrett, 2012: The arctic's rapidly shrinking sea ice cover: a research synthesis. **110 (3-4)**, 1005–1027, URL `http://dx.doi.org/10.1007/s10584-011-0101-1`.

Svendsen, E., C. Mätzler, and T. C. Grenfell, 1987: A model for retrieving total sea ice concentration from a spaceborne dual-polarized passive microwave instrument operating near 90 ghz. *International Journal of Remote Sensing*, **8 (10)**, 1479–1487.

Svendsen, E., et al., 1983: Norwegian Remote-sensing Experiment - Evaluation of the Nimbus-7 Scanning Multichannel Microwave Radiometer For Sea Ice Research. *Journal of Geophysical Research-Oceans and Atmospheres*, **88 (NC5)**, 2781–2791.

Tateyama, K. and H. Enomoto, 2001: Observation of sea-ice thickness fluctuation in the seasonal ice-covered area during 1992–99 winters. *Annals of Glaciology*, **33 (1)**, 449–456.

Tekeli, A. E., S. Kern, S. F. Ackley, B. Ozsoy-Cicek, and H. Xie, 2011: Summer antarctic sea ice as seen by asar and amsr-e and observed during two ipy field cruises: a case study. *Annals of Glaciology*, **52 (57)**, 327–336.

Tonboe, R. and E. Nielsen, 2011: Ocean and Sea Ice SAF Global Sea Ice Concentration Reprocessing Validation Product, Product OSI-409. Tech. Rep. Version 1.3, SAF/OSI/CDOP/met.no/TEC/RP/150, available from `http://www.osi-saf.org`.

Tonboe, R. T., 2010: The simulated sea ice thermal microwave emission at window and sounding frequencies. *Tellus A*, **62 (3)**, 333–344, URL http://dx.doi.org/10.1111/j.1600-0870.2010.00434.x.

Tonboe, R. T., G. Dybkjaer, and J. L. Hoyer, 2011: Simulations of the snow covered sea ice surface temperature and microwave effective temperature. *Tellus A*, **63 (5)**, 1028–1037, URL http://dx.doi.org/10.1111/j.1600-0870.2011.00530.x.

Tucker, W. B., D. K. Perovich, A. J. Gow, W. F. Weeks, and M. R. Drinkwater, 1992: Physical properties of sea ice relevant to remote sensing. *Microwave Remote Sensing of Sea Ice*, American Geophysical Union, 9–28, URL http://dx.doi.org/10.1029/GM068p0009.

Turner, J., T. J. Bracegirdle, T. Phillips, G. J. Marshall, and J. S. Hosking, 2013: An Initial Assessment of Antarctic Sea Ice Extent in the CMIP5 Models. *Journal of Climate*, **26 (5)**, 1473–1484, URL http://search.ebscohost.com/login.aspx?direct=true&db=aph&AN=85789932&site=ehost-live&scope=site.

Uotila, P., T. Vihma, A. B. Pezza, I. Simmonds, K. Keay, and A. H. Lynch, 2011: Relationships between antarctic cyclones and surface conditions as derived from high-resolution numerical weather prediction data. *J. Geophys. Res.*, **116 (D7)**, D07 109–, URL http://dx.doi.org/10.1029/2010JD015358.

Walsh, J. E. and W. L. Chapman, 2001: 20th-century sea-ice variations from observational data. *Annals of Glaciology*, **33 (1)**, 444–448, URL http://dx.doi.org/10.3189/172756401781818671.

Warren, S. G., I. G. Rigor, N. Untersteiner, V. F. Radionov, N. N. Bryazgin, Y. I. Aleksandrov, and R. Colony, 1999: Snow depth on arctic sea ice. *Journal of Climate*, **12 (6)**, 1814–, URL http://search.ebscohost.com/login.aspx?direct=true&db=aph&AN=5580235&site=ehost-live&scope=site.

Weissling, B., S. Ackley, P. Wagner, and H. Xie, 2009: EISCAM - Digital image acquisition and processing for sea ice parameters from ships. *Cold Regions Science and Technology*, **57 (1)**, 49–60, doi:10.1016/j.coldregions.2009.01.001.

Wentz, F. and T. Meissner, 2000: Algorithm theoretical basis document (atbd), version 2. RSS Tech. Proposal prepared for: EOS Project, Goddard Space Flight Center, NASA RSS Tech. Proposal 121599A-1, Remote Sensing Systems.

Wiesmann, A., C. Fierz, and C. Matzler, 2000: Simulation of microwave emission from physically modeled snowpacks. *Annals of Glaciology, Vol 31, 2000*, **31**, 397–405, doi:10.3189/172756400781820453.

Wiesmann, A. and C. Mätzler, 1999: Microwave Emission Model of Layered Snowpacks. *Remote Sensing of Environment*, **70 (3)**, 307–316, doi:10.1016/S0034-4257(99)00046-2.

Winebrenner, D. P., et al., 1992: Microwave sea ice signature modeling. *Microwave Remote Sensing of Sea Ice*, American Geophysical Union, 137–175, URL http://dx.doi.org/10.1029/GM068p0137.

Worby, A. and J. Comiso, 2004: Studies of the Antarctic sea ice edge and ice extent from satellite and ship observations. *Remote Sensing of Environment*, **92 (1)**, 98–111, URL `http://www.sciencedirect.com/science/article/pii/S0034425704001415`.

Worby, A. P., I. Allison, V. Dirita, and C. Antarctic, 1999: *A technique for making ship-based observations of Antarctic sea ice thickness and characteristics*. Antarctic CRC.

Worby, A. P., C. A. Geiger, M. J. Paget, M. L. Van Woert, S. F. Ackley, and T. L. DeLiberty, 2008: Thickness distribution of Antarctic sea ice. *Journal of Geophysical Research-Oceans*, **113 (C5)**, C05S92, doi:10.1029/2007JC004254.

Worby, A. P., K. M. Meiners, and S. F. Ackley, 2011: Antarctic sea-ice zone research during the International Polar Year, 2007-2009. *Deep-sea Research Part II—Topical Studies In Oceanography*, **58 (9-10)**, 993–998, doi:10.1016/j.dsr2.2011.01.001.

Yan, B. and F. Weng, 2008: Intercalibration between special sensor microwave imager/sounder and special sensor microwave imager. *IEEE Transactions on Geoscience and Remote Sensing*, **46 (4)**, 984–995.

Danksagung

Ich möchte Lars Kaleschke danken, dass er mir die Möglichkeit angeboten hat, diese Arbeit durchzuführen und mit seiner Betreuung Grundsteine zum Gelingen dieser Arbeit gelegt hat. Er konnte mir jederzeit hilfreiche Anregungen geben.

Mein besonderer Dank gilt Stefan Kern, der sich als weiterer Betreuer meiner Arbeit angeboten hat. Ich hätte mir keine bessere Unterstützung wünschen können. Stefan Kern wusste immer einen Rat und hat großen Anteil daran diese Arbeit zu einem erfolgreichen Abschluss zu führen.

Heinke Schlünzen möchte ich danken, dass sie den Vorsitz meines Doktoranden-Gremiums im Rahmen der SICCS Graduiertenschule übernommen und mir immer eine offenes Ohr geschenkt hat. Zudem danke ich Heinke Schlünzen, Hartmut Graßl und Dirk Notz, dass sie sich bereit erklärt haben in der Prüfungskommision teilzunehmen.

Ohne eine angenehme Arbeitsatmosphäre ist das Verfassen einer Doktorarbeit kaum möglich. Daher möchte ich folgenden Menschen meinen Dank für ihre Unterstützung und Zusammenarbeit aussprechen: Manfred Brath, Steffen Grünler, Anja Roesel, Maciej Miernecki, Valentin Ludwig, Nina Maaß, David Bröhan, Rasmus Tage Tonboe, Leif Toudal Pedersen, Meike Demgen, Xianshang Tian-Kunze, Mark Carson, Laura Niederdrenk, der Kickerrunde, Philipp Griewank und Dirk Notz.

Die größte Dankbarkeit empfinde ich für Doreen, die mich durch alle Höhen und Tiefen der letzten Jahre begleitet hat. Ich wünsche mir, dass das für immer so bleibt!

Erklärung

Hiermit erkläre ich an Eides statt, dass ich die vorliegende Dissertationsschrift selbst verfasst und keine anderen als die angegebenen Quellen und Hilfsmittel benutzt habe.

Hamburg, den 1.07.2014